Summer 2018

DYNAMICS OF A CIRCULAR CYLINDER IN CLOSE PROXIMITY TO A WALL

Yargo Teixeira Gomes de Melo
Bucknell University, ytgm001@bucknell.edu

I, Yargo Teixeira Gomes de Melo, do grant permission for my thesis to be copied.

DYNAMICS OF A CIRCULAR CYLINDER IN CLOSE PROXIMITY TO
A WALL

by

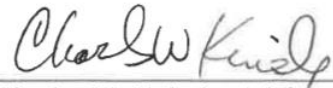Yargo Teixeira Gomes de Melo

(A Thesis)

Presented to the Faculty of
Bucknell University
In Partial Fulfillment of the Requirements for the Degree of
Master of Science in Mechanical Engineering

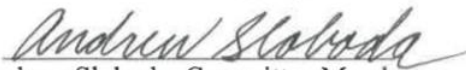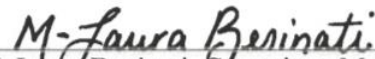Approved:

_____
Charles W. Knisely, Adviser

_____
Constance W. Ziemian, Dept. Chair

_____
Andrew Sloboda, Committee Member

_____
M. Laura Beninati, Committee Member

7/26/2018
_____
Date

ACKNOWLEDGEMENTS

TABLE OF CONTENTS

LIST OF FIGURES

ABSTRACT

The effect of wall proximity on the mechanism of flow-induced vibration of a circular cylinder mounted in a wind tunnel and free to vibrate with two degrees-of-freedom near a rigid plane boundary were examined at a Reynolds number of 1.86×10^5. Hot-wire anemometry and cylinder-mounted accelerometers were used to characterize the flow-induced vibration of the cylinder.

In the near wall region (gap ratios, *G/D*< 0.4) the system was found to exhibit symptoms of movement-induced vibration resulting from the push-and-draw effect of the cylinder pushing into and out of the fluid immediately upstream and downstream of the cylinder. The variation of the width of the separated wake region with the cylinder motion produces a force in phase with the cylinder velocity, resulting in excitation of the cylinder motion.

For *G/D* > 1.0, the alternate shedding of vortices (the Kármán vortex street) produces a fluctuating lift on the body. The lift force also has an associated drag fluctuation at twice the vortex shedding frequency

For 0.4 > *G/D*> 1.0, the excitation appears to be due to the combined effects of the movement-induced vibration found in the near wall region with the vortex shedding from the cylinder found for the free cylinder when it is far from the wall..

The system exhibited mechanical coupling of the two degrees-of-freedom, so additional tests will be needed to conclusively confirm the findings presented in this thesis.

Chapter 1 Introduction

The topic of this thesis, the effect of wall proximity on the flow-induced vibration of a circular cylinder, is a moderately complicated topic. To understand the effect of wall proximity, basic mechanisms of flow-induced vibration will be reviewed. The interaction between fluid flow past a structure and the dynamics of the structure may result in fluid-structure interaction, in which the fluid flow fluctuations induce forces that result in body motion and the body motion reinforces the unsteady flow processes. It is important to distinguish different types of vibration, that is, which mechanism drives the structural vibration, and which parameters affect the natural selection of dominant mechanism of vibration.

A commonly used name for such fluid structure interaction is flow-induced vibration. Flow-induced vibrations (FIV) occur in a wide variety of systems and flow geometries. An extensive, almost overwhelming, catalog of individual occurrences could be compiled; however, a more productive approach is to examine the underlying mechanisms of such flow-induced vibration. Such a systematic approach was formulated in the classification scheme introduced by Naudascher & Rockwell (1994).

In their scheme, Naudascher & Rockwell consider body oscillators, fluid oscillators, and sources of excitation. The body oscillator is an elastic system or component that can undergo linear or rotational displacements. A fluid oscillator is a fluid mass that can undergo oscillations due to effects of compressibility or gravity. Sources of excitation are identified as extraneously-induced excitation (EIE), instability-induced excitation (IIE), and movement-induced excitation (MIE).

Extraneously-induced excitation (EIE) includes effect from ambient noise and vibrations, such as that due to machinery and components, water waves, wind gusts, background turbulence and earthquakes. Instability-induced excitation (IIE) includes those vibrations due to all forms of fluid instability producing inherent flow fluctuations that serve as the source of excitation. Examples include impinging shear layers, vortex shedding, interfacial flows, bi-stable flows, and swirling flows. Movement-induced excitation (MIE), perhaps the largest class of FIV problems, occurs when structural motion produces a flow perturbation that subsequently amplifies the original structural motion. MIE can couple with flow pulsations and may involve structural mode coupling or multiple-body coupling.

The mechanism of vortex-induced vibration (VIV), one example of instability-induced-excitation, results from the agglomeration of oppositely signed vorticity on the two sides of the cylinder which periodically shed from alternate sides of the body. The shed vortices produce a fluctuating transverse force (lift) at the frequency of vortex shedding and a smaller in-line force (drag) at twice the frequency of vortex shedding. These vortices are generated by the action of viscosity as the fluid passes over the body and occur independent of any structural motion. If the structure is elastic or spring-mounted, the shed vortices may induce structural vibration; when the structural frequency is sufficiently close to the vortex shedding frequency, the vibrations enhance the strength of the shed vortices and can shift slightly the vortex shedding frequency in a process called lock-in. The structural frequency is said to "capture" the vortex shedding frequency. Figure 1 shows the frequency and amplitude characteristics associated with
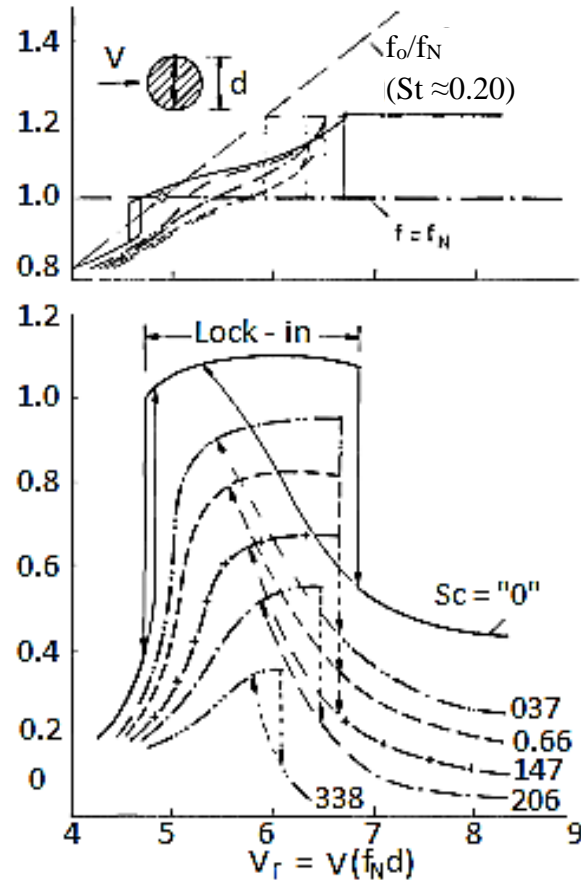
Figure 1 Amplitude and frequency characteristics for the lock-in region for a circular cylinder (from Naudascher & Rockwell, 1994)

the lock-in region. The system damping exerts a strong influence on the extent of the lock-in region.

In addition to flow past a single circular cylinder, many arrangements of flow past multiple cylinders have been studied, for example, flow past multiple smokestacks, flow over closely spaced electrical conductors and pipelines, and flow past heat exchanger tubes.

The geometrical description of adding a second cylinder to the flow is frequently in terms of the angle (α) between the freestream flow and the line connecting the centers

of the cylinders, and the center-to-center spacing ratio (*P/D*). The tandem arrangement occurs when the cylinders are aligned with the flow ($\alpha = 0°$). When $0° < \alpha < 90°$ the cylinders are said to be in a staggered arrangement; and, when $\alpha = 90°$, the cylinders are in a side-by-side arrangement.

When two cylinders are in the tandem configuration, the upstream cylinder shields the downstream cylinder from oncoming flow, resulting in different drag forces acting on the upstream and downstream cylinder. The difference in drag coefficient between the downstream cylinder and the upstream cylinder was designated as the "interference drag coefficient" by Zdravkovich (1977). When the gap ratio between the cylinders is zero, the interference drag is negative; as the gap ratio increases, the interference drag coefficient increases until the drag coefficient on the upstream cylinder reaches its minimum value. This generates what Zdravkovich called a 'kink' in the drag coefficient graph, with the kink being highly dependent on the Reynolds number. Sumner (2010) explained that the fluid behavior is not only a function of the Reynolds number, but also of the gap ratio. At small gap ratios, Kármán shedding is suppressed; at intermediate gap ratios, more complex flow behavior takes place in between the cylinders; at larger gap ratios, the 'kink' appears. In an attempt to physically explain the 'kink,' Alam (2014) considered the aerodynamics of tandem cylinders using surface oil-flow visualization to study the reattachment and boundary layer separation of cylinders in tandem and staggered arrangement in a low speed closed circuit wind tunnel. According to Alam, the 'kink' in the drag coefficient distribution at $3.2 \times 10^4 < Re < 6.5 \times 10^4$ is related to whether the upstream shear layer reattaches to same side surface of the

downstream cylinder as it approaches or reattaches to the front surface of the downstream cylinder and sweeping across to the other side.

Bokaian & Geoola (1984) found that a flexible circular cylinder in close proximity to other bodies behaves differently from an isolated flexible circular cylinder. The mean position of the cylinder, as well as the amplitude and frequency of vibration changes with flow velocity, behaving in a more complex way than is observed for an isolated circular cylinder. When the gap between two cylinders is decreased, the amplitude and frequency tend to increase with increasing flow velocity increases. This phenomenon was called interference galloping and results from movement-induced excitation, in the classification scheme of Naudascher & Rockwell. Interference galloping can be related to the shear layer from the upstream cylinder switching back and forth across the gap, a phenomenon called "jet switching" by Naudascher & Rockwell (1994).

With greater separation between the two cylinders, a different form of galloping, called wake galloping occurs. Zdravkovich (1977) provides an explanation for wake galloping which relies on the velocity gradient in the wake to provide a restoring force if the downstream cylinder is elastically displaced, either inward or outward.

Adding more cylinder to the flow field generates an array of cylinders that might comprise a tube bank. The flow-induced vibration of tube banks is of great concern for the power generation industry due to the reliance on heat exchangers in many power schemes. The fluid-elastic (movement-induced) vibrations of tube banks have been investigated by Weaver (1988), Paidoussis (1999), Blevins (1990) and many others. The displacement of a single tube in a tube bank creates an asymmetric flow producing fluid

loading on the neighboring tubes, which in turn begin to move, resulting in multi-body coupled movement-induced vibration.

Another type of movement-induced vibration occurs when vibration modes couple to produce a self-excited movement-induced vibration. One well-known example is the galloping of the Tacoma Narrows Bridge. Above a critical wind velocity, torsional motion of the bridge deck resulted in negative damping, supplying energy to the structural motion. The resulting instability was called a single-degree of freedom instability by Scanlan & Sabzevari (1967, 1969) and Scanlan & Tomko (1971). More recent and more sophisticated analyses (see Arioli & Gazzola, 2015 and references cited therein) suggest that the Tacoma Narrows failure may have been a movement-induced coupled-mode instability.

Large hydraulic gates have also been shown to have a susceptibility to coupled-mode movement-induced instabilities. Billeter & Staubli (2000) showed that flat-bottomed gates with two degrees-of-freedom are susceptible to multiple instabilities depending upon the reduced velocity and the ratio of the modal frequencies. Ishii et al. (2018) compiled data showing long-span gates with two degrees-of-freedom and inclined upstream weir plates can undergo coupled-mode vibration. Under the "right" conditions the underflow produces a force on the inclined plate, a portion of which produces a vertical gate displacement. The vertical gate displacement produces a discharge fluctuation that produces a streamwise motion. The trajectory of the gate is an elliptical orbit in which the gate moves upstream and upward followed by a downstream and downward motion (Figure 2).
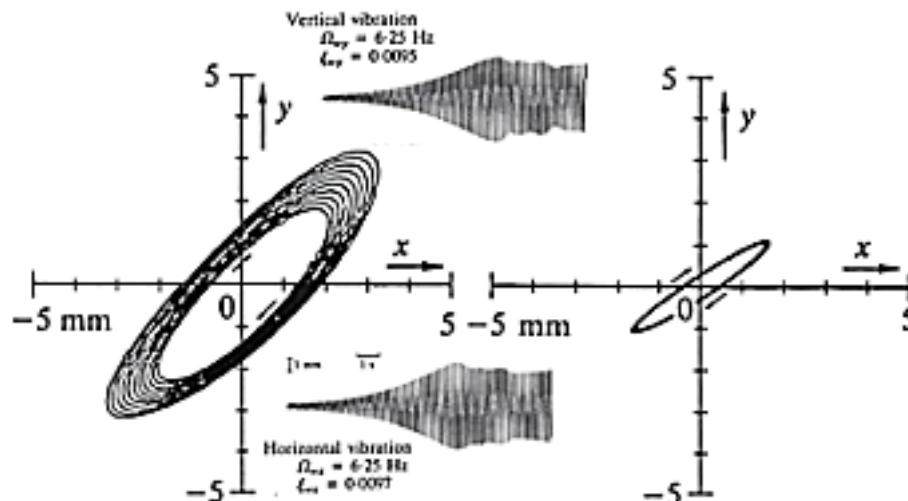
Figure 2 Characteristic elliptical trajectory of long-span gate with inclined upstream weir plate undergoing coupled-mode two degrees-of-freedom vibration, with upstream direction defined as positive (from Ishii et al.,2018)

Similar elliptical trajectories were found for the two degrees-of-freedom vibration of long-span gates with simultaneous over- and underflow. This mechanism is classified as a coupled-mode, movement-induced vibration (Ishii et al., 2018).

With the failure of the massive Folsom Dam Tainter gate in 1995, the analysis of the self-excited coupled-mode vibration for long-span gates was extended to provide a plausible explanation of the Tainter-gate failure (see Anami, et al. 2014, 2015 and Ishii et al.,2018). The application of theoretical analyses to the Folsom Dam gate, under the conditions at the time of failure suggest that the gate also underwent elliptical coupled-mode trajectories in the short time needed for failure. Subsequent measurements on full-scale gates revealed similar characteristic elliptical trajectories.

Flow past a circular cylinder near a plane boundary may behave quite differently from an isolated cylinder. These differences occur due to interactions between the wall

boundary layer and the freestream flow past the cylinder, as well as flow rate fluctuations through the cylinder-wall gap.

A circular cylinder with two degrees-of-freedom in close proximity to a wall exhibits elliptical trajectories, qualitatively similar to those shown for press-shut devices such as flat-bottomed gates with two degrees-of-freedom, long-span two degrees-of-freedom gates with inclined upstream weir plate in underflow, long-span two degrees-of-freedom with simultaneous over- and underflow, and massive Tainter gates undergoing self-excited coupled-mode vibration.

When a bluff body undergoes vibration in the streamwise direction, the wake region between the shear layers separated from this bluff body will alternately expand and contract. Naudascher & Rockwell (1994) denote this phenomenon as wake breathing due to the movement-induced displacements of the separating shear layers that make the near wake appear to "breathe", as depicted in Figure 3.

In this movement-induced excitation, the body motion in the upstream direction reduces the fluid forces, and downstream body motion increases of fluid forces. The streamwise fluid force can become an exciting force via two possible scenarios: a decrease in the drag coefficient with increasing relative velocity and a decrease in drag with decreasing relative velocity; or by means of a movement-induced flow fluctuation, part of which is in phase with the body fluid velocity (Naudascher & Rockwell, 1994).

This first type of wake breathing is associated with negative fluid damping: As the body accelerates downstream, the displaced fluid widens the wake resulting in increased drag with corresponding changes in the instantaneous flow patterns. During the
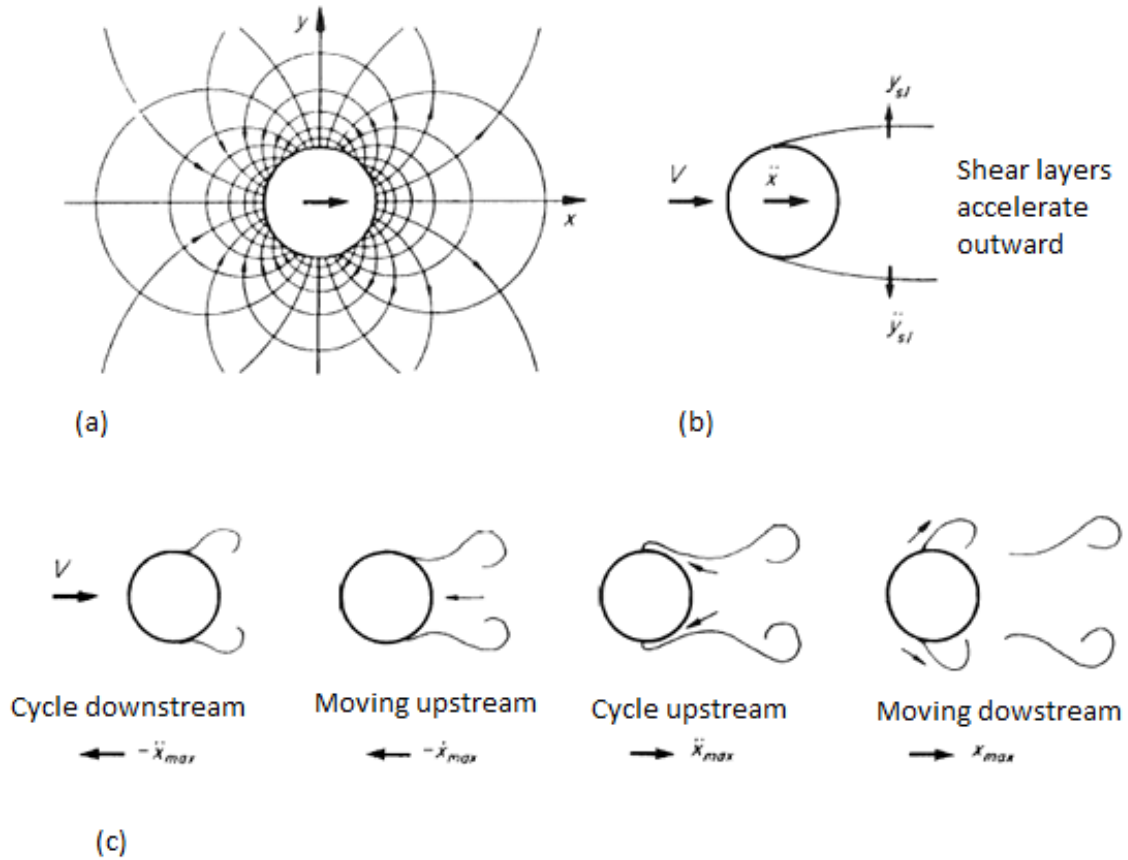
Figure 3 Generation of negative damping due to flow for a circular cylinder vibrating freely in the streamwise direction. (a) Instantaneous streamlines of accelerated cylinder, (b) Accompanying acceleration of free shear layers, (c) Streamlines at different instants during a cycle of cylinder vibration in the range of $1.5 < V/(fD) < 2.0$ (Naudascher & Rockwell, 1994)

upstream portion of vibration, the reverse happens: the wake narrows resulting in a decrease in drag, but again yielding a force fluctuation in phase with the body velocity. The in-phase component can be approximated by a linear relationship between the drag coefficient and the exciting force, but the "breathing-type" excitation is of a more complex nature due to its similarities with instability-induced vortex formation.

In an analysis of movement-induced excitation of a cylinder in proximity to a planar wall, Bokaian (1994) presented a quasi-steady linearized mathematical analysis of the behavior of a circular cylinder near a plane boundary, based on previous studies of multiple cylinders in a staggered arrangement. This theory shows that a galloping instability (resulting from movement-induced excitation) occurs for small gap ratios (G/D) and that the onset velocity for galloping increases with cylinder mass and structural damping.

The study of flow past a cylinder near a plane boundary is of special importance in understanding the mechanism of vibration of ocean pipelines. Such pipelines are often buried, but due to the uneven nature of the seabed and the process of scouring, free spans of pipeline of up to 100 times the diameter of the pipe may be exposed with the gap between the pipeline and the seabed ranging from zero to more than 3 diameters (Sumer et al.,2006.)

Barbosa et al. (2017) classified experiments on the effects of wall proximity in three distinct groups: (1) Experiments using a cylinder in a fixed position with measurements of forces acting on the cylinder; (2) Experiments using forced vibration of the cylinder at specified frequency and amplitude, with measurements of the resulting fluid forces; and, (3) Experiments with free vibration studies, with a cylinder vibrating freely, with measurements of amplitude, frequency and phase characteristics of the motion.

Group (1) Force measurements on stationary cylinder

Bearman & Zdravkovich (1978) were among the first to study this system with a fixed cylinder, considering the flow past it analogous to the flow about two cylinders in tandem arrangement. Their study varied the gap ratio (*G/D*) from zero (cylinder touching the plane boundary) to 3.5. The thickness of the boundary layer at the cylinder position was 0.8 times the diameter, with Re equals to 2.5 x 10^4 and 4.8 x 10^4. The authors confirmed the assumption that for gap ratios of *G/D* < 0.5 the flow past the cylinder is analogous to that one of two cylinders in tandem arrangement.

Later, Zdravkovich (1985) studied the fluid forces related to this arrangement, measuring the lift and drag forces on a fixed circular cylinder with 0 < *G/D* < 2, and $4.8x10^4$ < Re < $3x10^5$. Zdravkovich found that the lift coefficient is governed by *G/D*, while the drag coefficient was governed by the ratio of the gap distance between the cylinder and the wall to boundary layer thickness *G/δ*.

The effects of a wall on oscillatory flow past a fixed circular cylinder (1) was analyzed by Sumer et al. (1990), with 0 < *G/D* < 2, in a work complementary to that of Bearman & Zdravkovich, extending the study from steady flow to oscillatory flow. This study indicated that the vortex flow regimes undergo considerable changes as the gap ratio decreases. The vortex shedding is suppressed for small gap ratios, and the value in which the shed vortices are suppressed increase with the Keulegan-Carpenter number (KC). When the cylinder is placed near the wall, the lift experiences short-duration peaks associated with vortex shedding from the wall side, in the direction opposed to the wall.

Buresti & Lanciotti (1992) investigated the mean and fluctuating forces on a fixed cylinder near a wall, with boundary layer thickness over diameter ratio (δ/D) ranging from 0.1 to 1.1, Reynolds numbers $0.86 \times 10^5 < \text{Re} < 2.77 \times 10^5$, and varying *G/D*. This study showed that the mean forces are significantly affected by the gap ratio, presenting a higher lift and smaller drag ratio as the gap ratio decreased.

Lei et al. (1998) studied the effects of the boundary layer thickness, proximity to the wall, and the velocity gradient on the pressure distribution on a fixed cylinder near a wall. In agreement with previous studies, both lift and drag were found to strongly depend on the gap ratio and the boundary layer thickness. The drag is greater in thinner boundary layers and is almost unaffected when the cylinder is out of the boundary layer. The authors also proposed a method to calculate the point where vortex shedding is suppressed, with good results.

The flow around past a fixed circular cylinder near a plane boundary behaves similar to the flow past cylinders in tandem arrangement, with drag and lift forces being function of gap ratio (*G/D*) and boundary layer thickness.

Rao et al. (2013) generated a CFD analysis of a cylinder translating past a plane boundary, with varying gap ratio, $0.005 < G/D < \infty$, at *Re* = 200. Their model seemed to accurately predict the behavior of the cylinder at all gap ratios, agreeing with current literature. Their analysis presented a figure showing the computed lift coefficient versus the computed drag coefficient. The plots of lift coefficient versus drag coefficient, as shown in Figure 4, yielded figure eight trajectories for the cylinder with large gap ratios, as expected for vortex-induced vibration, and elliptical trajectories for small gap ratios, as
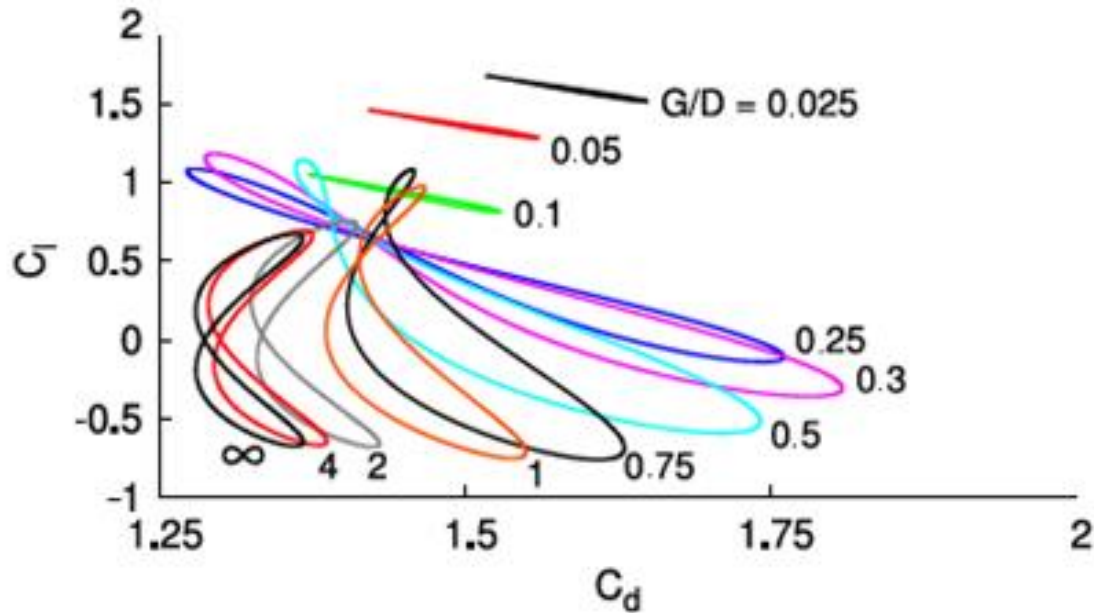
Figure 4 Computed lift coefficient as a function of drag coefficient for a cylinder translating above a fixed surface showing changing force coefficient trajectories with varied gap ratio *G/D* (from Rao et al., 2013)

has been observed in physical experiments. For intermediate gap ratios the force

coefficient exhibited a combination of elliptical and figure eight trajectories.

Group (2) Forced vibrations of cylinders in wall proximity

Few studies have been made on forced vibration of cylinders near a plane

boundary, Hover et al. (1998) studied forced vibration of rigid cylinders compared to free

vibration. The lift and drag coefficients seemed to agree for forced and free vibrations for

uniform and tapered cylinders.

Gopalkrishnan (1993), examined vortex-induced vibration on oscillating bluff

bodies, studying the interaction between circular cylinders and hydrofoils in close

proximity to each other.

Group (3) Measurement of elastic or spring-mounted cylinder in wall proximity

Sumer et al. (1994) studied the flow around a cylinder freely vibrating (2) in the cross-flow direction at close proximity to a plane boundary. The lift and drag forces increased by more than 100% due to vibrations. The effects on the lift were significantly larger when the cylinder was closer to the wall.

Hover et al. (1998) conducted research comparing group (2) and (3), concluding that the lift and drag coefficient agreed for both cases.

Barbosa et al. (2017) conducted research on groups (1) and (3), his studies on free to vibrate cylinders observed that inside the lock-in region, the amplitude of vibration is not affected by the wall, for gap ratios of $G/D > 2$. The amplitude of vibration seemed to remain symmetric, but decreased as the cylinder approached the wall, from $0.75 < G/D < 2$, and for smaller gap ratios, the amplitudes of oscillation were not symmetric any longer.

Effects of the gap ratio and boundary layer

The proximity to a plane boundary affects the flow around the cylinder by shifting the front stagnation point and by varying the base pressure. Alternate vortex shedding weakens with decreasing gap ratios. For gap ratios above 2.0, the effects of the wall are negligible (Lei et al., 1998). Oner et al. (2008) showed that the gap ratio (G/D) is the major parameter affecting the flow structure around a fixed circular cylinder near a plane boundary. According to Oner et al., increasing the gap G/D values greater than 1.0 eliminates any wall effects.

Shed vortices become more irregular as the gap ratio decreases, and the width of lock-in range increases with decreasing gap ratio (Yang et al., 2005). The work of Barbosa et al. (2017) supported the results found by Lei et al. (1998) which showed that for gap ratios above 2.0, the wall boundary layer does not affect the circular cylinder. For $0.75 < G/D < 2.0$, the amplitude of vibration decreases, but the vibration remains symmetric. For gaps below 0.75 diameters, the cylinder can impact the boundary, generating a non-symmetrical movement. This study also agrees with Yang et al. (2005) showing that the lock-in range widens as the gap ratio decreases, increasing the frequency and amplitude of vibration.

For gaps of $G/D < 0.3$ strong regular vortex shedding was suppressed. All the G/D ratios where vortex shedding was suppressed were accompanied by separation bubbles on the plate upstream and downstream of the cylinder. For $G/D = 0$ the bubbles attached to the cylinder. Flow around a cylinder near a wall considered analogous to the side-by-side arrangement of two cylinders, the two geometries exhibit behavior similar at $G/D > 0.5$. The flow about two side-by-side cylinders becomes bi-stable at $G/D < 0.5$ while at that gap ratio, a cylinder near a wall does not show these bi-stable states (Bearman & Zdravkovich, 1978).

Vortex flow regimes identified by Williamson (1985) undergo changes with proximity to a wall when $G/D < O(1)$. Transverse vortex sheet was observed for an isolated cylinder for $0.077 < St < 7$, but it disappears when $G/D < 1.7$. Vortex shedding is suppressed for small G/D, and the G/D below which vortex shedding is suppressed decreases with Strouhal number. For low Strouhal numbers in the range 0.05 to 0.1,

shedding persists for $G/D = 0.1$; vortex shedding frequency is a function of G/D, and it increases when gap ratio increases (Sumer et al., 1990).

Critical gap ratio

As shown in Figure 5, the vortex suppression can be seen in the behavior of the RMS lift coefficient, or the power spectra of the fluctuating lift at gap ratios of about 0.2 or 0.3 (Lei et al., 1998). Bearman & Zdravkovich (1978) observed the suppression of vortices at $G/D = 0.3$ at Re = 4.5 x 10^4; similar results were obtained by Grass et al. (1984).

Strouhal number

Both the gap ratio and velocity gradient influence the Strouhal number (Lei et al.,1998). Sub-critical regimes present Strouhal number of 0.2 for cylinders near a plane boundary (Yang et al., 2009). Regular vortex shedding persists at the same Strouhal number for all gaps down to $G/D = 0.3$ (Bearman & Zdravkovich, 1978).

Grass et al. (1984) observed an increase of Strouhal number due to a combination of proximity to the plane boundary and velocity gradients of a maximum of 25 percent, as shown in Figure 6.

Hydrodynamic forces

There are a number of practical tools to predict hydrodynamic forces acting on bluff bodies, a more current approach for prediction in-line forces induced by waves and currents were proposed by Aristodemo et al. (2011) as an alternative to the more widespread Morrison equation (Morrison et al., 1950) and wake models. Aristodemo et

al. propose a new wake II model as a numerical approach for the evaluation of the

hydrodynamic forces acting on a submerged pipeline.
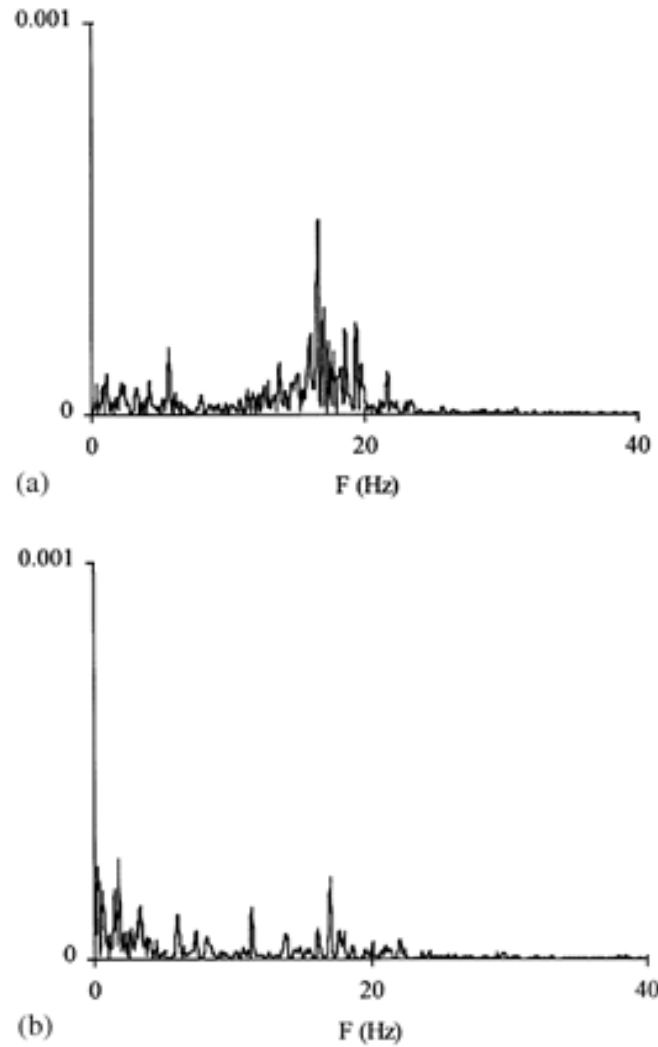
Figure 5 Power spectra of fluctuating lift near the critical gap ratio in a thin boundary layer (a) *G/D*= 0.3, Re = 13900, and (b) *G/D*= 0.2, Re = 13100 (from Lei et al., 1998)
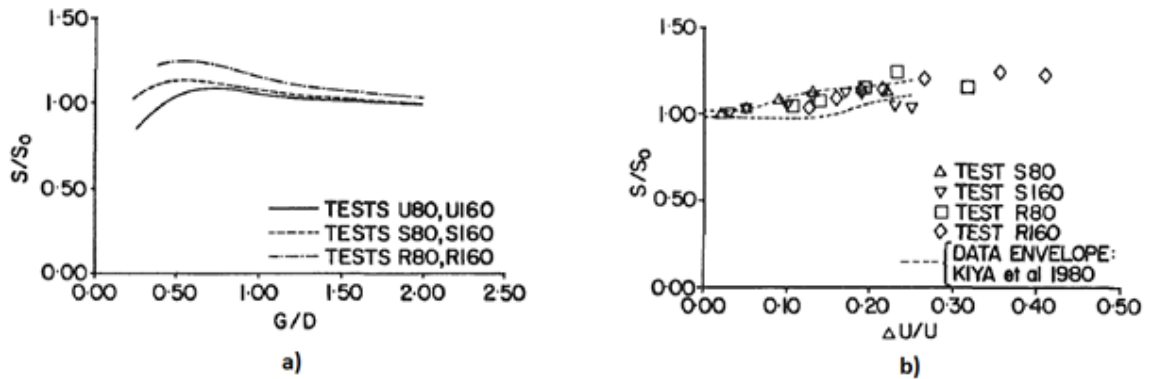
Figure 6 Normalized Strouhal number dependence on (a) gap ratio, and (b) velocity gradient parameter (from Grass et al., 1984)

Lift

For the case of a fixed cylinder (1), the lift coefficient is dominated by the gap ratio (Lei et al.,1998). The lift coefficient depended strongly on *G/D* with complex variation depending on type of boundary layer (Zdravkovich, 1985). Symmetry in both formation and motion of vortices observed for isolated cylinder for Strouhal number > 0.20-0.25 disappears with close proximity to a wall, which creates a periodic lift force on the cylinder. When cylinder is very close to the wall, the lift forces exhibit distinct, short duration peaks, directed away from the wall, and associated with vortex shedding from the wall side of the cylinder (Sumer et al., 1990). Vibrations may increase drag and lift forces up to 100% in pipelines, especially when cylinder is near a wall (Sumer et al., 1994).

Drag

The drag coefficient is dominated by the gap ratio (Lei et al.,1998). The drag coefficient was almost unaffected by *G/D* until the gap value was about the same as the

thickness of the wall boundary layer (Zdravkovich, 1985). The drag coefficient did not show any clear trends as a function of *G/D*, but showed a dependence on the boundary layer thickness that may have been caused by reduced dynamic pressure or increased turbulence intensity (Buresti & Lanciotti, 1992).

Barbosa et al. (2017) observed that the drag forces are amplified in the lock-in region, and the forces can increase up to three times the value for the corresponding stationary force. Barbosa et al. also observed two oscillating components of the drag force, one characterized by the same frequency as the vertical oscillation of the cylinder, and another at twice that frequency.

Effects of a moving wall

In addition to a stationary cylinder, studies were made with a translating wall, a translating cylinder, or a rotating cylinder were examined. Nishino et al. (2007) studied the flow around a fixed cylinder near a moving wall at upper-subcritical Reynolds numbers, with and without end-plates. Rao et al. (2013) examined a translating cylinder near a wall, while Hourigan et al. (2013) considered a translating and rotating cylinder near a wall.

Nishino et al. (2007) studied the effects of a moving wall on a fixed cylinder in its close proximity at upper critical Re. The wall moved at the same velocity as the freestream in order to avoid confusing the effects of the wall boundary layer and the effect of the ground on the cylinder. Nishino et al. observed that at *G/D*< 0.35 the Kármán-type vortices ceased to be generated in the wake of the cylinder, and instead, a dead fluid zone was created, but contrary to what is observed for a fixed wall, the drag

coefficient remained almost constant. A possible explanation of this occurrence according to the authors is that the wall restricts the propagation of disturbances, preventing resonance between the traveling instabilities and the near wake region, similar to what is observed in a cylinder with a backward splitter plate. Bimbato et al. (2011) presented a method to mathematically model the effects of a moving wall on a cylinder.

Scope of thesis

The behavior of the flow around a cylinder near a plane boundary is quite complicated. To unravel some of these intricacies, the work contained in this thesis considered the effects of the most important parameters: the gap ratio, the hydrodynamic accelerations (proportional to the hydrodynamic forces) and the fluctuating velocity.

A distinct change in the cylinder trajectory occurs as the gap between the cylinder and the wall decreases below a certain value. The symmetric vortex shedding becomes increasingly asymmetric, the mean lift can become negative (acting towards the wall), the fluctuating lift increases, the fluctuating drag increases. All these aspects are reflected in elliptic trajectories for the cylinder displacement. Such trajectories are also seen in the movement-induced vibration of closely spaced cylinder arrays. In addition, large hydraulic gates with two degrees-of-freedom also exhibit similar elliptical trajectories, both with underflow and simultaneous over- and underflow. Ishii et al. (2017) develop a theoretical model relying on potential flow analysis with small empirical corrections to predict the vibration of such large gates. One of the driving forces in their model is the pressure loading on the gate due to discharge fluctuation in the underflow. They classify such vibration as movement-induced vibration.

A potential flow study by Valentine & Madhi (2012) provides evidence that a fluctuating singularity in proximity to a cylindrical surface induces a pressure loading on the cylinder. Placing the singularity beneath the cylinder to simulate fluctuating discharge in the gap region reveals a fluctuating lift force resulting from a fluctuating strength source or doublet, or both fluctuating lift and drag for a fluctuating strength point vortex. To determine the loading due to this singularity between the cylinder and the wall will require additional calculations to include an image system symmetrical about the wall upper surface. The study of Valentine & Madhi (2012) provides additional evidence that fluctuating discharge due to a small variation in the gap opening can supply a pressure loading on the cylinder that can potentially excite larger amplitude vibration.

The commonality of elliptical trajectories and fluctuating flow through small gaps near the body surface permits the posing of the question of whether the movement of the cylinder is due to the shed vortices only, or does the movement of the cylinder augment the shedding of vortices in a way that drives the cylinder vibration? In other words, is the mechanism of vibration acting on the cylinder-wall system, vortex-induced as has been observed for isolated cylinders, or is it movement-induced by the cylinder motion in close proximity to the solid boundary, as has been observed for other systems with fluctuating flow through small gaps near the cylinder surface? The hypothesis put forward in this study is that the wall-region vibration results from movement-induced excitation while the isolated cylinder VIV results from instability-induced excitation. The extent of these two regions depend upon the momentum available to drive flow fluctuations in the gap region, requiring consideration of the oncoming boundary layer momentum thickness,

wall roughness, the gap dimension, and the cylinder diameter. From the above cited studies (Bearman & Zdravkovich, 1978; Sumer et al., 1990; Sumer et al., 1994) there is strong evidence that the two excitation mechanisms can be concurrently active in an overlap region, as the strength of the flow rate fluctuation pressure decreases with increased gap ratio.

The intent of this thesis is to delineate the region over which the movement-induced excitation is active from the region over which the instability-induced excitation related to VIV is active. Initially the intent was to test a two degrees-of-freedom spring mounted cylinder at varied G/D ratios in a wind tunnel. Constraints imposed by the wind tunnel geometry resulted in a system that has some coupling between the two degrees -of-freedom, as will be discussed in detail in Chapter 2

Chapter 2 of this thesis presents the apparatus and procedures used in this study, introducing the laboratory facility, as well as the design of the cylinder and wall. Instrumentation and data acquisition are described and a list of tests and procedures undertaken is presented.

Chapter 3 contains important results from the experiments. A more extensive catalog of experimental results is included in Appendix B – Data.

Chapter 4 provides a discussion in which the results from the present study are compared with available literature.

In Chapter 5, the conclusions of this thesis and suggestions for further work are presented.

Appendix A -Wind Tunnel Characteristics presents the method used to calibrate the wind tunnel. In addition, the detailed procedure used to obtain the velocity profile of the wind tunnel is also presented.

The measurement of the added wall boundary layer profile is also contained in this appendix. The measured wall boundary layer profile data are listed in a table.

Appendix B- Data contains a full list of the data for each cylinder-wall location, corresponding spectra.

Appendix C – MATLAB code for data reduction contains a printout of the MATLAB code used to generate time history plots and spectral analysis of the data.

Chapter 2 Apparatus and Procedures

This chapter presents the laboratory facility, the design of the cylinder support, and details of the added wall. Experimental procedures including instrumentation, calibration and data acquisition are also presented.

Wind Tunnel Facility

All experimental work reported in this thesis was carried out in a subsonic, open loop wind tunnel in the Mechanical Engineering Laboratory at Bucknell University.

In Figures 7 and 8 provide a schematic of the wind tunnel and a photograph of wind tunnel, respectively. The cross section of the wind tunnel test section is 17.5 inches wide by 36 inches high with a 9.2:1 contraction ratio nozzle upstream of the test section. The contraction section contains aluminum honey comb with 1/8" cells and five screens at its inlet to provide relatively uniform, low turbulence flow into the test section. The test section is 68.5 inches long, followed by a diffuser and the axial flow fan that draws air through the wind tunnel.
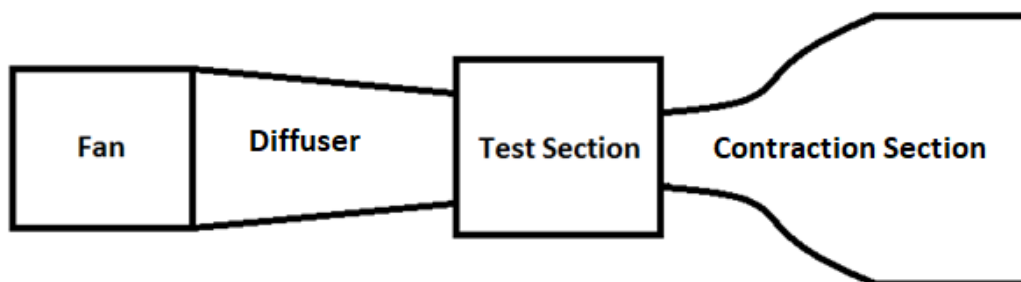
Figure 7 Schematic of the open loop wind tunnel

Figure 8 The subsonic open loop wind tunnel in the Mechanical Engineering Laboratory at Bucknell University

The test section is compliant, allowing a maximum blockage of 33% of the tunnel section. Studies by Ralston (1997), indicate the flow in the test section is uniform to within 1% at the entrance of the test section, and within 2.5% at the axial midpoint of the test section, excluding the boundary layers on the front and back walls of the test section. The wind tunnel has been disassembled and moved twice since Ralston's study. Initial re-measurement of the velocity distributions determined a need for maintenance on the seals between sections of the wind tunnel and then subsequent re-measurement of the velocity distributions in the test section.

A computer controlled traverse system in the test section allows for placement and movement of instruments such as Pitot tubes and constant temperature anemometers. Details regarding the wind tunnel structure and the traverse system are specified in the work of Ralston (1997), the controller of the traverse system was replaced with a Raspberry Pi and a SlushEngine, Model X LT Stepper Motor.

A Pitot tube was used to re-calibrate the wind tunnel after the needed repairs. The Pitot tube was inserted in the geometric center of the test section. The pressure difference across the Pitot tube permitted the calculation of the velocity using Bernoulli's equation $\left(\frac{p}{\rho} + \frac{1}{2}V^2 + gz = \text{constant}\right)$ for isentropic incompressible flow. The stagnation pressure measured using the Pitot tube is the sum of the static pressure and the dynamic pressure, as follows:

$$p_t = p_s + \frac{\rho V^2}{2} \tag{1}$$

where p_t is the stagnation pressure, p_s is the static pressure, ρ is the fluid density, and V is the flow velocity. Solving Equation (2) for the velocity yields:

$$V_{Pitot} = \left(\frac{2(p_t - p_s)}{\rho}\right)^{\frac{1}{2}} = \left(\frac{2\Delta p_{Pitot}}{\rho}\right)^{\frac{1}{2}} \tag{2}$$

where Δp _Pitot_ is the Pitot tube pressure difference, $p_t - p_s$.

The dry air density can be found from the measured atmospheric pressure and the ambient temperature using the following form of the ideal gas law (Equation 3):

$$\rho_{dry} = \left(\frac{P_{atm}}{R_d T}\right) \tag{3}$$

where ρ_{dry} is the density of dry air at the given pressure and temperature, p_{atm} is the measured ambient air pressure, R_d is the gas constant for dry air, and T is the absolute room temperature.

To find the moist air density, the measured relative humidity, η, was used Equation 4:

$$\rho = \frac{\rho_{dry}(1+\eta)}{1+\eta\frac{R_d}{R_{wv}}} \tag{4}$$

where R_{wv} is the ideal gas constant for water vapor.

This process is repeated for several wind tunnel motor speeds, in terms of percentage of full speed. Simultaneously, pressure transducers, mounted in the wall at the entrance and exit of the contraction section, were used to measure the pressure drop across the wind tunnel contraction.

Equation 2 was used to calculate the velocity using the wind tunnel pressure drop measurements, and the result was compared to those from the Pitot tube. Bearing in mind that the values measured by the Pitot tube are the actual velocity of the wind tunnel, and the results obtained by the wind tunnel pressure transducer are proportional to the actual velocity of the flow, a relationship between the velocities measured by the Pitot tube and the wind tunnel pressure transducers can be formulated:

$$C_1 * V_{wt} = V_{actual} = V_{pitot} \tag{5}$$

Plots of the velocities versus the motor speed are given in Figure 9 below:
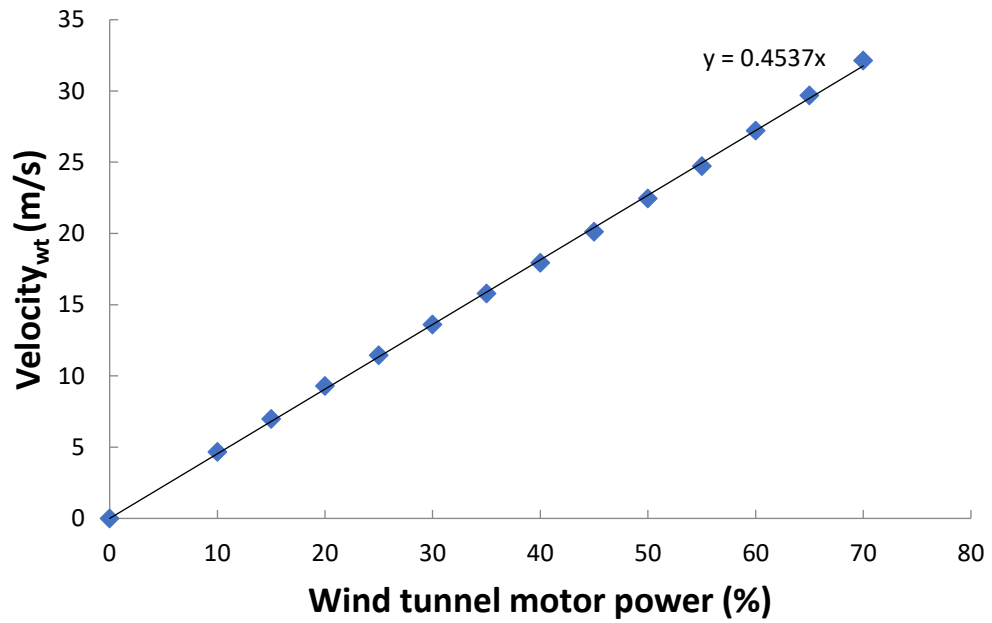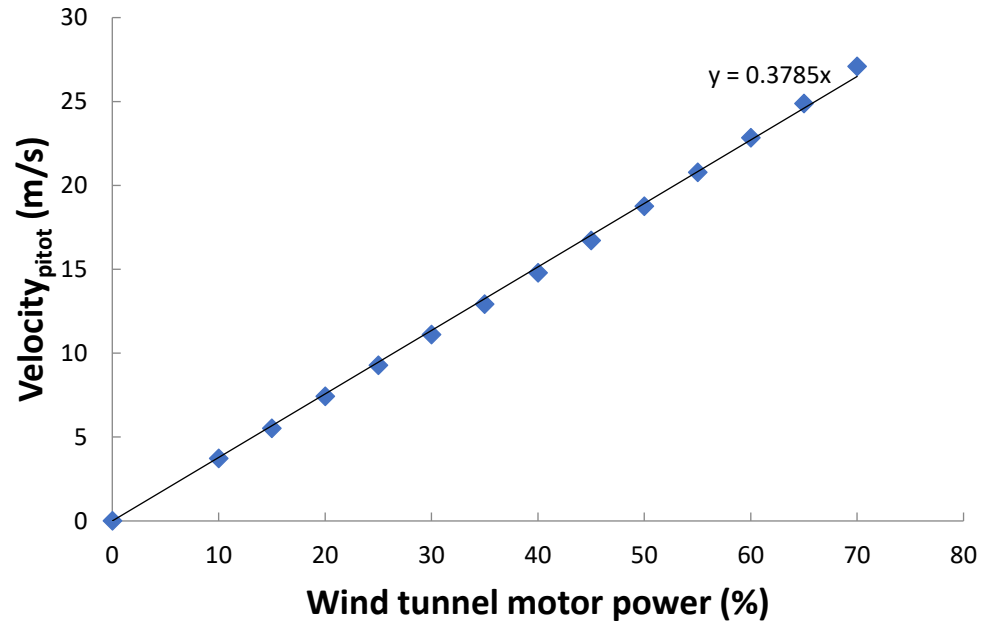
Figure 9 Velocities measured using the (a) Pitot tube, and (b) wind tunnel pressure drop as functions of percentage motor power

As shown in Figure 9, both velocities measured were directly proportional to the wind tunnel speed, but the proportionality constants are still a function of air humidity and pressure. To arrive at a single plot that can be used for any relative humidity and pressure, a standard velocity was arbitrarily selected as

$$V_{STD} = \left(\frac{2\Delta P_p}{\rho_{STD}}\right)^{\frac{1}{2}} \tag{6}$$

where ρ_{STD} is defined as the density of dry air at 1 atmosphere and 293.15 K. The plot of velocity using standard conditions, as shown in Figure 10, is independent of the ambient conditions during data collection.
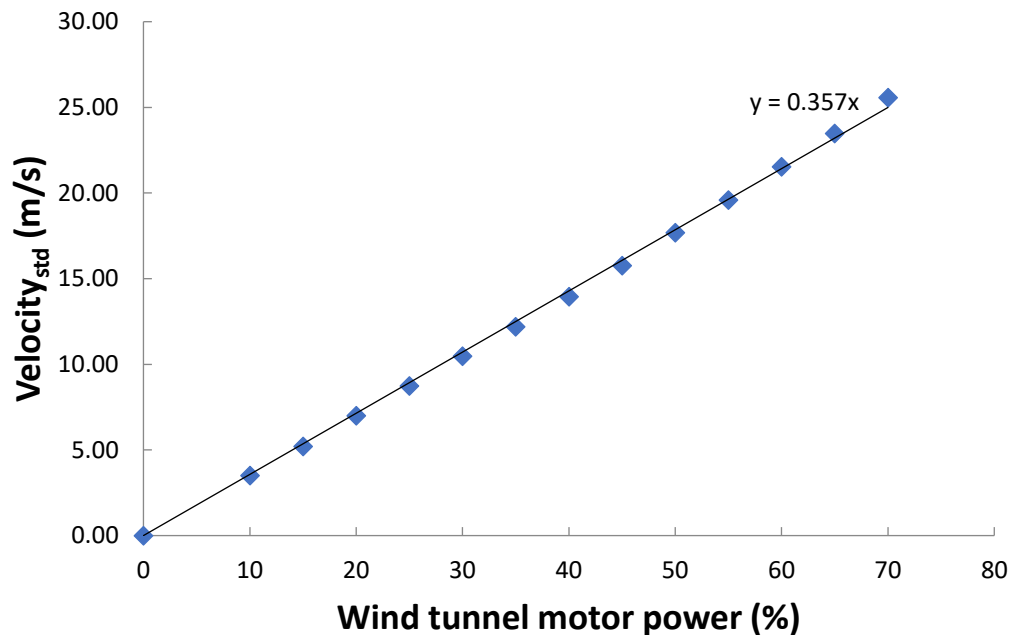
Figure 10 Standard velocity of the wind tunnel as a function of percentage motor power

The relationships between the velocities measured by the Pitot tube and the wind tunnel pressure transducer (Equation 5), can be combined using Equation 6 to determine a relationship between standard and actual velocities, and standard velocity and wind

tunnel pressure difference and moist density. These relationships are shown by Equations 7 and 8 below, respectively:

$$V_{Actual} = V_{STD} \left(\frac{\rho_{STD}}{\rho_m}\right)^{\frac{1}{2}} \tag{7}$$

and

$$\frac{\Delta P_{wt}}{\rho_m} = \frac{1}{2} (V_{STD})^2 \frac{\rho_{STD}}{\rho_m} C_2 \tag{8}$$

where C_2 is a constant calculated via the plots of velocities versus *%N*.

Equations 7 and 8 allow for the actual velocity of the flow to be found with only measurements of relative air humidity and wind tunnel pressure difference, which is summarized by Equation 9:

$$V_{actual} = \left(\frac{2\Delta P_p}{\rho_{STD}}\right)^{\frac{1}{2}} \left(\frac{\rho_{STD}}{\rho_m}\right)^{\frac{1}{2}}, \tag{9}$$

Equation 9 is the calibration equation of the wind tunnel, $\left(\frac{2\Delta P_p}{\rho_{STD}}\right)^{\frac{1}{2}}$ is the standard velocity, drawn from Figure 3, and $\left(\frac{\rho_{STD}}{\rho_m}\right)^{\frac{1}{2}}$, can be found by calculating the moist density with Equation 4 and measuring the pressure difference with the wind tunnel pressure transducer.

Model

To create a test model with two-degrees of freedom, a spring system, intended to allow the cylinder to vibrate freely in the streamwise and cross-stream direction without mechanical coupling, was needed.

A 3.5″ diameter and 36″ length aluminum cylinder was used with a 0.25″ rod

attached by end plates to the centerline of the cylinder. Springs connect the rod to two solid frames, top and bottom, placed in the test section. The mass of the cylinder was 0.48 kg (1.06 lb$_m$), with a mass ratio defined as the mass of the cylinder over the mass of displaced air varying from 44 to 72, depending on the flow density at the time of the experiment.

Springs were dimensioned based on the weight of the cylinder, and the expected frequency of vibration. The expected Strouhal number for a circular cylinder is around *St* = 0.2 for most of the Reynolds number range, as shown in Figure 11.
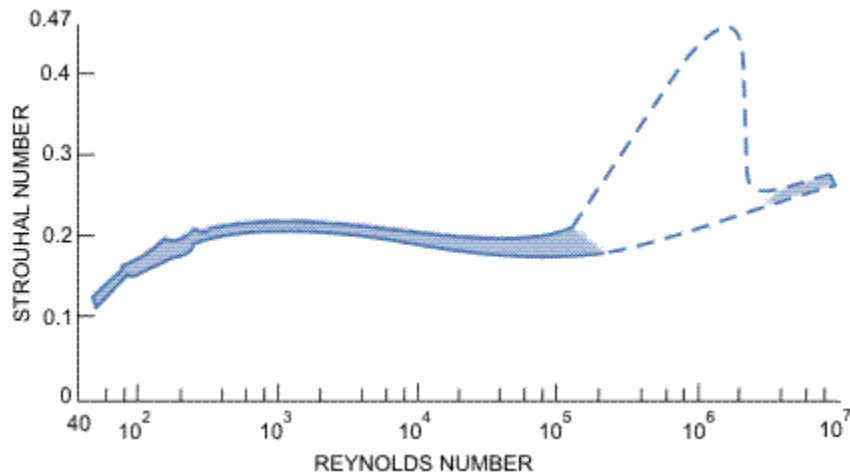
Figure 11 Strouhal number for a stationary circular cylinder as a function of Reynolds number (Blevins, 1990)

Assuming an expected St = 0.2, with a constant diameter for the cylinder, and the measured weight for the system, a frequency and velocity can be selected to determine an appropriate spring constant for the system, using Equations 10 and 11.

$$St = \frac{fL}{U} \qquad (10)$$

and

$$f = \frac{1}{2\pi}\sqrt{\frac{k}{m}} \tag{11}$$

The calculation lead to the use of four precision extension springs with hook ends, with a spring constant of 10.7 lbf/in as shown in Figure 12.
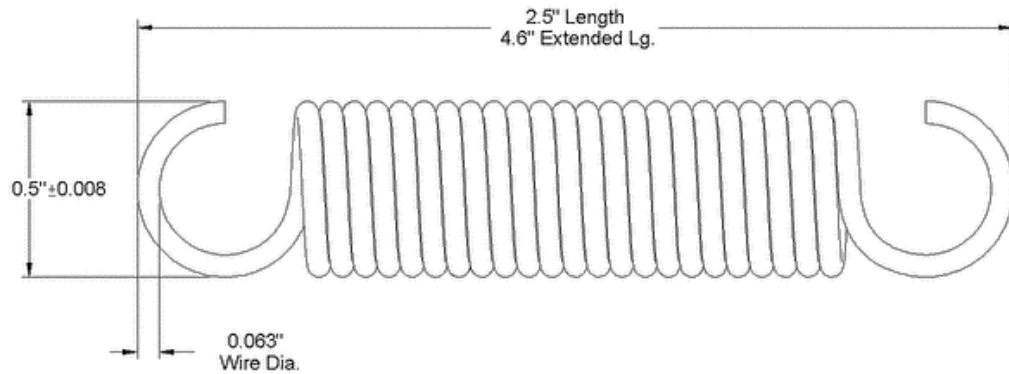
Figure 12 Precision extension spring with a spring constant of k = 10.7 lbf/in

Modified shaft collars, connected with steel guitar strings, were used to connect a 4 ft long 1/4″–20 threaded aluminum rod, shown in Figure 13, to the spring system.
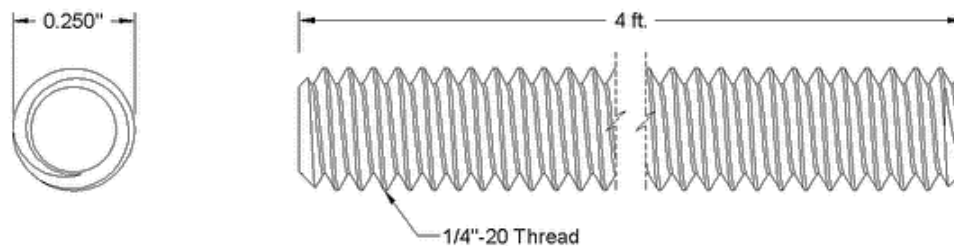
Figure 13 Threaded aluminum rod used to connect the springs to the aluminum cylinder

The threaded aluminum rod was placed inside the 3.5″ diameter cylinder supported on the axis of the cylinder using of four 3D printed inserts that connected the

outside of the threaded rod to the inside of the aluminum cylinder. Subsequently, 3D printed endplates were added on the top and bottom of the cylinder to reduce the end effects.

A false wall was added inside the wind tunnel, reducing the cross-stream cross section from 17.5 to 15 inches. Figure 14 shows the system with the support bars, the springs, the threaded rod, the cylinder and added wall.

Figure 14 Mounted system with base, threaded rod, cylinder and springs

Figure 15 System mounted inside the wind tunnel test section

Two steel support bars were designed, manufactured and mounted to the top and bottom of the wind tunnel, connected to each of these bars a structure composed by T-slotted framing aluminum was mounted. The T-slot frame was chosen as it allowed for easy translation of the cylinder in the lift direction without changing its relative position in the stream wise direction.

Connected to the T-slotted frames were the four springs on the top structure and four springs on the bottom structure, as shown in Figure 16.
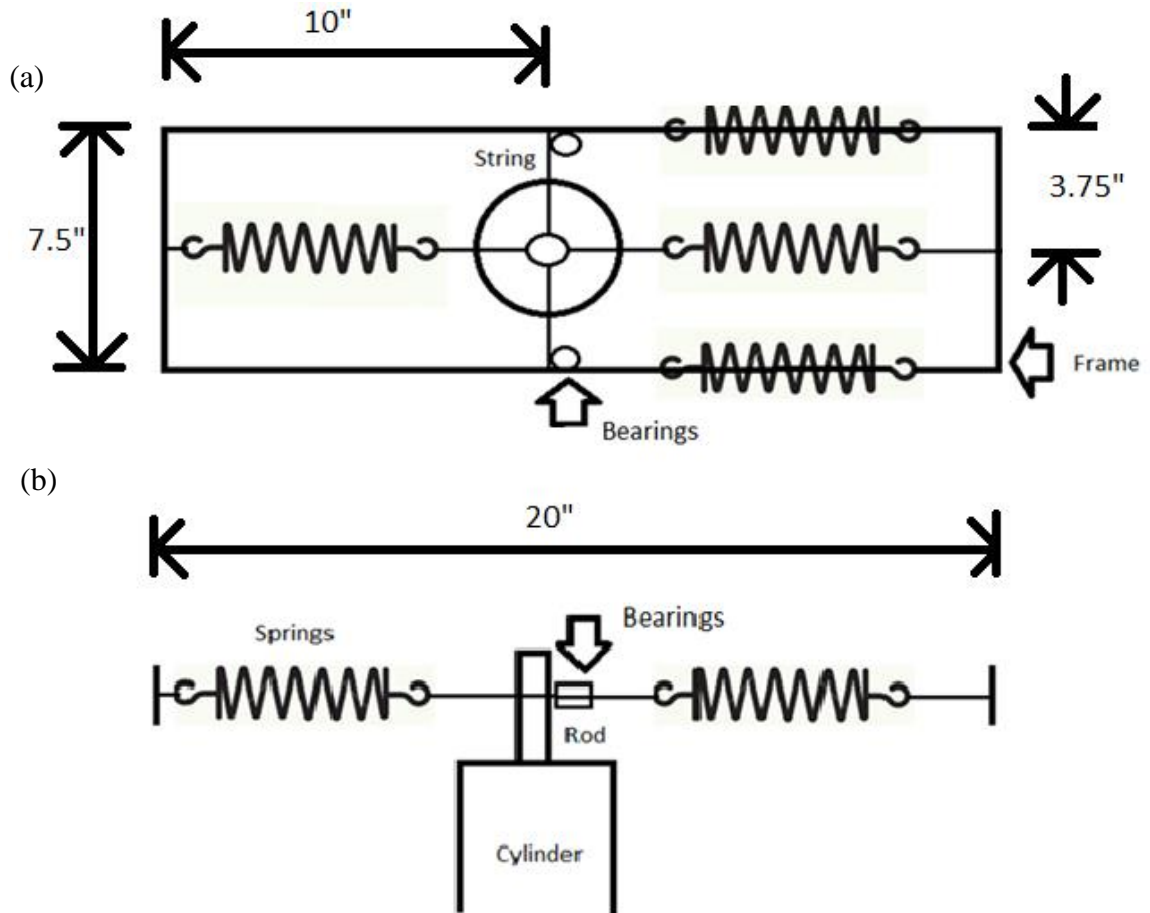
Figure 16 System schematic (a) top view (b) side view

Data Acquisition

To understand better the mechanism of vibration of the cylinder at various gap ratios, an understanding of the relationship between cylinder motion and vortex shedding is required. The vortices are shed into the near wake of the cylinder with a regular frequency; they roll up and move downstream at fixed at certain spatial and temporal intervals for a given gap ratio and Reynolds number. To correlate the vortex shedding with the motion of the cylinder, a hot-wire anemometer was mounted at a fixed position

downstream of the cylinder (2.5 diameters). Beginning inside the shear layer, the hot-wire probe was traversed outward to a point where the velocity fluctuation measured using the hot-wire probe became a relatively clean fluctuating sinusoidal wave. The hot-wire probe was fixed in that cross-stream position (1.0 diameter) on the far side from the added false wall. The position of the probe relative to the cylinder was maintained for all *G/D*.

Tri-axial accelerometers were mounted on the top and bottom of the cylinder end plates to measure the dynamic response of the cylinder in the streamwise and cross-stream directions.

By analyzing the phase angle between the measured velocity fluctuations relative to the fluctuating fluid accelerations, the changing effects of vortex shedding from the outer side of the cylinder can be linked with changes in the lift and drag behavior with *G/D*.

Constant Temperature Anemometer

A DANTEC hot-wire constant temperature anemometer (CTA) was used in order to measure the velocity at which vortices were shed from the cylinder. A CTA is one of two types of thermal anemometer, the other being a constant current anemometer. A thermal anemometer is an instrument that uses an electrically heated sensor to measure fluid velocities by sensing small changes in heat transfer.

A hot-wire of tungsten filament was used to measure the changes in velocity around the cylinder, the tip of the hot-wire was positioned 2 diameters downstream of the

cylinder, and at 0.5 diameters up in the direction of the lift fluctuations, as shown in Figure 17.
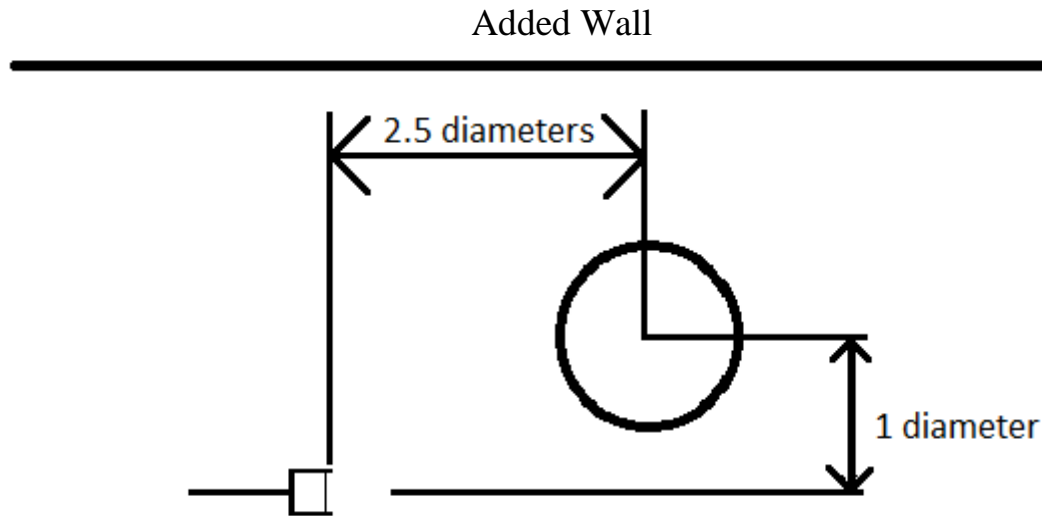
Added Wall

Figure 17 Location of the hot-wire anemometer relative to the cylinder (top view), 2 diameters downstream, and 1.0 diameters in the cross-stream direction

As the cylinder was moved closer to the added wall, the traverse system was moved to maintain that same position relative to the cylinder. The hot-wire output was calibrated using the velocity determined from the correlation between pressure and humidity as a function of the percent power of the wind tunnel motor, as detailed in the wind tunnel facility section of this chapter. The hot-wire was mounted in the free-stream, the velocities were measured and compared to V_{actual}, as calculated using Equation 9. The DANTEC software, STREAMWIRE, presents a calibration table, which after filled with measured values of voltage, and expected values for velocity, generates a calibration curve. The input voltage data measured by the DANTEC STREAMWIRE software was

connected to a NI-DAQ system and read by LabView. The MATLAB code used for the spectral analysis is presented in Appendix C.

Accelerometers

The PCB Piezotronics accelerometers mounted on the end-plates of the cylinder were connected to that same NI-DAQ system, and the voltage output read by the same LabView code. After being recorded, a calibration had to be applied to the acceleration data in all three directions; the calibration was provided by the accelerometer manufacturer and was applied for each data point.

Figure 18 Top accelerometer positioned on the cylinder end plate

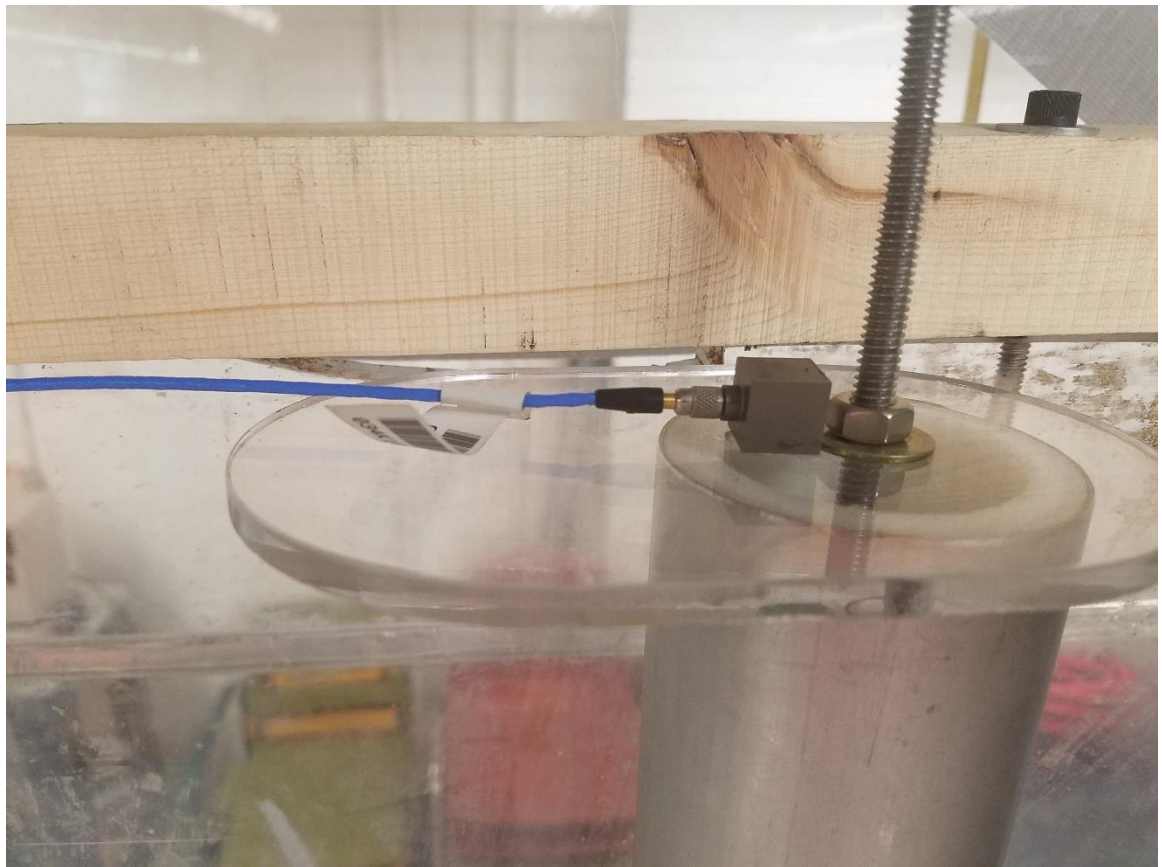The LabView program allowed the simultaneous recording of fluctuating acceleration and velocity fluctuation data at a desired sampling frequency and size.

Signal Processing

Before any data acquisition and signal analysis could be undertaken, a careful study of the data acquisition techniques was made. All the equations for data acquisition were taken from the works of Bendat & Piersol (2011). It was decided that a frequency of resolution of 0.04 Hz would be satisfactory. For a given frequency resolution, the total signal length can be determined using Equation 12:

$$T = {^1}\!/_{\Delta f} \qquad\qquad (12)$$

where T is the sampling time, and Δf is the frequency resolution desired.

From Equation 12 the signal length was determined to be 25 seconds. Analyzing the natural frequency of the model, and considering the literature, it was assumed that all dominant frequencies would be below 100 Hz, a Nyquist cutoff of 100 Hz was used. It is extremely important that there are no dominant fluctuation peaks above the Nyquist cutoff to avoid aliasing. Aliasing is when a frequency exists above the Nyquist cutoff and is reflected as a mirror image frequency peak about the Nyquist cutoff. Therefore, the frequency will be incorrectly recorded.

The sampling frequency must be at least twice the Nyquist Cutoff, in this case 200 Hz.

The data sample must be converted from the time domain to the frequency domain

using a Fourier Transform to examine the spectral densities of the signal as shown by

Equation 13.

$$X(f) = \int_{-\infty}^{\infty} x(t)e^{-j2\pi ftt} \, dt \tag{13}$$

To satisfy Equation 13 for a finite time length, the Fast Fourier Transform (FFT) is

used to estimate the Fourier Transform. The FFT can be calculated by equation 14.

$$X(f,T) = \int_{0}^{T} x(t)e^{-j2\pi ftt} \, dt \tag{14}$$

All data analysis requiring FFT calculations used MATLAB's FFT algorithm.

Once the FFT has been applied to the data, the power spectrum can be calculated by

finding the RMS of the FFT. For better estimation of the spectra, a windowing function is

used to taper the beginning and the end of the time history data. This reduces the leakage

error in the estimation of the Fourier Transform due to the discontinuities at the

beginning and end of the time series. The us this thesis was the Tukey window, also

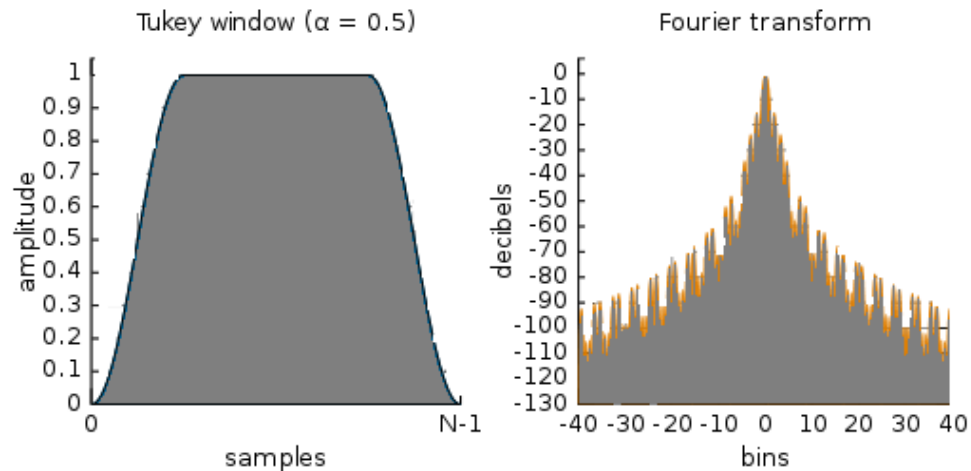known as the tapered cosine window, shown by Figure 19.

Figure 19 Tukey windowing function

Before the measurement of cylinder interaction began, the turbulence intensity of the freestream was estimated. With the calibrated hot-wire probe positioned in the wind tunnel, the mean and root mean square (rms) velocity fluctuations were measured. The turbulence intensity was estimated by dividing the rms velocity by the mean velocity, as indicated in Equation 15.

$$Tu = \frac{V'_{rms}}{\bar{V}} \tag{15}$$

where V'_{rms} is the root mean square of the velocity fluctuations, and $\bar{V}$ is the mean velocity. The average turbulence intensity for the wind tunnel is reported in Appendix A.

Before each test was conducted, the Baratron 10 Torr and 100 Torr pressure transducers were zeroed. The atmospheric pressure, ambient temperature and humidity were measured before and after each experiment, as well as during the time each sample was collected.

Experimental Procedure

For each data sample, 4096 data points were collected at 200 Hz. Thirty data samples were collected at each cylinder location. For each sensor, the data was calibrated, and converted from the time domain to the frequency domain using FFT with the Tukey window function.

The spectra from the 30 data samples at each location were averaged, and three different sets of data for each position were obtained. Eight data records were recorded for each sample: (1) time, (2) streamwise, (3) cross-stream, and (4) transverse accelerations from the accelerometer on the top of the cylinder, (5) streamwise, (6) cross-

stream, and(7) transverse accelerations from the accelerometer on the bottom of the cylinder, and (8) the output from the hot-wire anemometer

Wind Tunnel Velocity Profiles

Wind tunnel velocity characteristics were determined by using the hot-wire anemometer to measure the mean velocity profile along the vertical, horizontal, and axial centerline as a function of percent wind tunnel speed and density including humidity effects. The one-dimensional RMS of the velocity profiles in empty section were also recorded vertically, horizontally and axially along the centerline.

Appendix B contains the detailed study of the wind tunnel velocity profiles, as well as a study of the turbulence intensity in the wind tunnel.

Dynamic Characteristics of the Cylinder

The cross-stream and streamwise natural frequencies of the cylinder were determined by striking the system in the streamwise direction and measuring the acceleration responses in the streamwise and cross-stream direction, and then repeating the experiment striking the system in the cross-stream direction.

Vortex Shedding Characteristics of Cylinder with Flow

The cross-stream and streamwise acceleration peak frequency were measured at different gap ratios. The phase lag between cross-stream and streamwise spectral peaks was recorded from cross-spectral analysis. This procedure was repeated to determine the phase-lag between the cross-stream acceleration and the fluctuating hot-wire data at the fixed relative position in the wake. For small gap ratios the phase-lag between the

streamwise acceleration signal and the fluctuating hot-wire data from the fixed wake

location.

The unsteady characteristics of the cylinder at multiple gap ratios with added false

wall (*G/D*: 1.5, 1, 0.75, 0.5, 0.4, 0.3, 0.2, and 0.1) were calculated and plotted. The same

procedure used for the freestream analysis was repeated at all *G/D*.

Chapter 3 reports on the impact response of the system as well of the dynamic

characteristics of the cylinder.

Chapter 3 Results

In this chapter sample results related to the motion of the cylinder and the vortex shedding are presented. A complete catalogue of results is provided in Appendix B. The results shown in this chapter will be discussed in Chapter 4.

Impact Response Testing

The fluctuating acceleration in the streamwise (drag) and cross-stream (lift) direction responses to a streamwise impact were measured to determine the natural frequencies of the system, as well as to explore whether there was any coupling between the streamwise and cross-stream directions. Subsequently, an analogous measurement was undertaken to measure the fluctuating drag and lift acceleration responses to impact in the lift direction. All results for impact response testing were done using the top accelerometer. All the accelerometer response was converted to m/s^2, and the hot-wire data was reported in terms of voltage.

Figure 20 depicts the streamwise and cross-stream responses in the time domain with impact in the streamwise direction. Figure 21 shows the streamwise and cross-stream responses spectra with impact in the streamwise direction.

Figures 21 (a) and (b) shows a predominant peak at 9.33 *Hz* in the streamwise (drag) direction that is hypothesized to result in a smaller magnitude peak in lift response at that same frequency, as shown in Figures 21 (c) and (d). The second peak (one order of magnitude smaller than the first peak) in the drag direction response at 16.31 Hz in Figures 21 (a) and (b) and present in Figures 21(c) and (d) as well, is conjectured to
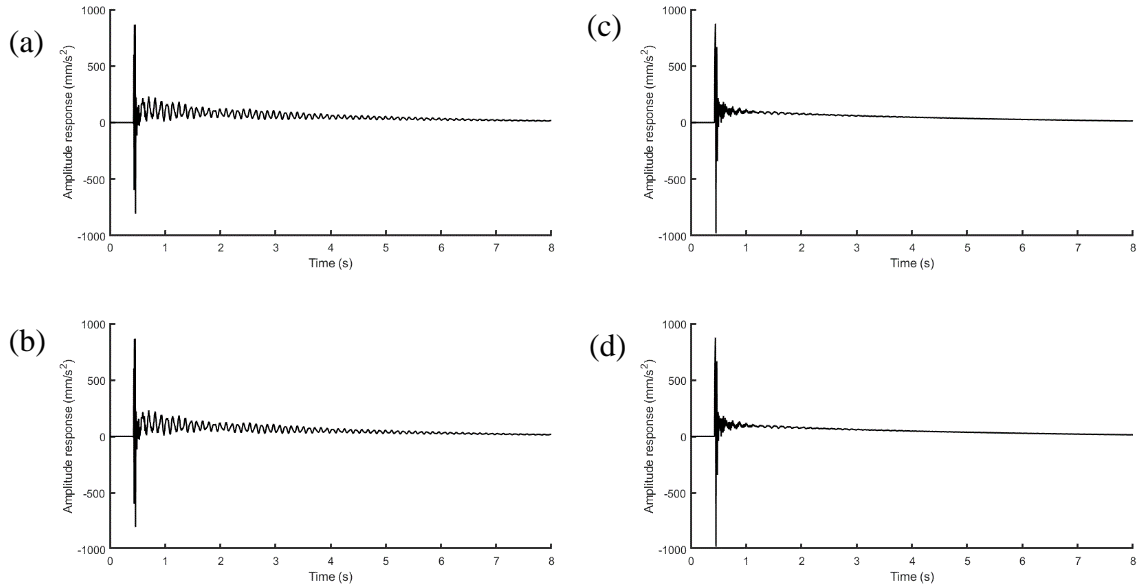
Figure 20 Time response due to streamwise impact as measured by (a) the accelerometer in streamwise direction at the top of the cylinder, (b) the accelerometer in streamwise direction at the bottom of the cylinder, (c) the accelerometer in cross-stream direction at the top of the cylinder, and (d) the accelerometer in cross-stream direction at the bottom of the cylinder

correspond to the natural frequency in the lift direction.

Figure 22 depicts the streamwise and cross-stream responses in the time domain with impact in the cross-stream direction. Figure 23 shows the streamwise and cross-stream responses spectra with impact in the streamwise direction.

Figures 23(a) and (b) exhibit amplitude peaks for the fluctuating streamwise acceleration at 8.79 Hz and 9.38 *Hz*, peaks close to the hypothesized natural frequency of the system in the streamwise direction, and another peak at 16.36 Hz, consistent with the cross-stream natural frequency found in Figures 21 (c) and (d).

The data in Figures 20 through 23 indicate coupling of the fluctuating acceleration responses. When struck in the one direction, the fluctuating acceleration responses are found in the direction of impact as well as in the orthogonal direction. This coupling must
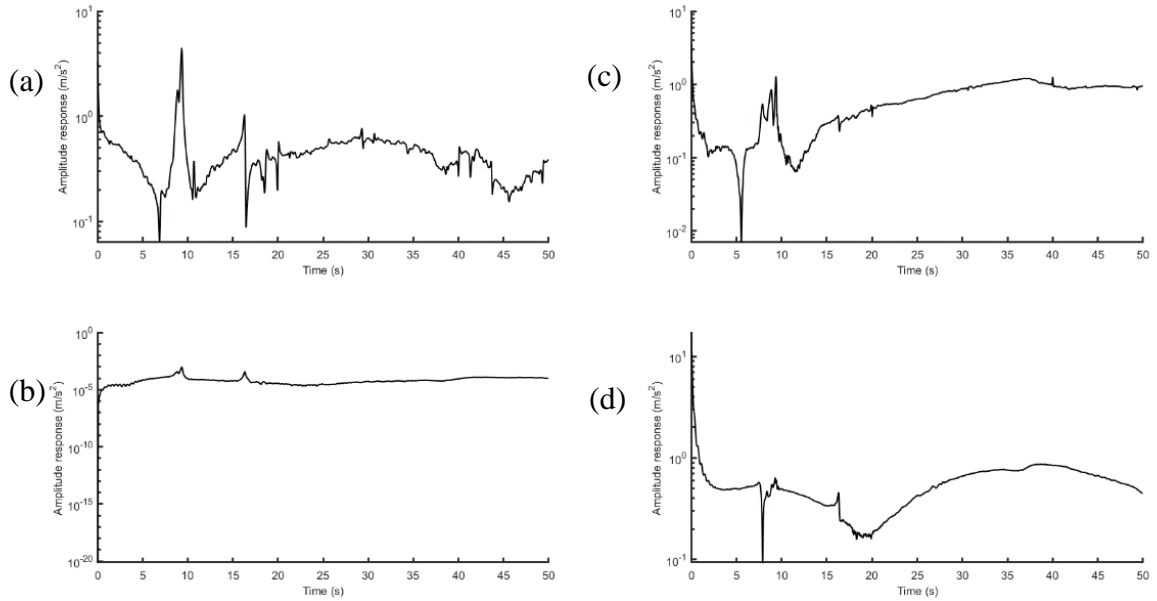
Figure 21 Acceleration logarithmic amplitude spectral response to streamwise impact (a) the accelerometer in streamwise direction at the top of the cylinder, (b) the accelerometer in streamwise direction at the bottom of the cylinder, (c) the accelerometer in cross-stream direction at the top of the cylinder, and (d) the accelerometer in cross-stream direction at the bottom of the cylinder

be considered when looking at the dynamic response of the cylinder when exposed to fluid forces. The time domain responses of the bottom accelerometer showed signs of modulation, likely due to a grounding or mounting problem, that lead to a bigger reliance on the top accelerometer data (Figures 20 and 21). A logarithmic decrement analysis revealed a 3% damping ratio of the system.

Wall Boundary Layer Measurement

With the vertical false wall installed, flow visualization of its leading edge region was undertaken. Flow visualization using oil streaks revealed the presence of a small separation region at the leading edge, approximately 1.0″ in streamwise extent, as
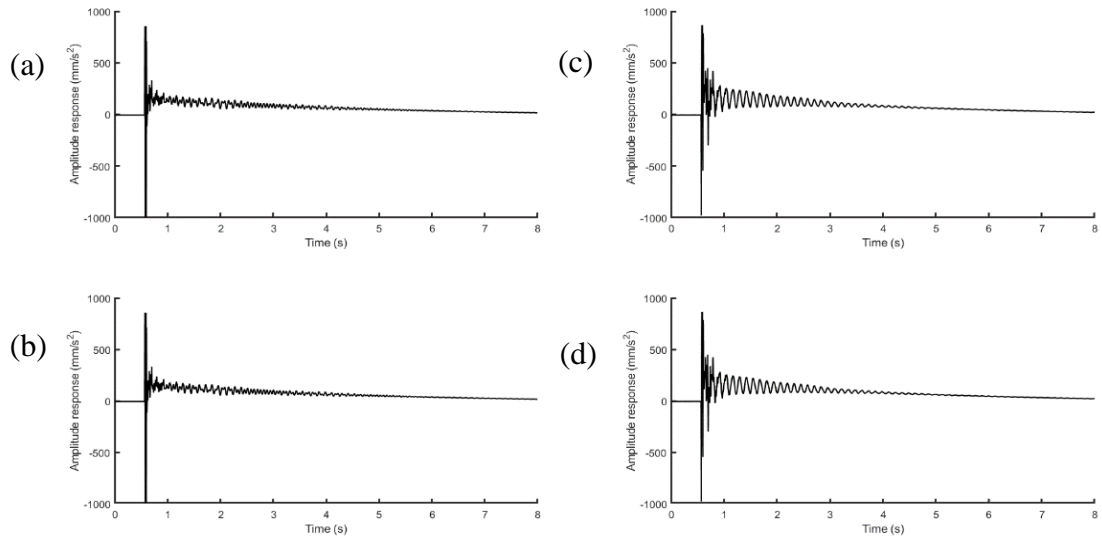
Figure 22 Time response due to cross-stream impact as measured by (a) the accelerometer in streamwise direction at the top of the cylinder, (b) the accelerometer in streamwise direction at the bottom of the cylinder, (c) the accelerometer in cross-stream direction at the top of the cylinder, and (d) the accelerometer in cross-stream direction at the bottom of the cylinder
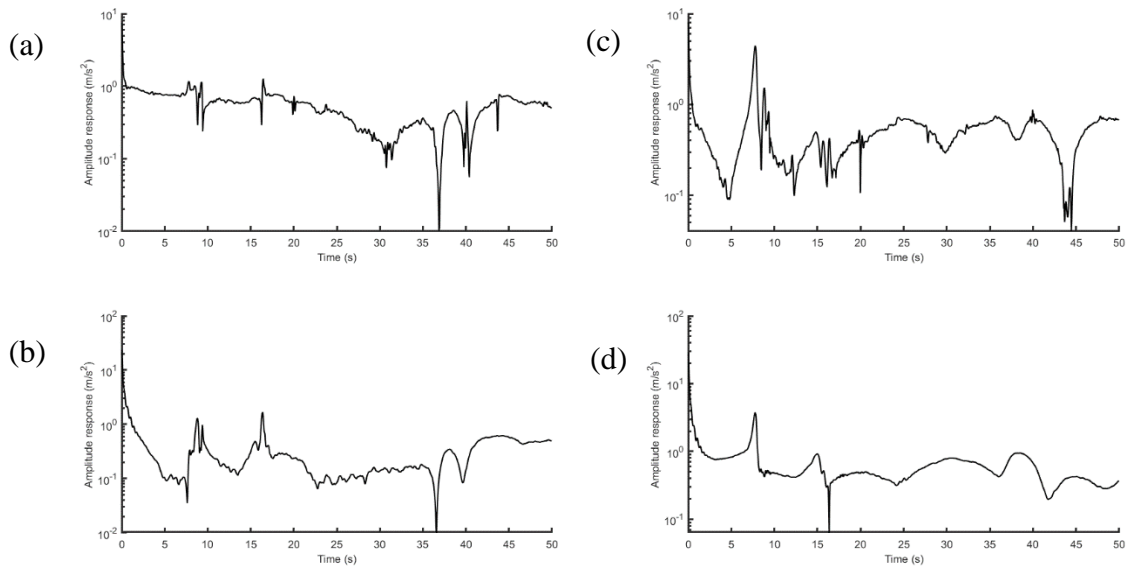

Figure 23 Acceleration logarithmic amplitude spectral response to cross-stream impact (a) in the streamwise direction at the top of the cylinder, (b) in the streamwise direction at the bottom of the cylinder, (c) in the cross-stream direction at the top of the cylinder, (d) in the cross-stream direction at the bottom of the cylinder

depicted in Figure 24. Attempts to reduce the separation region using a downstream flap

failed to eliminate the separation region. The limited extent of the separation and the

ineffectiveness of the downstream flap due to the open region above the wall in the
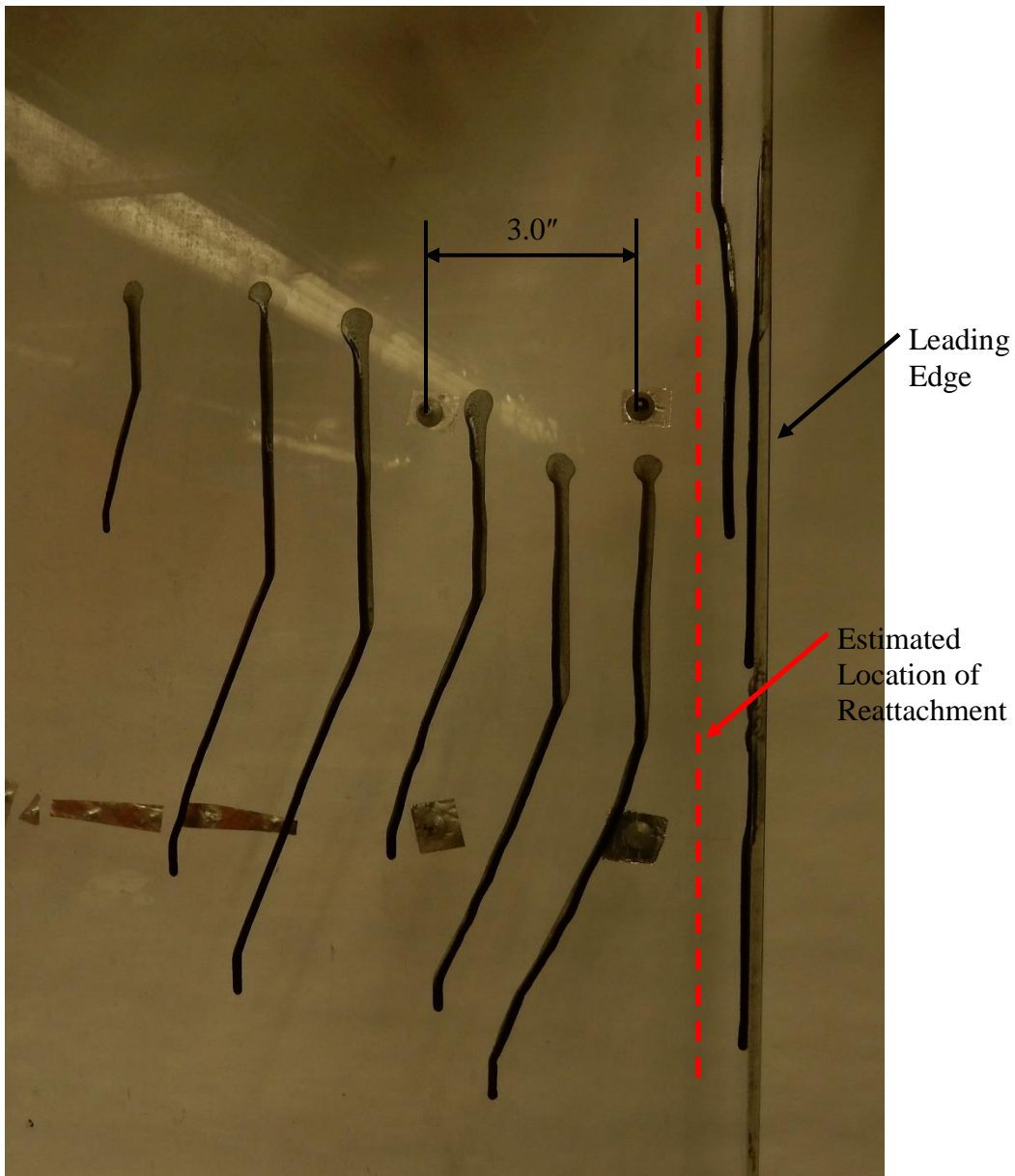

Figure 24 Flow visualization on the added wall using oil streaks showing a small leading
edge separation region

tolerant test section, resulted in a reluctant acceptance of this separation region.

Subsequently, hot wire measurements of the boundary layer on the wall 15 inches

downstream of its leading edge were made.

Figure 25 shows the measured wall boundary layer with no cylinder in the flow

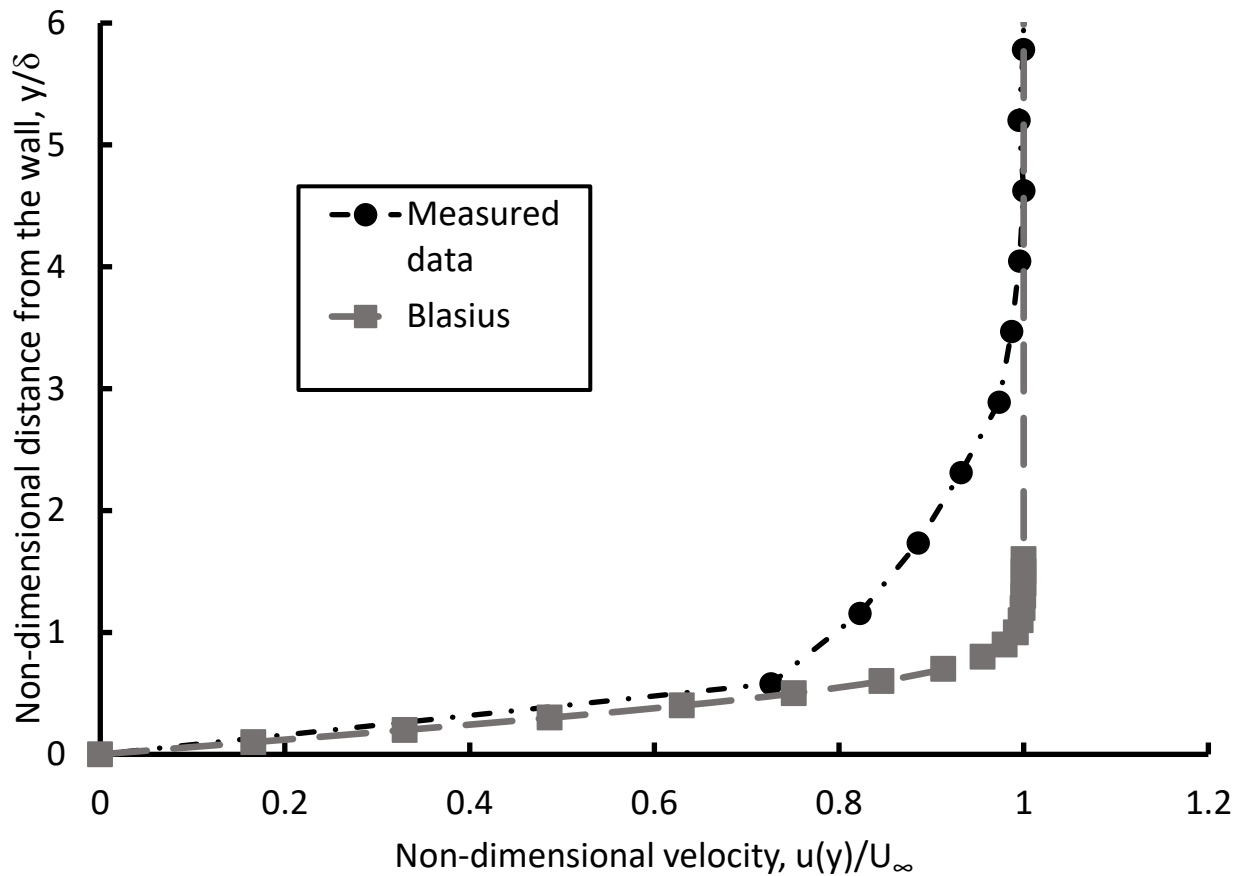along with a Blasius laminar boundary layer profile.

Figure 25 Hot wire anemometer boundary layer velocity profile measured at a streamwise distance 15 inches from the leading edge of the wall compared with a Blasius laminar boundary layer profile. Measured boundary layer thickness δ = 0.443 inches; displacement thickness δ* = 0.0689 inches; momentum thickness θ =0.0561 inches; shape factor H = 1.22.

The near wall region approximates the Blasius profile. The outer portion of the measured

boundary layer extends further into the freestream than does the Blasius profile. The

boundary layer thickness, δ, was found to be approximately 0.443 inches, with a

displacement thickness, δ^*, of 0.0689 inches and a momentum thickness, θ, of 0.0561

inches, yielding a shape factor $H = \delta^*/\theta = 1.22$. The low value of the shape factor

suggests the boundary layer is transitional or turbulent at the location where cylinder

testing was undertaken.

Cylinder Response with Flow

The fluctuating velocity was measured using a hot wire anemometer (DANTEC

Type 55R11) at a fixed point downstream of the cylinder center position and outside of

the wake of the cylinder, as shown in Figure 17. Subsequently, the fluctuating velocity

spectra were computed from the fluctuating time domain signal (with the mean value

subtracted).

The acceleration responses from two tri-axial accelerometers (PCB, Piezotronics

T356A32) provided acceleration signals from which fluctuating streamwise and cross-

stream acceleration spectra were computed and plotted. In addition, cross-spectral

amplitude and phase relations between fluctuating cross-stream (lift) acceleration and the

fluctuating velocity, as well as between fluctuating cross-stream (lift) and streamwise

accelerations, were computed. Figure 26 depicts the time domain response of the

fluctuating acceleration components as well as the velocity fluctuation. Figures 27

through 31 show the streamwise and cross-stream acceleration spectra, and the two cross-

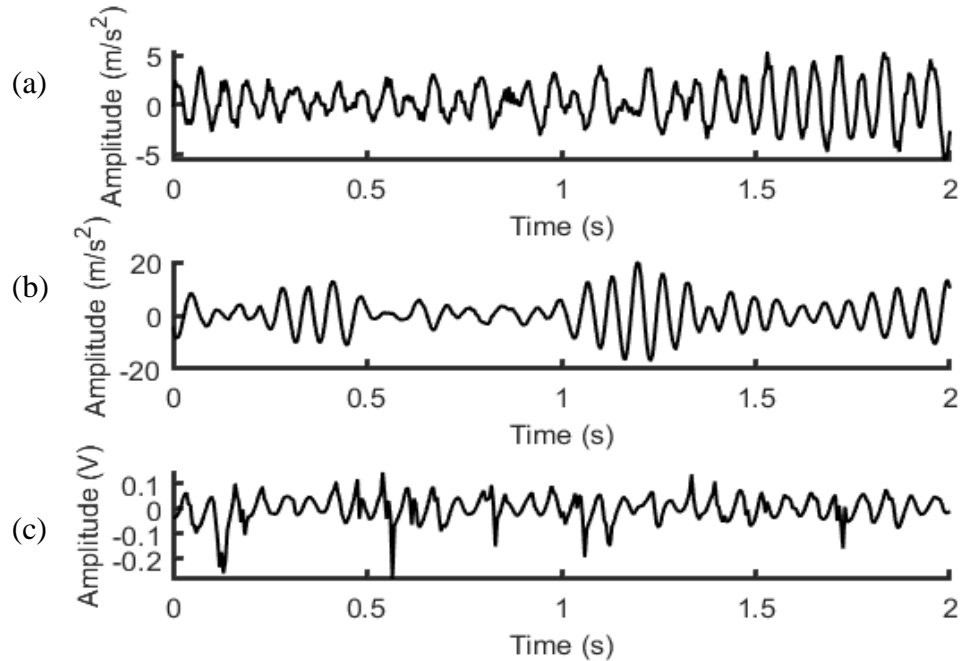spectra with the cylinder positioned at $G/D = 1.64$.

Figure 26 Time histories with $G/D = 1.64$ of (a) cylinder vibration in the streamwise direction, (b) cylinder vibration in the cross-stream direction, and (c) velocity fluctuations in the wake at $x_v/D = 2.5$, $y_v/D = 1.0$
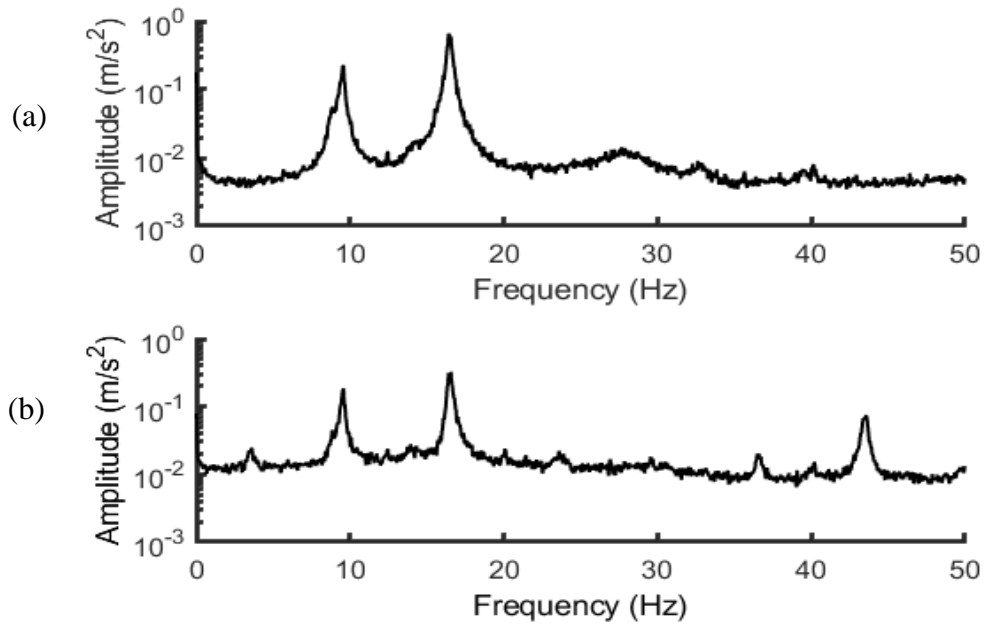

Figure 27 Streamwise (drag) acceleration amplitude spectra for gap ratio $G/D = 1.64$ from acceleration at (a) top of cylinder, and (b) bottom of cylinder
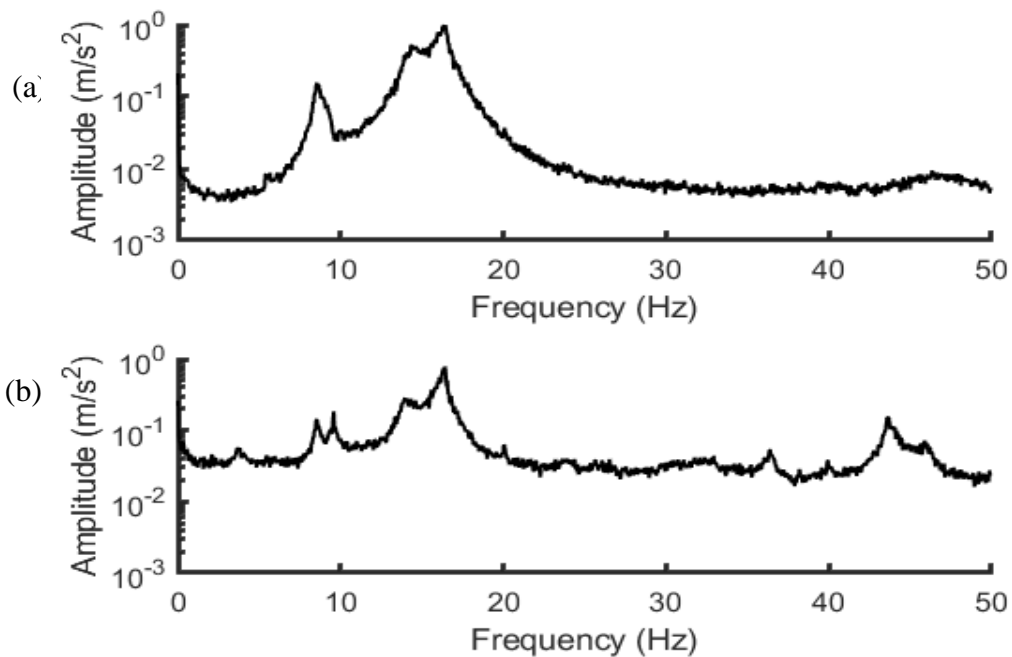
Figure 28 Cross-stream (lift) acceleration amplitude spectra for gap ratio *G/D* = 1.64 from acceleration at (a) top of cylinder, and (b) bottom of cylinder

For G/D =1.64 the cross-stream (lift) vibration seems to dominate the cylinder dynamics, with the fluctuating lift acceleration displaying a peak amplitude at a frequency of 16.41 *Hz* (Figures 27 and 28), corresponding to the cross-stream (lift) natural frequency, and a second, smaller peak close to the streamwise (drag) natural frequency, due to the previously discussed coupling resulting from system design.

From measurements made by many researchers, as discussed in Chapter 1, vortex shedding from an isolated circular cylinder is known to produce fluctuating lift at the frequency of vortex shedding and close to the natural frequency of the cylinder and a fluctuating drag at twice the lift fluctuation frequency. In the spectra shown in Figure 27 the small peak at 32.82 Hz in the fluctuating drag acceleration amplitude spectra, corresponds to the expected small vortex shedding drag fluctuation at twice the frequency

of the lift fluctuation. The fluctuating drag acceleration amplitude spectra also exhibit peaks at the lift and drag natural frequencies.

The velocity amplitude spectrum has its peak at the cross-stream natural frequency (Figure 29), corresponding to a Strouhal number of St = $f_v D//U = 0.4$, suggesting that vortex shedding drives the lift fluctuation. The vortex-induced lift dominates the vibration under these conditions, permitting the classification of this case as an IIE vibration.
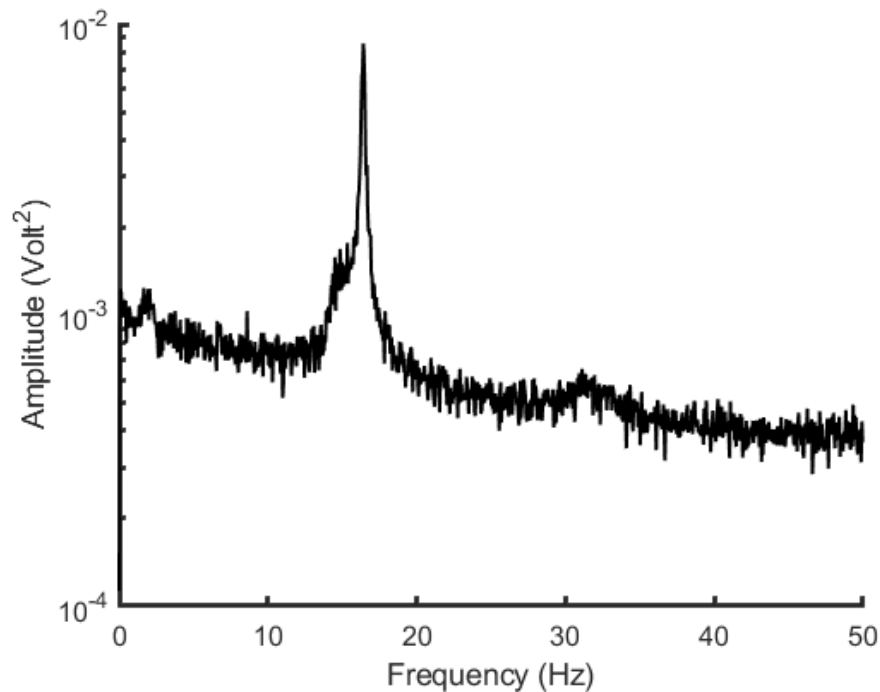

Figure 29 Fluctuating velocity spectrum with $G/D = 1.64$

The cross spectral analysis between the cross-stream acceleration and the fluctuating velocity is shown in Figure 30. The cross spectral amplitude peaks in Figure 30(a) represent frequencies that are common to both signals. The phase plot in Figure 30(b) indicates that at this particular hot wire location the velocity fluctuation lags the lift
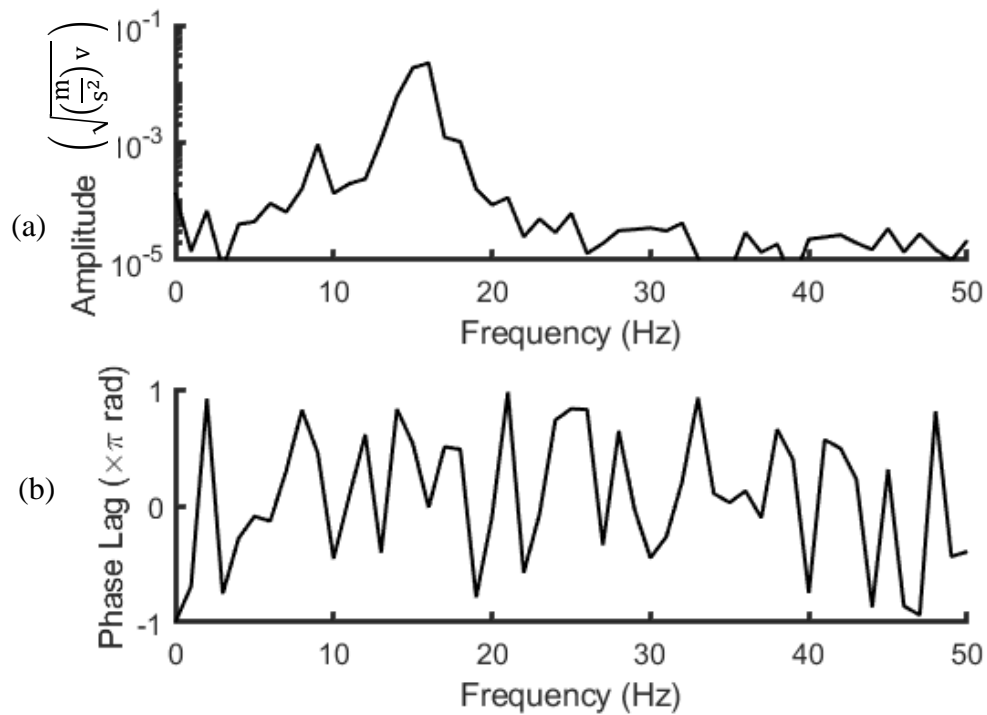
Figure 30 Cross spectral analysis of cross-stream acceleration with fluctuating velocity with G/D = 1.64, showing (a) logarithmic amplitude plot and (b) phase plot

fluctuation by about 36°. This phase angle has no particular interpretation, since the location of the hot wire is arbitrary, but by keeping the hot wire fixed relative to the cylinder position, it can be used to present the changing phase between velocity and lift as a function of G/D.

Figure 31 shows the cross spectral analysis of the cross-stream (lift) acceleration with the streamwise acceleration (drag). The dominant cross spectral peak in Figure 31(a) is at the vortex shedding frequency. Figure 31(b) shows a phase relation at this frequency of approximately 180°, suggesting that the trajectory of vibration should be elliptical with the lift acceleration at a maximum while the drag acceleration is at a minimum and vice
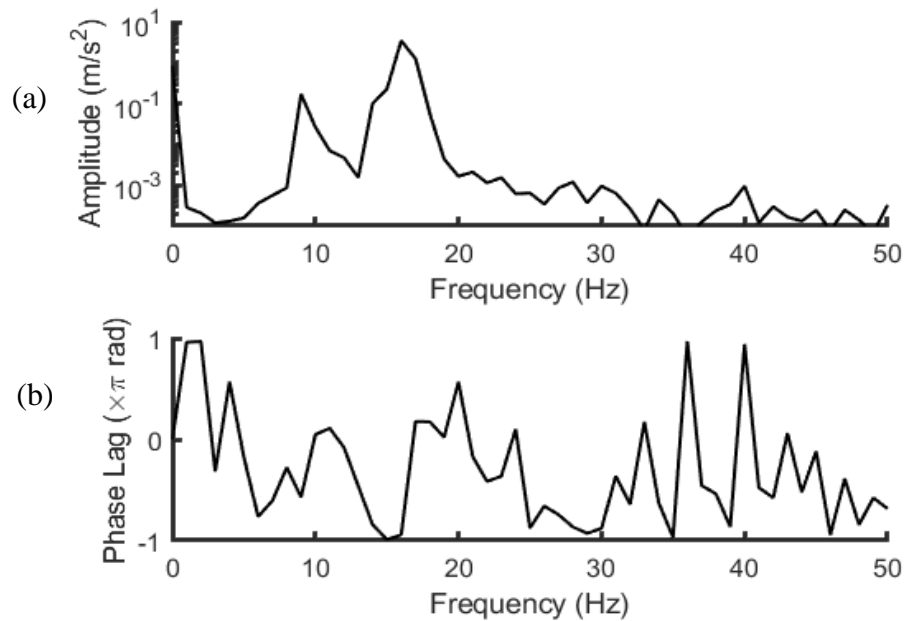
Figure 31 Cross spectral analysis of cross-stream (lift) acceleration with streamwise (drag) acceleration with $G/D = 1.64$, showing (a) logarithmic amplitude plot, and (b) phase plot

versa. Also note that at the peak near the streamwise natural frequency, the lift and drag accelerations are approximately 90° out of phase.

At decreasing G/D, the nature of the vibration is expected to remain the same until the cylinder is close enough to the wall that the symmetry of vortex shedding is disrupted. For $G/D = 1.0$, the cylinder seems to display similar frequency and phase characteristics to the ones observed for $G/D = 1.64$, as shown in Figures 32 through 37.
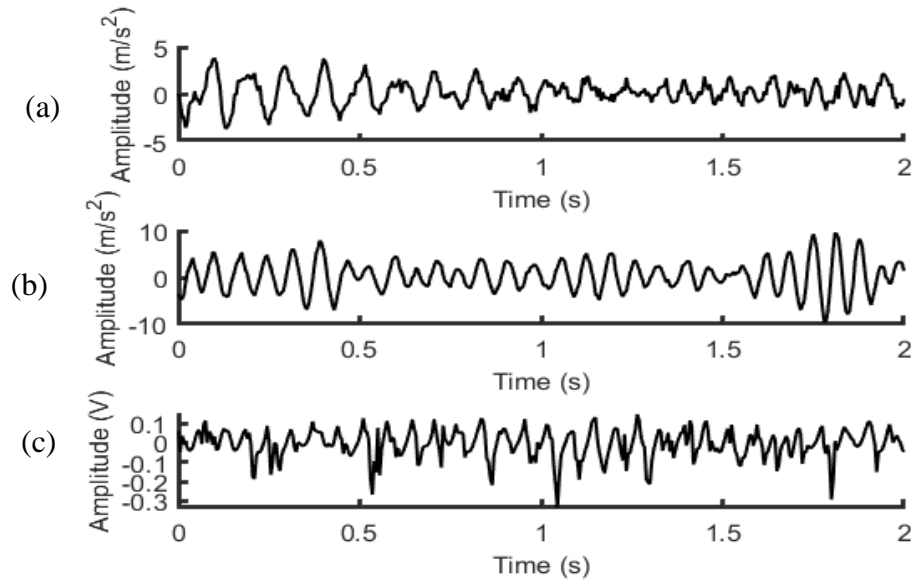
Figure 32 Time histories with $G/D = 1.0$ of (a) cylinder vibration in the streamwise direction, (b) cylinder vibration in the cross-stream direction, and (c) velocity fluctuations in the wake at $x_v/D = 2.5$, $y_v/D = 1.0$
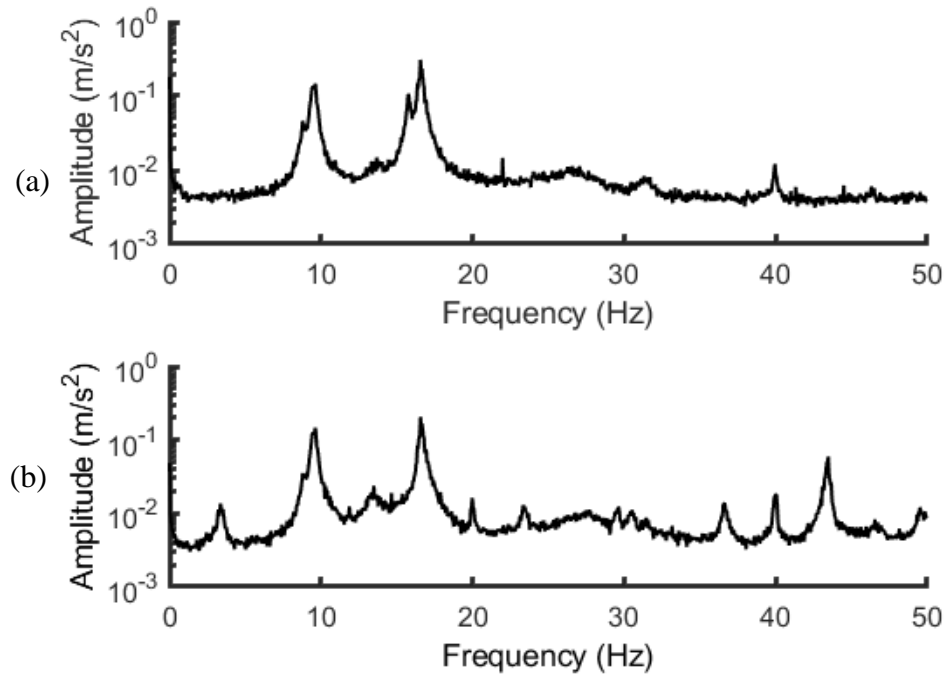

Figure 33 Streamwise (drag) acceleration amplitude spectra for gap ratio $G/D = 1.00$ from acceleration at (a) top of cylinder, and (b) bottom of cylinder
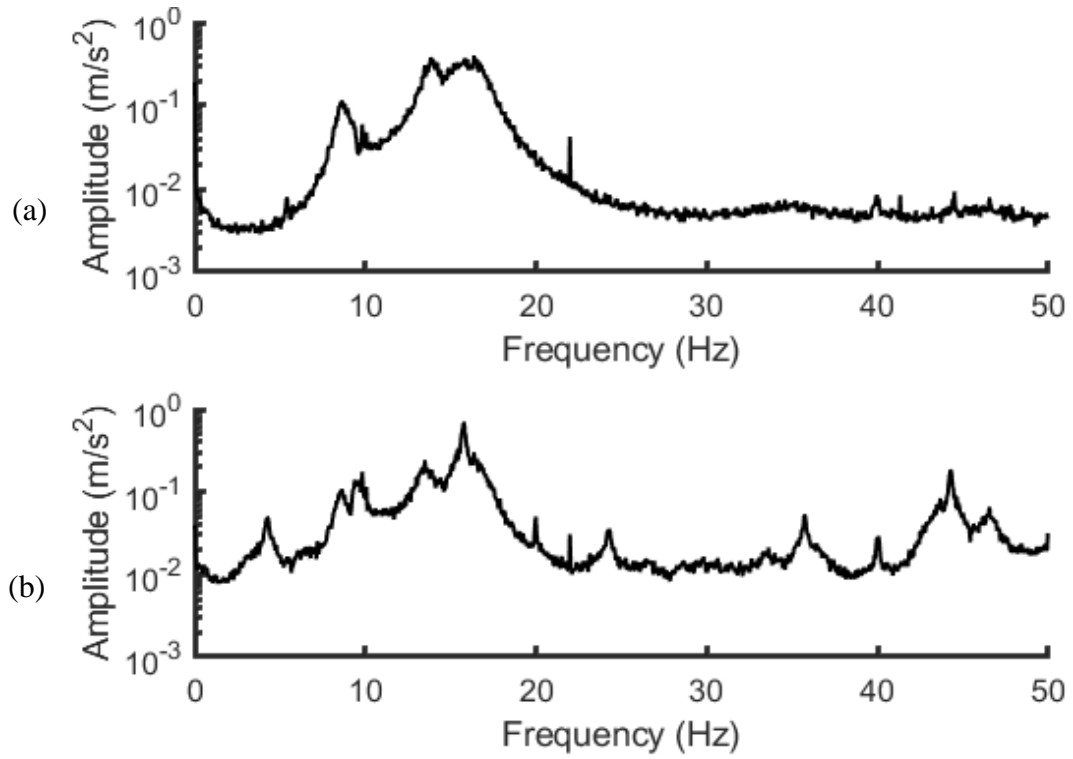
(a)

(b)

Figure 34 Cross-stream (lift) acceleration amplitude spectra for gap ratio *G/D* = 1.00
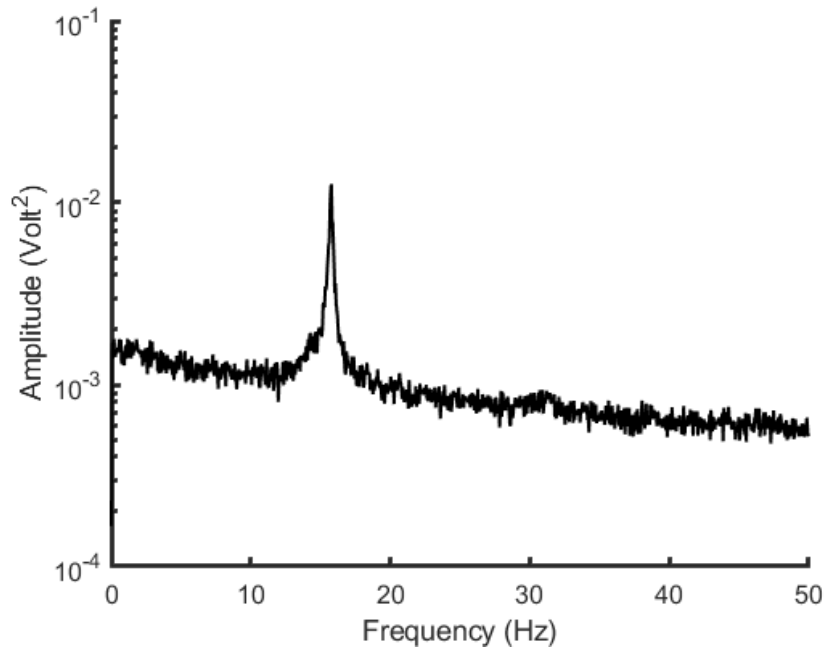

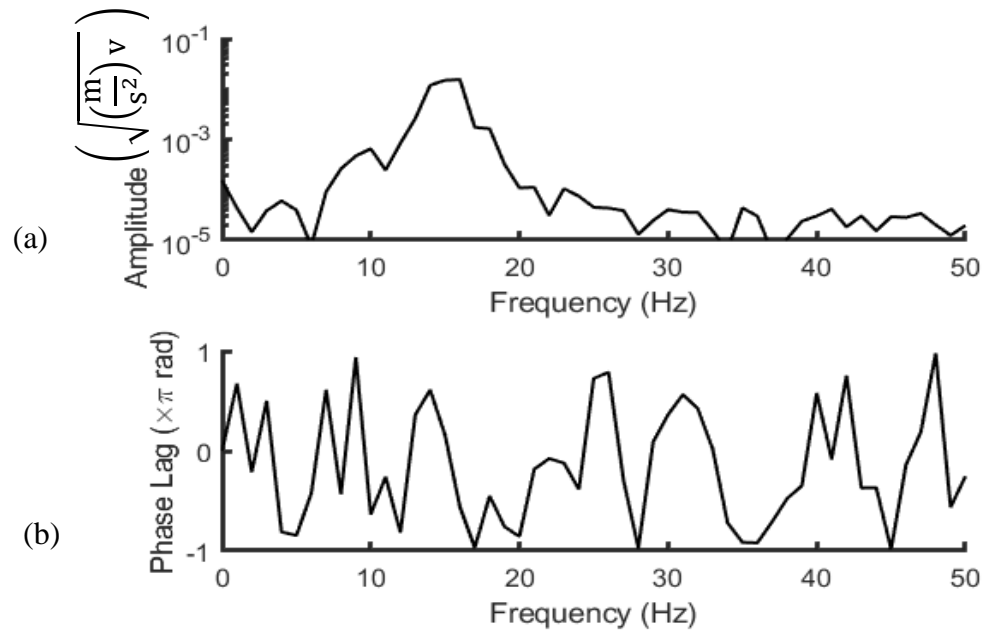Figure 35 Fluctuating velocity spectrum with *G/D* = 1.00

Figure 36 Cross spectral analysis of cross-stream acceleration with fluctuating velocity with $G/D = 1.00$, showing (a) logarithmic amplitude plot and (b) phase plot
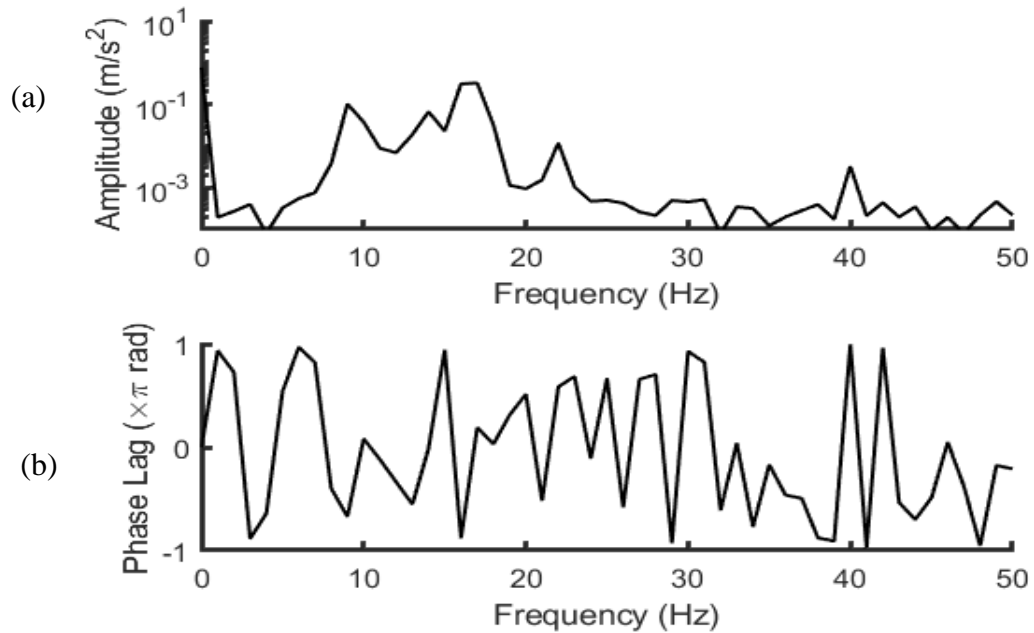

Figure 37 Cross spectral analysis of cross-stream (lift) acceleration with streamwise (drag) acceleration with $G/D = 1.00$, showing (a) logarithmic amplitude plot, and (b) phase plot
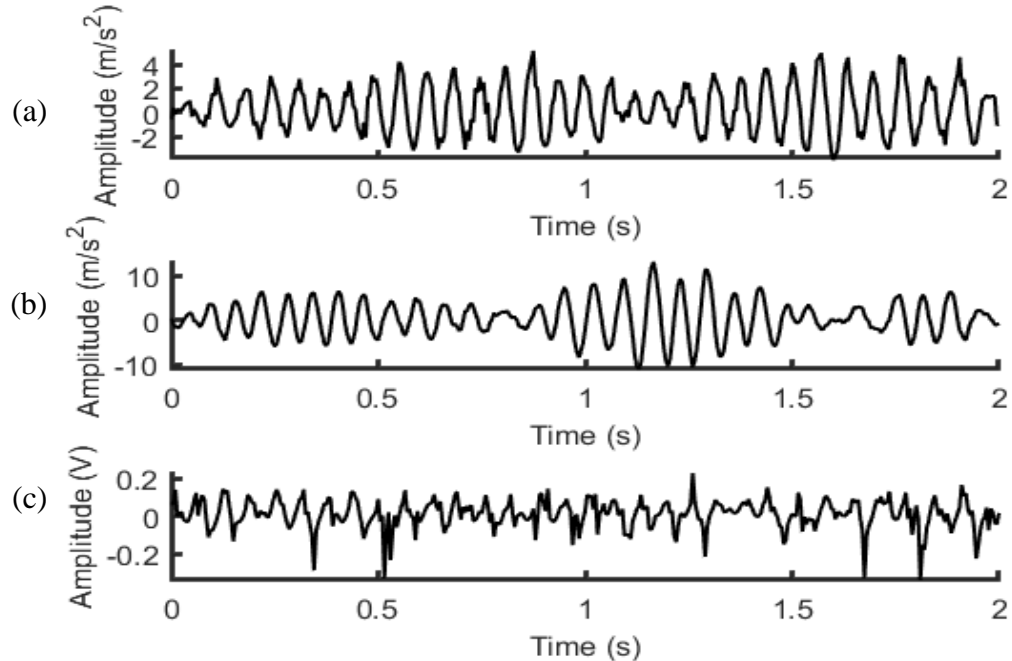
Figure 38 Time histories with $G/D = 0.4$ of (a) cylinder vibration in the streamwise direction, (b) cylinder vibration in the cross-stream direction, and (c) velocity fluctuations in the wake at $x_v/D = 2.5$, $y_v/D = 1.0$

For $G/D = 0.4$, following the same procedure as for the previous two cases, the amplitude spectra of fluctuating cross-stream (lift) and streamwise (drag) accelerations, and velocity at the same relative location were calculated and plotted (see Figures 39 to 41, respectively). In addition, the cross spectral amplitude and phase plots of cross-stream (lift) acceleration with velocity, and of cross-stream (lift) and streamwise (drag) accelerations were generated and are shown as Figures 42 and 43, respectively.
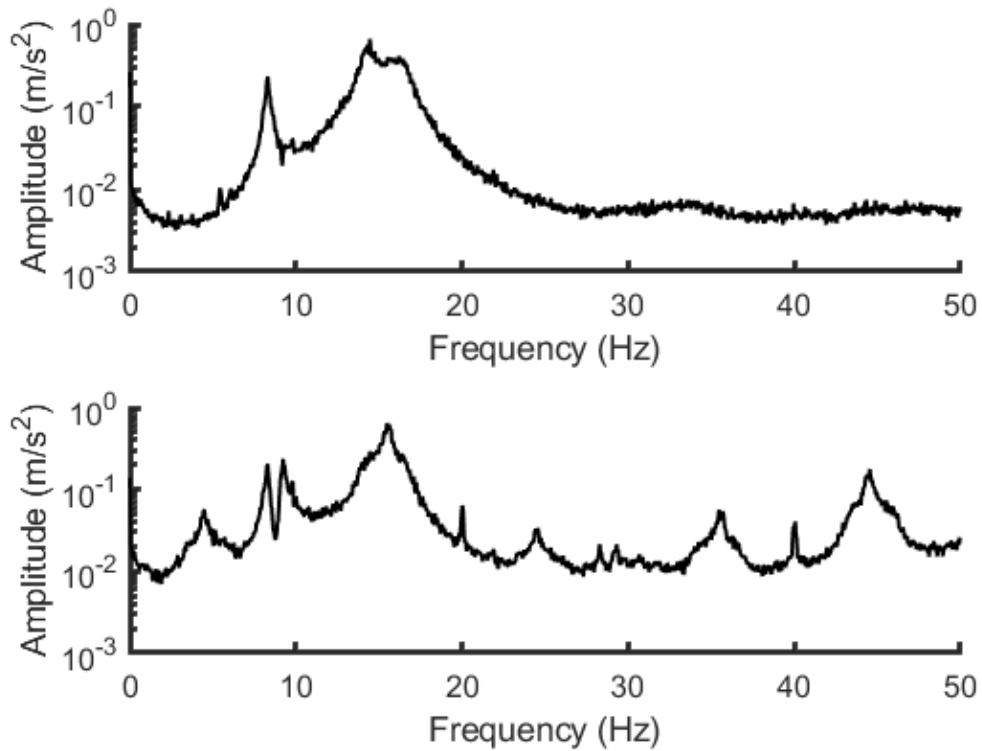
Figure 39 Streamwise (drag) acceleration amplitude spectra for gap ratio *G/D* = 0.4 from acceleration at (a) top of cylinder, and (b) bottom of cylinder
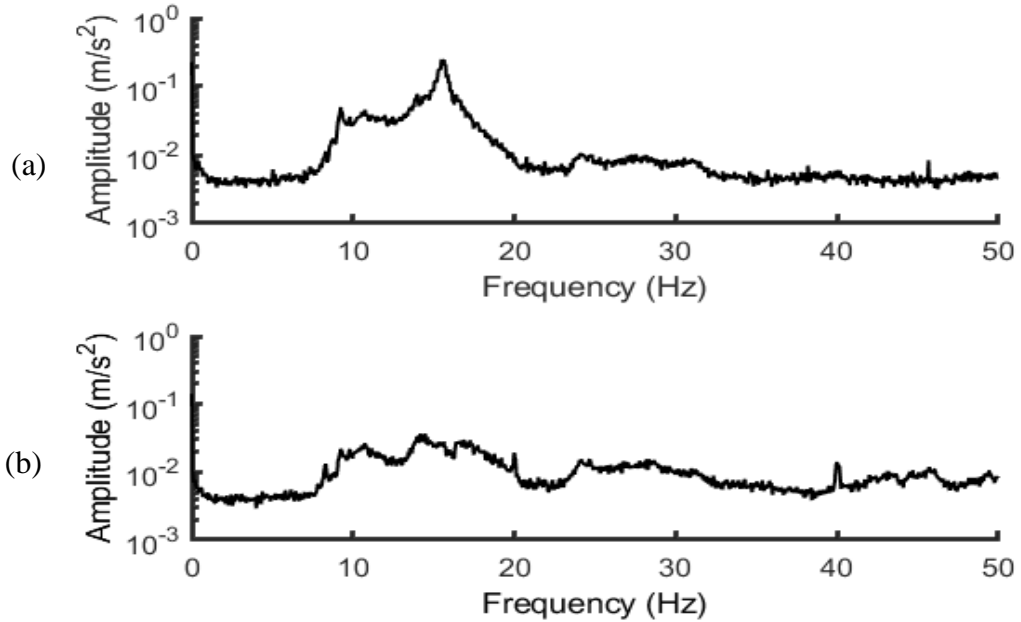

Figure 40 Cross-stream (lift) acceleration amplitude spectra for gap ratio *G/D* = 0.4 from acceleration at (a) top of cylinder, and (b) bottom of cylinder
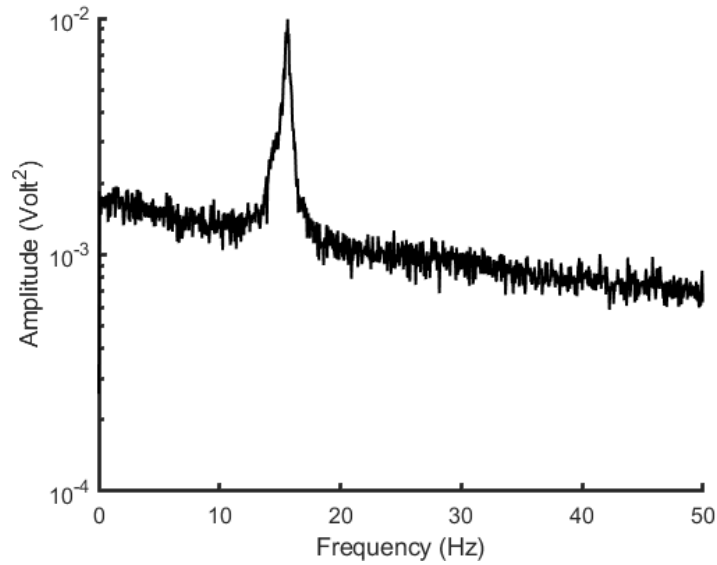
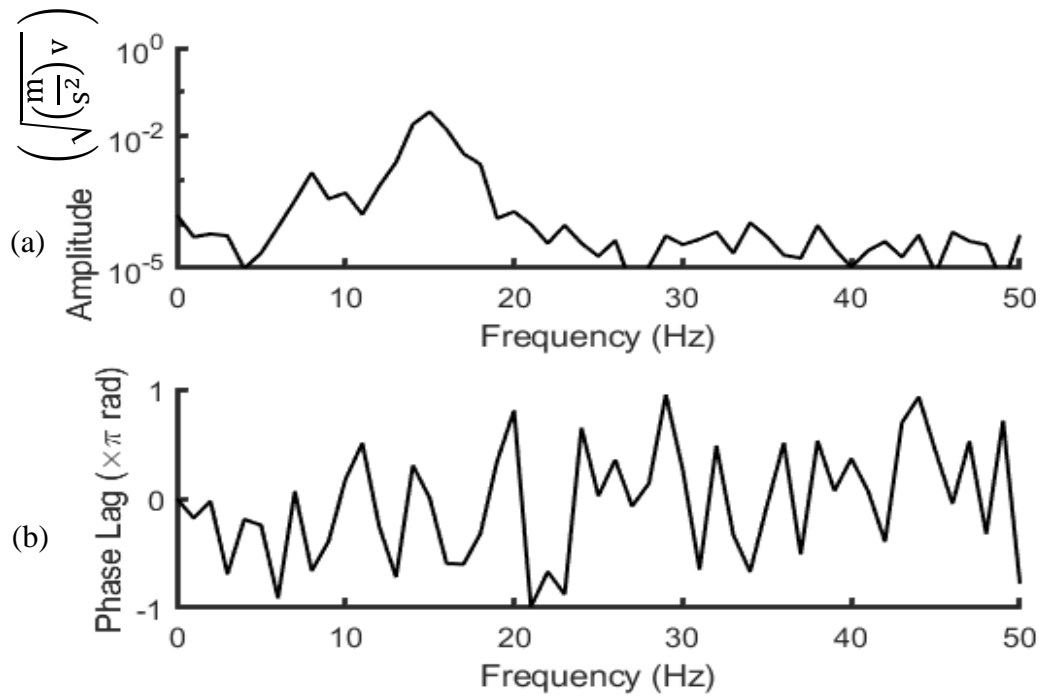Figure 41 Fluctuating velocity spectrum with *G/D* = 0.4

Figure 42 Cross spectral analysis of cross-stream acceleration with fluctuating velocity with *G/D* = 0.4, showing (a) logarithmic amplitude plot and (b) phase plot
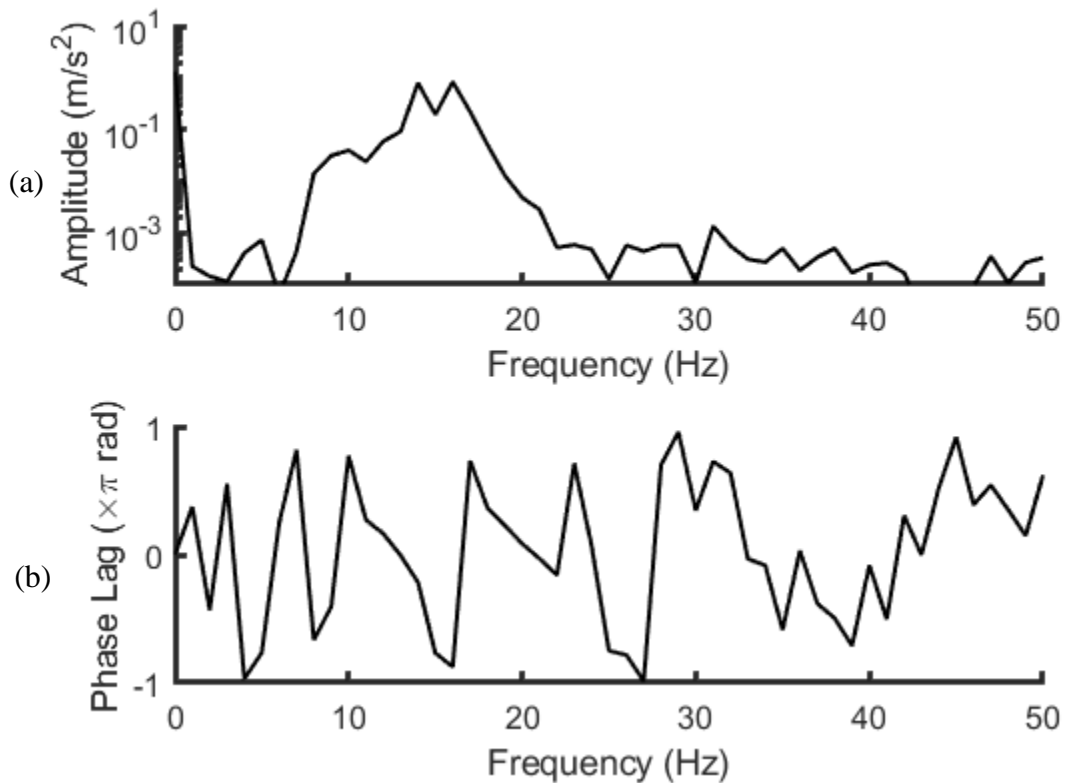
Figure 43 Cross spectral analysis of cross-stream (lift) acceleration with streamwise (drag) acceleration with *G/D* = 0.4, showing (a) logarithmic amplitude plot, and (b) phase plot

In Figure 40, the cross-stream acceleration spectra, the peak amplitude is near 15 Hz, showing a slight decrease from that shown in Figures 28 and 34. Similarly, the smaller peak near the hypothesized natural frequency of vibration in the streamwise direction occurs close to, but at a slightly lower frequency, due to the wake breathing causing a slight increase in added mass caused by the movement of the cylinder near the plane boundary. The streamwise acceleration (Figure 39) exhibits peaks at similar

frequencies to those of the cross-stream spectra, but the peaks are not quite as sharp and distinct as those in the cross-stream spectra.

The peak value in the cross-spectral amplitude (Figure 42(a)) between lift acceleration and velocity as well as that for the fluctuating lift and drag accelerations Figure 43(a), also shift to slightly lower frequency of 15 Hz that matches the apparent vortex shedding frequency, from the velocity spectrum in Figure 41. The corresponding Strouhal number is St = 0.37. The phase plot in Figure 42(b) indicates that at this particular hot wire location the velocity fluctuation leads the lift fluctuation by about 5º.

With *G/D* = 0.2, as shown in Figures 45 to 49, the mechanism of vibration has different characteristics, as anticipated. The cross-stream (lift) acceleration no longer dominates the system. The peak amplitudes for streamwise (drag) acceleration (Figure 45) as well as that for velocity (Figure 47) shift to a frequency of about 12 Hz, while the peak lift amplitude remains near the lift natural frequency (Figure 46). Note that the velocity fluctuation spectra (Figure 47) is substantially noisier than when the cylinder was at larger *G/D* ratios, as the relative position of the hot-wire was maintained.

In Figure 48, the phase angle between the lift and velocity at both the vortex shedding frequency and at the peak lift frequency show a 90º phase difference, that is, the velocity fluctuation leads (-90º phase angle) or lags (+90º phase angle), respectively, the cross-stream acceleration.
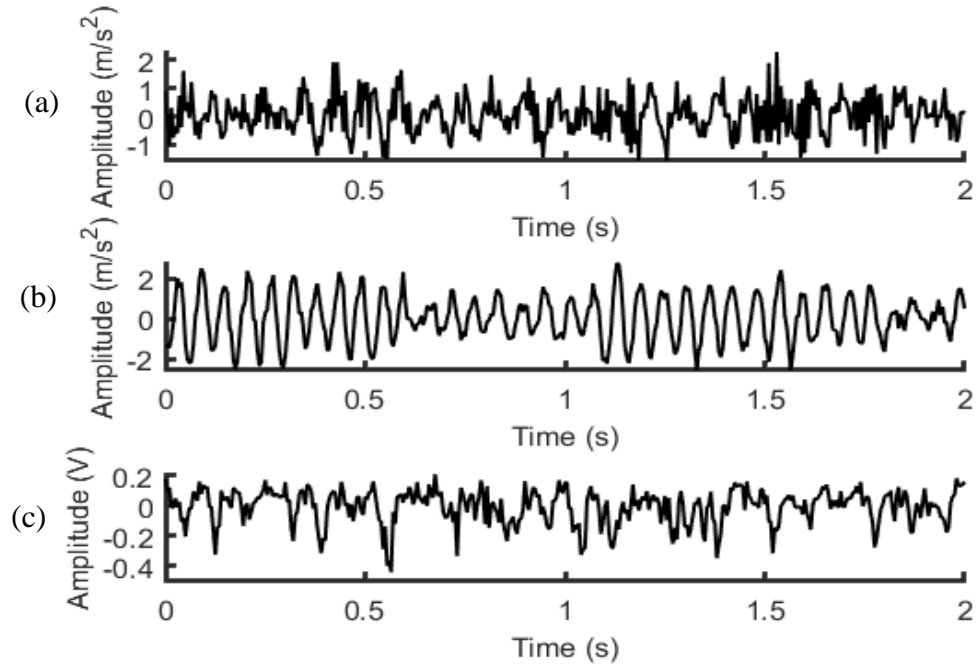
Figure 44 Time histories with $G/D = 0.2$ of (a) cylinder vibration in the streamwise direction, (b) cylinder vibration in the cross-stream direction, and (c) velocity fluctuations in the wake at $x_v/D = 2.5$, $y_v/D = 1.0$
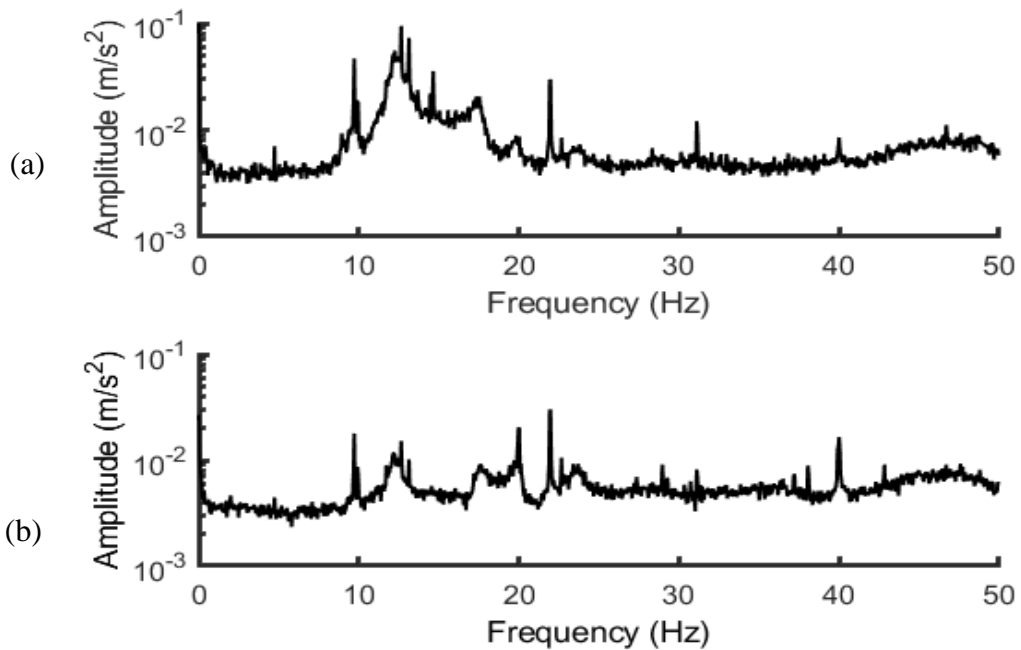

Figure 45 Streamwise (drag) acceleration amplitude spectra for gap ratio $G/D = 0.2$ from acceleration at (a) top of cylinder, and (b) bottom of cylinder
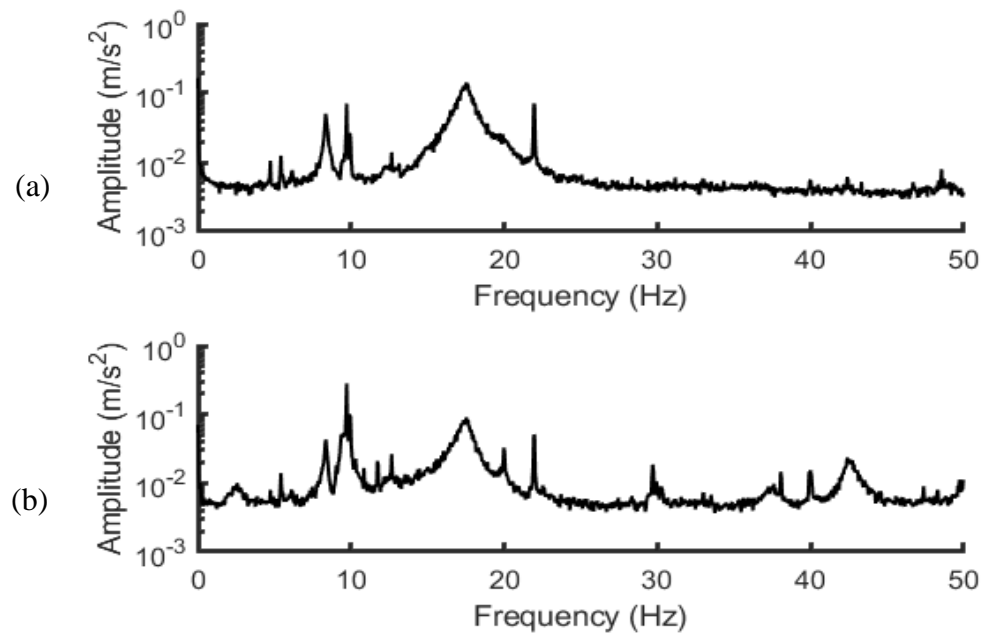
Figure 46 Cross-stream (lift) acceleration amplitude spectra for gap ratio $G/D = 0.2$ from acceleration at (a) top of cylinder, and (b) bottom of cylinder

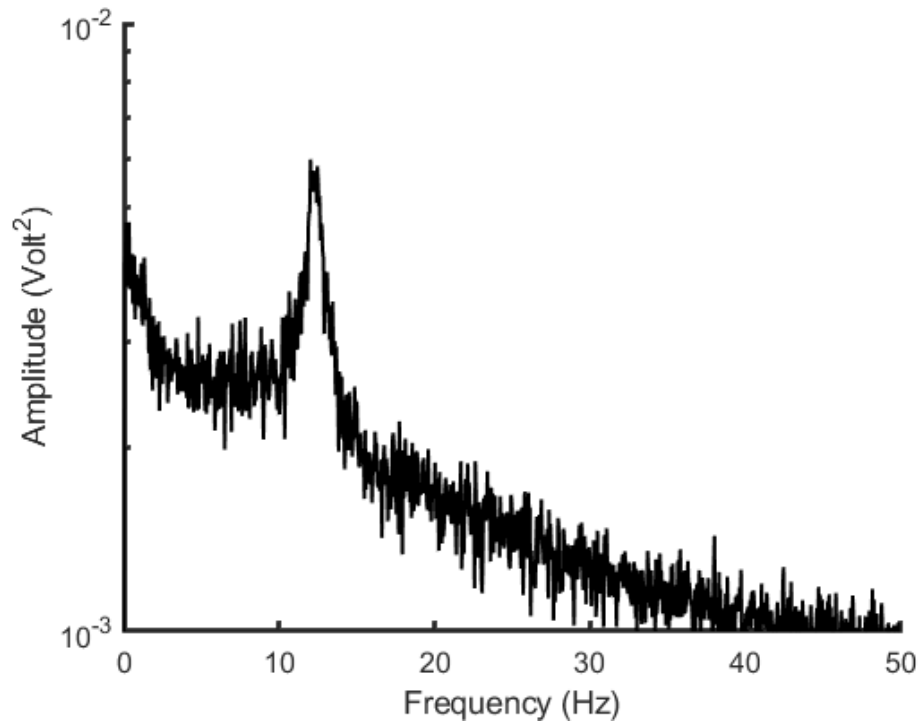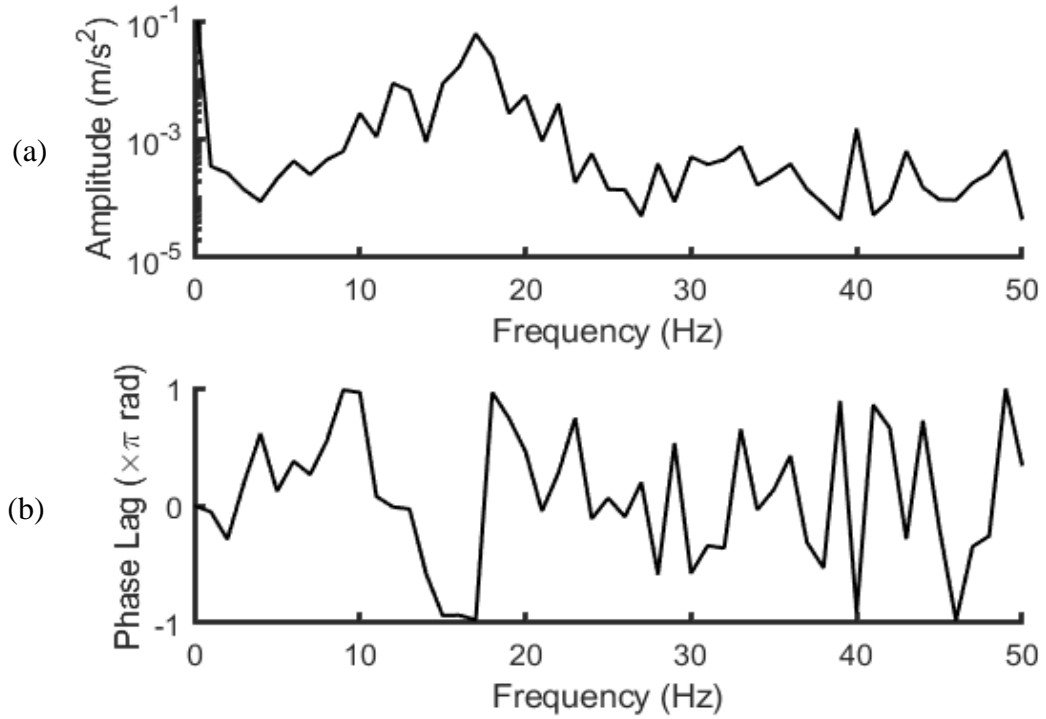Figure 47 Fluctuating velocity spectrum with $G/D = 0.2$

Figure 48 Cross spectral analysis of cross-stream acceleration with fluctuating velocity with $G/D = 0.2$, showing (a) logarithmic amplitude plot and (b) phase plot
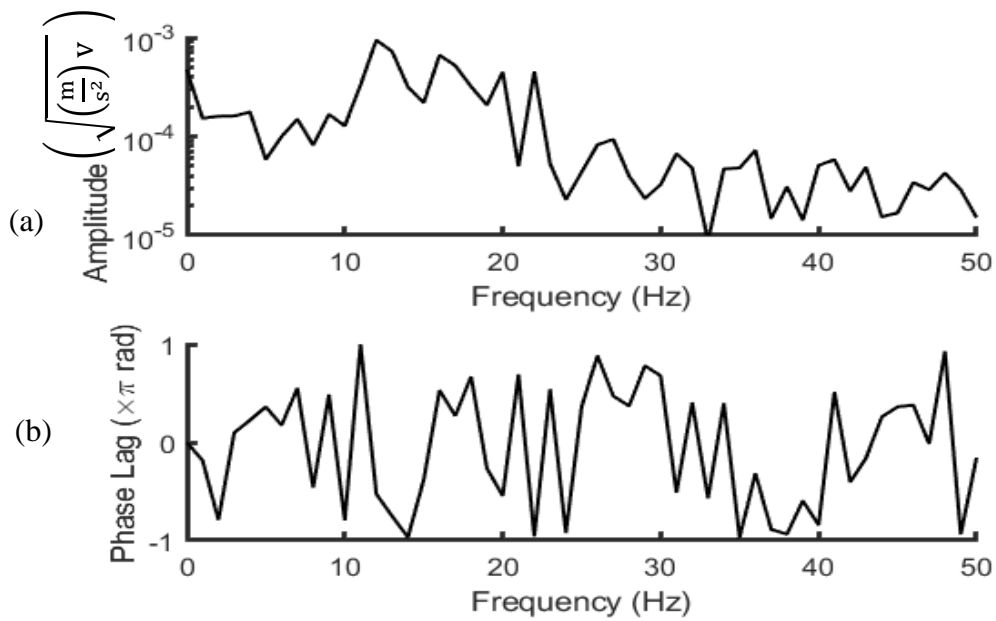

Figure 49 Cross spectral analysis of cross-stream (lift) acceleration with streamwise (drag) acceleration with $G/D = 0.2$, showing (a) logarithmic amplitude plot, and (b) phase plot
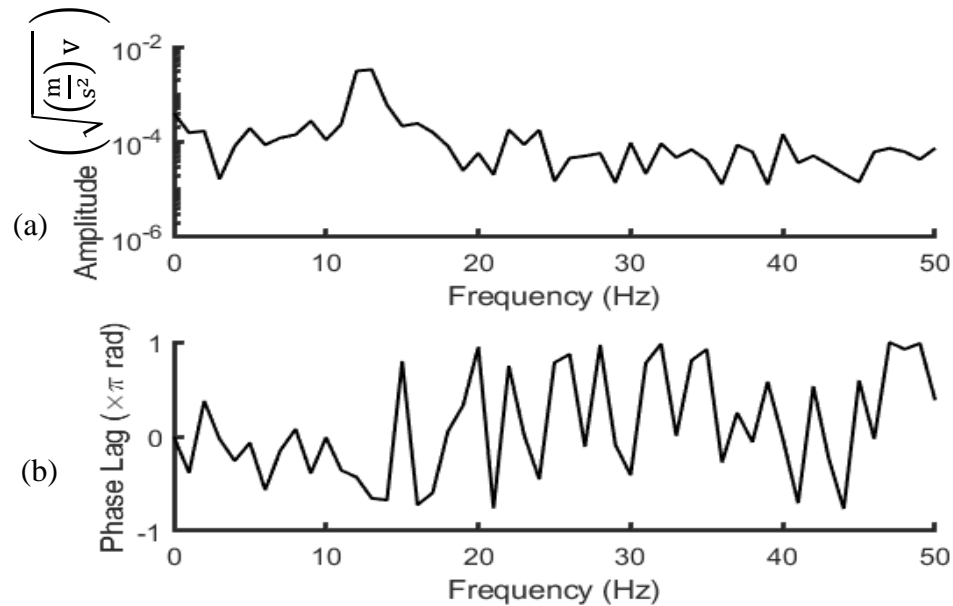
Figure 50 Cross spectral analysis of streamwise acceleration with fluctuating velocity with *G/D* = 0.2, showing (a) logarithmic amplitude plot and (b) phase plot

The cross-stream and the streamwise accelerations in Figure 49 are shown to be in phase at the vortex shedding frequency, due to a hydrodynamic coupling, while the two accelerations are 180° out of phase at the frequency closest to the natural frequency in the cross-stream direction.

In Figure 50, the cross spectral characteristics between the streamwise acceleration and the velocity fluctuation is presented. The peak, as expected is at the vortex shedding frequency and the phase angle between the streamwise acceleration and the fluctuating velocity is 92°.

A comprehensive compilation of all data sets for all *G/D* values tested (1.64, 1.5, 1, 0.75, 0.5, 0.4, 0.3, 0.2 and 0.1) can be found in Appendix B.

Summary of Dynamic Characteristics with Gap Ratio

To better understand how the dynamic characteristics change with the gap ratio, several of the factors are plotted as functions of *G/D*. Figure 51 shows a constant value of St for values of *G/D* > 0.4, and then decreasing with further reduction in gap ratio.
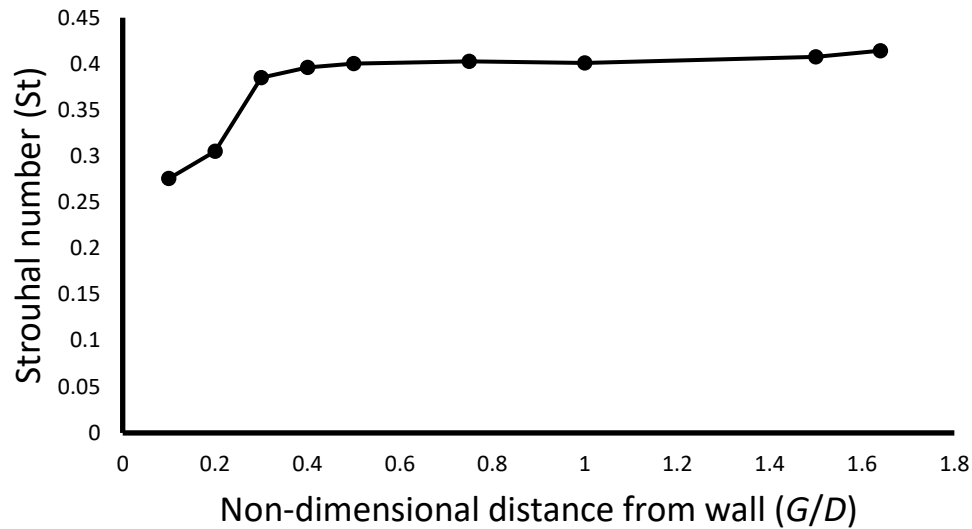

Figure 51 Strouhal number, St = *fD/U*, as a function of gap ratio

Figure 52 shows the frequency of the predominant cross-stream acceleration fluctuation, f_0, with gap ratio normalized with its value at *G/D* =1.64, denoted as f_∞. A comparison between Figures 51 and 52 shows that the cross-acceleration fluctuation changed linearly with St for large ratios up to *G/D* = 0.2, where the parameters behave differently, possibly due to MIE becoming the main mechanism of vibration near the wall.

Figure 53 shows the amplitude of cross-stream acceleration fluctuation at the predominant frequency f_0 and at twice the predominant frequency, denoted as $f_1 = 2f_0$. In addition, the amplitude of the streamwise (drag) acceleration fluctuations at both f_0 and f_1

are shown. The changes in behavior of these amplitudes summarize the hypothesized change in the nature of the forcing function from being lift dominated at larger gap ratios and drag dominated at small gap ratios.

The phase angles between cross-stream acceleration and velocity fluctuations and between cross-stream and streamwise accelerations at the frequencies f_0 and f_1 are shown in Figure 54. The velocity fluctuation phase angle relative of the cross-stream acceleration appears to be highly dependent on G/D, getting close to 0 for small gap ratios ($G/D < 0.4$), similar to what is observed for that of cross-stream acceleration relative to streamwise acceleration. The phase relative to lift at f_0 seems to decrease as G/D decreases for both the velocity fluctuation and fluctuating drag acceleration, while at f_1 the phase in relation to lift for both the velocity fluctuations and fluctuating drag acceleration seem to behave similarly far from the wall, until about $G/D = 0.75$, where
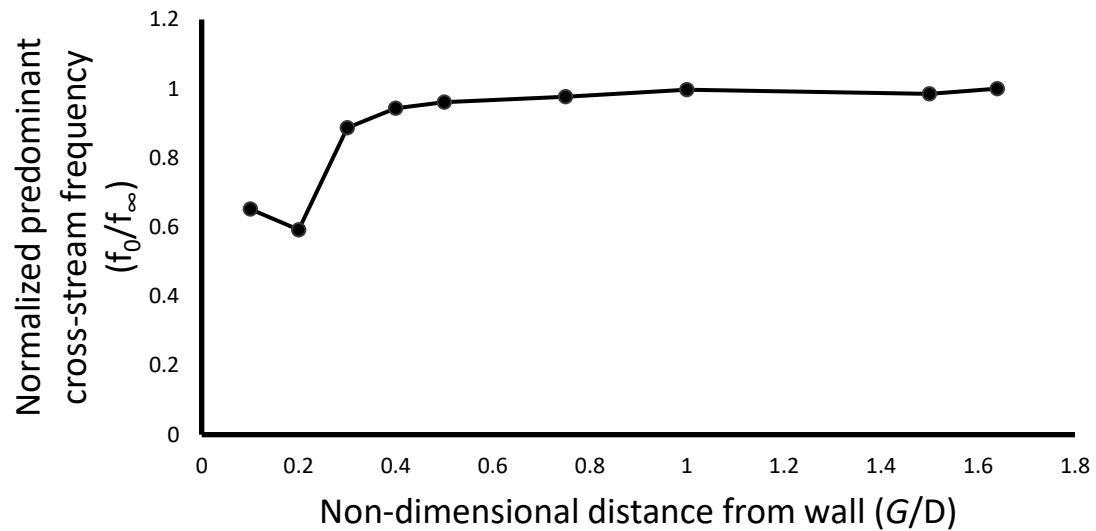

Figure 52 Predominant frequency of cross-stream acceleration fluctuation f0 /f∞ as a function of gap ratio
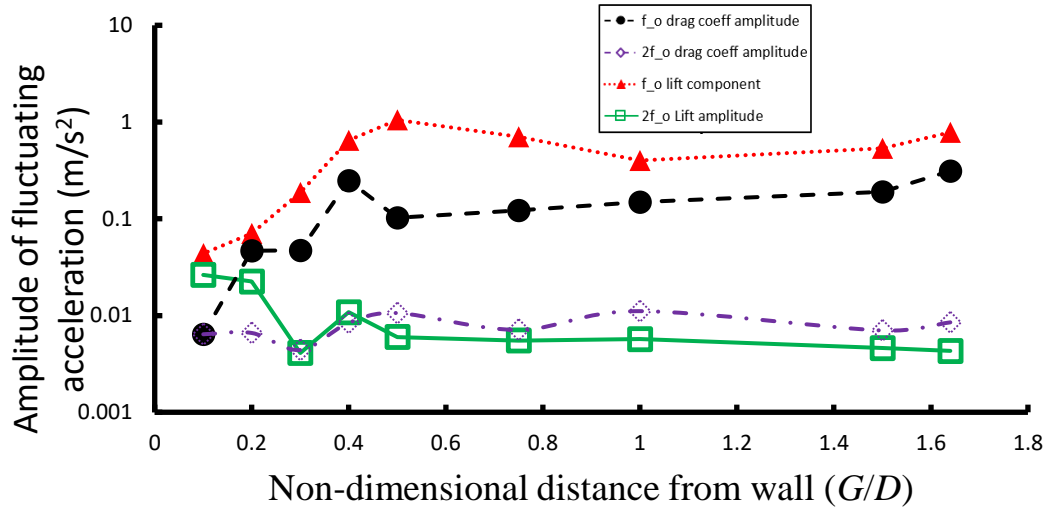
Figure 53: Fluctuating cross-stream acceleration and streamwise acceleration amplitudes at f_0 and at $f_1 = 2f_0$ as a function of gap ratio

Figure 54: Phase lags of drag relative to lift and of velocity relative to lift at f_0 and $f_1 = 2f_0$ as a function of gap ratio

the rate in which their phase lag decrease change at different ratios, with the velocity fluctuation phase in relation to lift rapidly decreasing with G/D, while the phase drag slowly decreases with gap ratio until $G/D = 0.3$, when it sharply decreases.

Chapter 4 Discussion

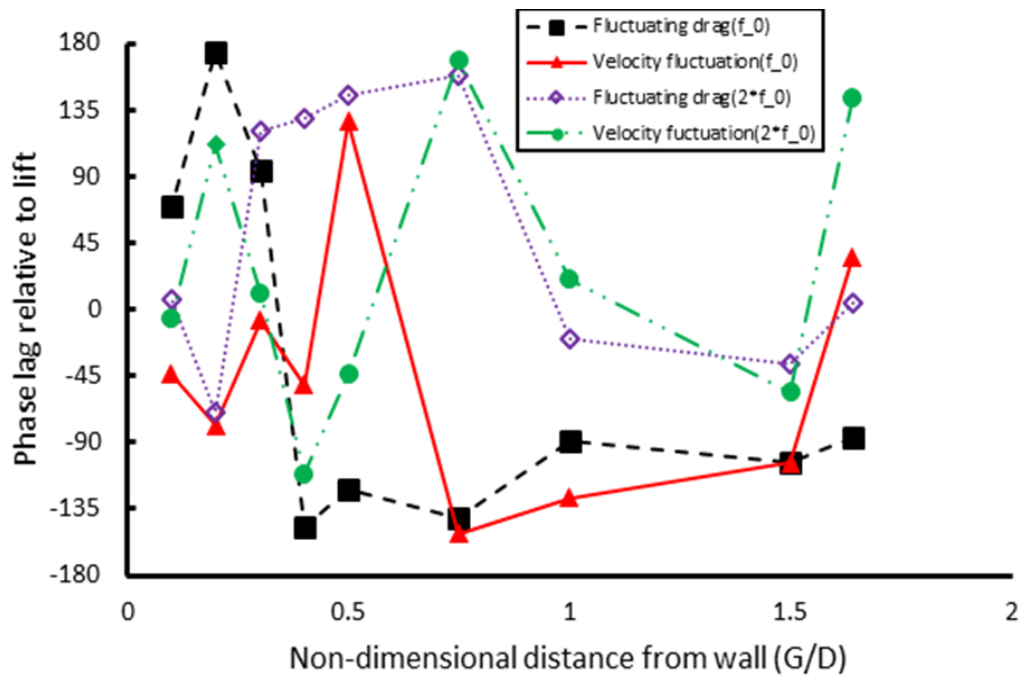An analysis of the results shown in Chapter 3 is presented in this section. Differences between the results obtained for the cylinder close to and far from the wall are discussed, highlighting possible explanation for these differences as well as presenting a comparison of the results with current literature.

Strouhal number

Far from the wall, the Strouhal number is larger than what is expected for vortex induced vibration of circular cylinders. Blockage might be one of the reasons. Awbi (1983) studied the effect of blockage on the Strouhal number of circular cylinders. He concluded that the blockage of the test section may lead to changes in Strouhal number.

The Strouhal number was calculated using the freestream velocity with zero blockage and no added wall, however, the freestream velocity is expected to increase with blockage ratio, and after the addition of the false wall, due to the area reduction. Consider the decrease in the cross-section of the test section from 17.5″ to 15″ due to the addition of the false wall, as well as the 23.3% blockage due to the cylinder. Assuming an increase of the freestream velocity inversely proportional to the area reduction, a corrected Strouhal number as a function of G/D was calculated and shown in Figure 55.
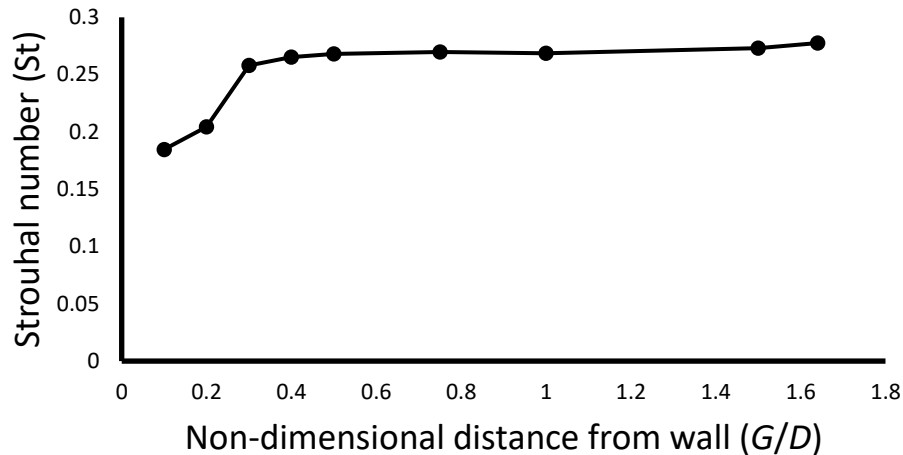
Figure 55 Strouhal number as a function of gap ratio corrected for area reduction

The increase in the frequency at which the peaks occur in fluctuating velocity and drag acceleration spectra for small values of gap ratio ($G/D = 0.2$), is possibly related to the process of wake breathing, discussed in Chapter 1. The negative damping due to the drag force acting in the direction of cylinder velocity in the wake breathing mechanism will result in an increase in the system frequency, just as system (viscous) damping produces a decrease in the system natural frequency. Thus, the increase of the frequency may possibly be explained as the result of the interaction between the wall, and the flow around the cylinder as it moves closer to the wall.

Reynolds number

The present work was undertaken at $1.8 \times 10^5 < Re_D < 1.9 \times 10^5$, depending on the density of the flow at the time of the experiments with a boundary layer thickness over diameter ratio of $\delta/D = 0.127$. Buresti & Lanciotti (1992) investigated the fluctuating and mean forces acting on a cylinder near a wall under similar characteristics, obtaining analogous results for small gap ratios. Figure 56 shows that for $Re_D = 1.89 \times 10^5$, and δ/D

= 0.1, the lift coefficient is fairly constant far from the wall, and it plummets as it

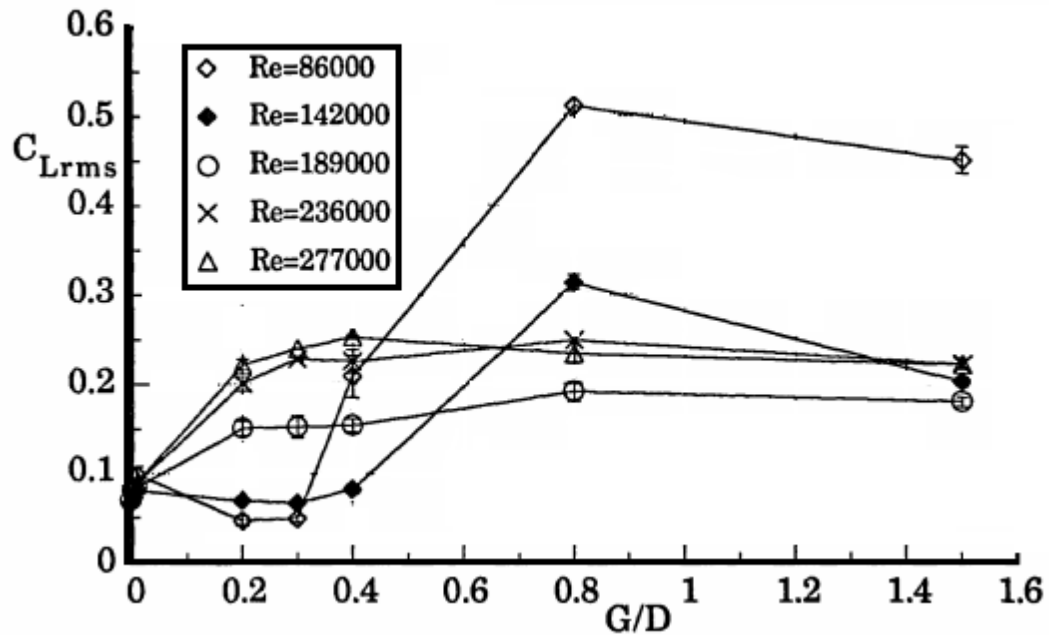approaches the wall more closely, similar to the behavior shown in Figure 53.

Figure 56 Rms lift coefficient at various gap ratios and Reynolds numbers for a boundary
layer of δ/D = 0.1

Boundary Layer

Studying the boundary layer in conjunction with the effects of the wall on the

vibration of a nearby bluff body is of great importance, as the boundary layer could have

an effect on the drag (Buresti & Lanciotti, 1992) and lift (Zdravkovich, 1985)

coefficients, as discussed in Chapter 1. The behavior of the boundary layer close to the

wall resembles a laminar flat plate boundary layer, however, at $y/D > 0.7$ it behaves

differently from the Blasius boundary layer, while not showing signs of being fully

turbulent, the shape factor $H=1.22$ indicates that the boundary layer is transitional or

turbulent (Schlichting, 1979). Buresti & Lanciotti (1992) found that for boundary layers

of $\delta/D = 0.1$, the critical gap ratio was $G/D = 0.4$, in agreement with the current study. Buresti & Lanciotti also observed a high sensitivity of transitional regimes to even small perturbations.

Stationary cylinder response

The presence of two natural frequencies, 9.3 Hz (in the streamwise direction) and 16.3 Hz (in the cross-stream direction), can be understood by considering the cylinder to be a point mass suspended on two orthogonal tensioned wires or cables. A stretched wire has a fundamental vibrational mode such that the wavelength is twice the length of the spring (Equation 16).

$$L = \frac{\lambda}{2} \tag{16}$$

where λ is the wavelength of the vibration, and L is the length of the wire. The wave velocity, v, can be expressed as:

$$v = \sqrt{\frac{T}{m/L}} \tag{17}$$

Where T is the wire tension, and m, the wire mass,(here assumed to be the point mass of the cylinder). Knowing that the frequency of vibration is the ratio between the wave velocity and wave length, the fundamental frequency can be found as:

$$f_{string} = \frac{\sqrt{\frac{T}{m/L}}}{2L} \tag{18}$$

Considering the values of $L_1 = 10''$, and $L_2 = 3.75''$ as the length of the wires, as from Figure 17 in Chapter 2, and assuming mass and tension for both wires are the same, the ratio between the streamwise and cross-stream vibration frequencies is 0.61, which

could explain the frequency ratio of 0.57 found between the streamwise (9.4 Hz) and the cross-stream (16.4 Hz) natural responses.

Cylinder response with flow

Far from the wall ($G/D > 1.0$), the fluctuating lift acceleration seems to be the dominating parameter in the vibration of the cylinder, with amplitude peak at the same frequency as that of the velocity fluctuations. Close to the wall ($G/D < 0.4$), however, the velocity fluctuation is no longer being dominated by the lift, rather it drives the drag vibration, causing the cylinder to move downstream and upstream.

When the vibration cycle moves the cylinder downstream, the wake on the side opposite to the wall expands, the base pressure on the top side of the cylinder decreases, and the stagnation point moves up, this change in the dynamics of the flow creates a negative damping effect on the upstream top side of the cylinder. When the cycle moves the cylinder upstream, the negative damping is in phase with the movement, which pushes the cylinder upstream and up.

Analogously, when the cylinder moves in the upstream direction and up, the reverse happens, stagnation point moves downward which shifts the dynamics of flow separation on the bottom side of the cylinder, when it moves up, the pressure on the region between the cylinder and the wall decreases, and as it moves up, the wake downstream of the cylinder contracts, reducing the drag effect on the cylinder and finishing the wake breathing cycle. This change on the drag coefficient is in phase with the movement of the cylinder, driving the vibration of the cylinder near the wall.

This wake breathing process seems to be in phase with the movement of the cylinder. This process is corroborated by the results of this study that showed that near the wall, the drag component fluctuation happens at the same frequency as the velocity fluctuation. This process would also explain the tendency of a cylinder near wall to move in an elliptical trajectory, moving downstream and down, and upstream and up. It is important to note that this excitation is initiated only by the movement of the cylinder, rather than the vortices shed from the far side of the cylinder.

For intermediate gap ratios ($0.4 < G/D < 1.0$), both mechanisms of vibration seem to take place on the cylinder, until the point of vortex suppression, when the movement-induced excitation drives the vibration.

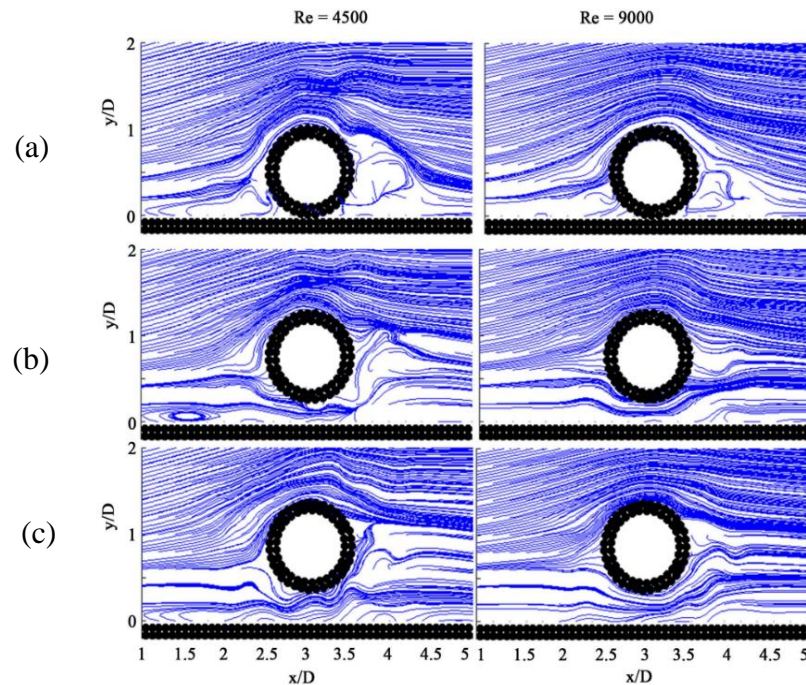Figure 57 depicts a computational model of instantaneous streamlines around a

Figure 57 Streamline contours at various Reynolds numbers, with (a) $G/D = 0$, (b) $G/D = 0.2$, and (c) $G/D = 0.3$ (from Jamalabadi & Oveisi, 2016)

cylinder near a plane boundary (Jamalabadi & Oveisi, 2016), the difference in the stagnation points can be observed.

Comparing Figure 53 and Figure 58, the fluctuating lift response close to the wall appears to behave in a similar manner to that which was measured in the work of Rao et al. (2013), which seems to validate the close to the wall response of the system.

A prediction of the behavior a circular cylinder near a wall at Re < 200 was made using a computational model as shown in Figure 58, using data from Rao et al. (2013) and iterating different phase angles between the lift and drag coefficients, to generate a
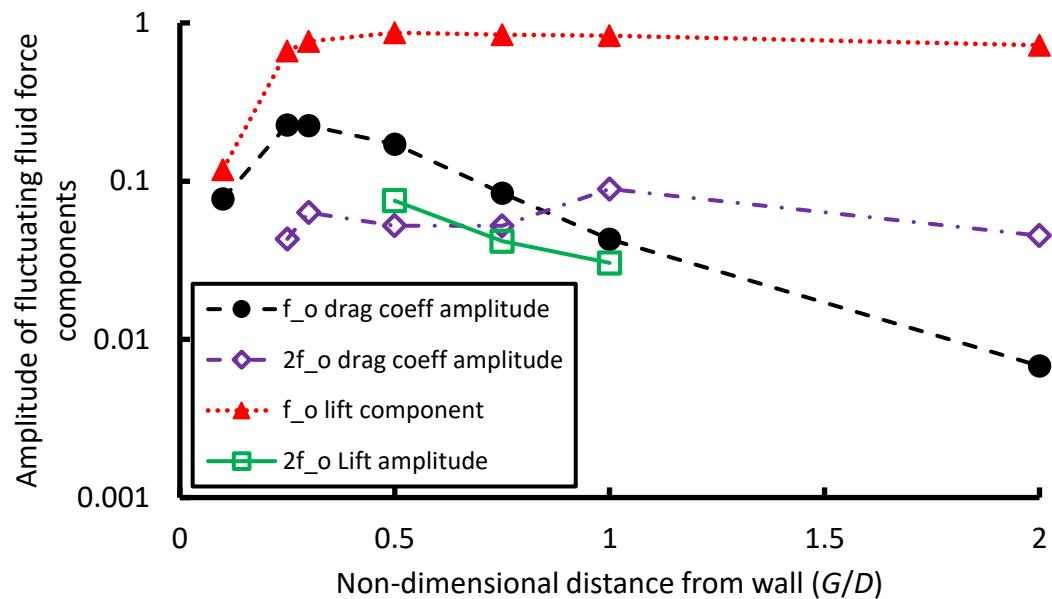

Figure 58 Amplitude of the fluctuating fluid components at the cross-stream peak frequency of vibration and at twice that peak based on a model using data from Rao's CFD computations

perfect match for their computational results. The fitted parameters from computational model based on the results from Rao et al. was compared with the findings in the present work.

Close to the wall ($G/D < 0.4$), the trends for the amplitude of fluctuating fluid components matches that of the present work, as it can be seem when compared to Figures 53 and 56. Both graphs present amplitude peaks close to the wall. Far from the wall, a substantially different behavior occurs while the lift component seems to remain constant for Rao's study, it dips a little at $G/D = 1.0$, probably due to the many nuances unaccounted on a mathematical model or some unnoticed fault while collecting the data.

Figure 53 agrees with the study of Barbosa et al. (2017), for intermediate gap ratios ($0.75 < G/D < 2$), the amplitude of vibration seems to decrease in amplitude. Both Figures 55 and 53 present peak fluctuating lift components at $G/D = 0.5$, and peak fluctuating drag components at f_0 at $G/D = 0.4$, with a drastic decrease of both fluctuating fluid forces after these peaks, likely due to the change in the mechanism of vibration.

The differences between the data of Rao et al. (2013) and the one in the study might be attributable to several slight differences. As was pointed out in previous chapters, there is a difference in Reynolds number of three orders of magnitude. Further, the 23.33% blockage of the wind tunnel might have some effect on the results. In addition, the mechanical coupling between the system response to the streamwise and cross-stream vibrations, may interfere with the frequency responses of the system.

Chapter 5 Conclusion

The present work focused on the effect of wall proximity on the mechanism of flow-induced vibration of a circular cylinder with two degrees-of-freedom, near a plane boundary at a Reynolds number of 1.86×10^5. Through the use of hot-wire anemometry and cylinder-mounted accelerometers, the flow-induced vibration of the cylinder was characterized.

Close to the wall (gap ratios, $G/D < 0.4$) the system exhibited characteristics of MIV as a result of the wake breathing mechanism, with the cylinder's wake varying in width with the motion of the cylinder, producing a fluctuating force component in phase with the cylinder velocity, increasing the excitation of the system.

For intermediate gap ratios ($0.4 > G/D > 1.0$), the excitation had characteristics of both VIV and MIV, due to the combined effects of vortex shedding and movement-induced cylinder motion near the plane boundary.

For large gap ratios ($G/D > 1.0$), shed vortices produced a fluctuation in the lift component at the vortex shedding frequency that showed a tendency to exhibit lock-in to the cylinder natural frequency, as is known to occur in vortex shedding excitation. An associated weak fluctuating drag component at twice the vortex shedding frequency was also observed.

The change in the driving mechanism of vibration from the fluctuating lift component to the movement of the cylinder near the wall is a likely explanation of how the mechanism changes near the wall; however, it is not possible to reach a definitive conclusion before all uncertainties associated with the effects of mechanical coupling and

blockage have been addressed. Movement-induced vibration near the wall, due to wake breathing is the highly likely explanation for the change in the dynamics of the flow near the wall. The experiments conducted herein provide evidence to corroborate this hypothesis.

As discussed in previous chapters, the cross-stream and streamwise vibrations are mechanically coupled far from the wall, which caused the phase relationship between the fluctuating fluid forces and velocity fluctuation to be unclear. Close to the wall, the results were consistent with a hydrodynamic mode coupling.

If the mechanical coupling between the streamwise and cross-stream vibrations could be removed (changing the springs) or accounted for, the wake breathing effect would most likely be more evident. Other constraint issues were the blockage ratio, which affected the Strouhal number, and the transitional boundary layer.

For future work, it would be necessary to undertake these experiments with a spring system that would allow for free vibration in both the streamwise and cross-stream direction, without mechanical coupling of the two degrees-of-freedom, possibly through the use of leaf springs. A smaller diameter cylinder with less blockage would be ideal, however, it is not a simple problem, as a smaller frequency would require more energy to be excited while at the same time requiring a lower velocity to match the Strouhal number requirements. Changes on the false wall in conjunction with the flap at its trailing edge to decrease or eliminate the separation could be made, as well as the addition of a trip wire upstream of the cylinder to trip the boundary layer into a o fully turbulent state. Future research in a water channel is encouraged, to study the effects of different mass

ratios on the dynamics of the cylinder in close proximity to a plane boundary, as well as

generating sufficient fluid force for excitation at low velocities.

References

Alam, M. M. 2014.The aerodynamics of a cylinder submerged in the wake of another. *Journal of Fluids and Structures* 51: 393-400.

Anami, K., Ishii, N., & Knisely, C.W. Theory of Coupled-Mode Self-Excited Vibration of Tainter Gates. *International Journal of Mechanical Engineering and Robotics Research* 3.4): 678-707.

Anami, K., Ishii, N.,. & Knisely, C.W. 2015. Dynamic stability identification of a full-scale Tainter-gate and extension of gate-opening range for operation. *ASME 2015 Pressure Vessels and Piping Conference*. American Society of Mechanical Engineers.

Arioli, G. & Gazzola, F.2015.A new mathematical explanation of what triggered the catastrophic torsional mode of the Tacoma Narrows Bridge. *Applied Mathematical Modelling* 39.2: 901-912.

Aristodemo, F., Tomasicchio, G.R.,. & Veltri, P. 2011. New model to determine forces at on-bottom slender pipelines. *Coastal Engineering* 58.3 (2011): 267-280.

Awbi, H. B. 1983. Effect of blockage on the Strouhal number of two-dimensional bluff bodies. *Journal of Wind Engineering and Industrial Aerodynamics, 12(3)*, 353-362.

Barbosa, J. M., Yang Q., Metrikine, A. V., & Lourens, E.M. 2017. Vortex-induced vibrations of a freely vibrating cylinder near a plane boundary: experimental investigation and theoretical modelling. *Journal of Fluids and Structures* 69: 382-401.

Bearman, P. W. & Zdravkovich, M.M. 1978. Flow around a circular cylinder near a plane boundary. *Journal of Fluid Mechanics* 89.1: 33-47.

Bendat, J. S. & Piersol, A.G. 2011. *Random Data: Analysis and Measurement Procedures*. Vol. 729. John Wiley & Sons.

Billeter, P. & Staubli, T. 2000. Flow-induced multiple-mode vibrations of gates with submerged discharge. *Journal of Fluids and Structures* 14.3): 323-338.

Bimbato, A. M. , Alcântara Pereira L.A., & Hirata, M.H. 2011. Study of the vortex shedding flow around a body near a moving ground. *Journal of Wind Engineering and Industrial Aerodynamics* 99.1: 7-17.

Blevins, R. D. 1990. *Flow-induced Vibration*. .Publisher

Bokaian, A. 1995. Interference galloping of a circular cylinder near a plane boundary. *Journal of Sound and Vibration* 181.3: 431-445.

Bokaian, A. & Geoola, F. 1985. Wake displacement as cause of lift force on cylinder pair. *Journal of Engineering Mechanics* 111.1: 92-99.

Buresti, G. & Lanciotti, A. 1992. Mean and fluctuating forces on a circular cylinder in cross-flow near a plane surface. *Journal of Wind Engineering and Industrial Aerodynamics* 41.1-3 (1992): 639-650.

Gopalkrishnan, R. 1993. *Vortex-induced Forces on Oscillating Bluff Cylinders*. No. WHOI-92-38. Woods Hole Oceanographic Institution MA, 1993.

Grass, A. J., Raven, P. W. J., Stuart, R. J., & Bray, J. A. 1984. The influence of boundary layer velocity gradients and bed proximity on vortex shedding from free spanning pipelines. *Journal of Energy Resources Technology* 106.1: 70-78.

Hourigan, K., Rao A., Brøns, M., Leweke, T., & Thompson, M.C. .2013. Vorticity generation and wake transition for a translating circular cylinder: wall proximity and rotation effects. *Journal of Wind Engineering and Industrial Aerodynamics* 122: 2-9.

Hover, F. S., Techet, A. H., & Triantafyllou, M. S. 1998. Forces on oscillating uniform and tapered cylinders in cross flow. *Journal of Fluid Mechanics 363*, 97-114.

Jamalabadi, M. A., & Oveisi, M. 2016. Numerical simulation of interaction of a current with a circular cylinder near a rigid bed. *Journal of Applied Mathematics and Physics*, *4*(02), 398.

Lei, L., Cheng, L., & Kavanagh, K. Re-examination of the effect of a plane boundary on force and vortex shedding of a circular cylinder. *Journal of Wind Engineering and Industrial Aerodynamics* 80.3 (1999): 263-286.

Morrison, J. R., O'Brien, M. P., Johnson, J. W., & Schaaf, S. A. 1950. The force exerted by surface waves on piles. Petroleum Transaction, 189, 149-157.

Naudascher, E., & Rockwell, D.. 1994. *Flow-induced Vibrations*, Dover Publications Inc.: Mineola, New York.

Nishino, T., Roberts, G.T., & Zhang,X. 2007. Vortex shedding from a circular cylinder near a moving ground. *Physics of Fluids* 19.2: 025103.

Oner, A. A., Kirkgoz, M.S.,.& Akoz, M.S. 2008. Interaction of a current with a circular cylinder near a rigid bed. *Ocean Engineering* 35.14-15: 1492-1504.

Ralston, L. M. 1997. *An Experimental Study on Passive Control of a Reattaching Shear Layer Behind a Backward-Facing Step*. M.S. Thesis, Bucknell University.

Rao, A., Thompson, M. C., Leweke, T., & Hourigan, K. 2013. The flow past a circular cylinder translating at different heights above a wall. *Journal of Fluids and Structures* 41: 9-21.

Scanlan, R. H., & Sabzevari, A. 1967. Suspension Bridge Flutter Revisited, ASCE Str. *Eng'g Conf./Seattle, Washington*.

Scanlan, R. H., & Sabzevari, A. 1969. Experimental aerodynamic coefficients in the analytical study of suspension bridge flutter. *Journal of Mechanical Engineering Science* 11.3: 234-242.

Scanlan, R. H., & Tomko, J.J. 1971. Airfoil and bridge deck aerodynamic parameters. *J. Engineering Mechanics* 97.6: 1171-1737.

Sumer, B. M. 2006. *Hydrodynamics around cylindrical strucures*. Vol. 26. World Scientific.

Sumer, B. M., Jensen, B.L. &s Fredsøe, J. 1991. Effect of a plane boundary on oscillatory flow around a circular cylinder. *Journal of Fluid Mechanics* 225: 271-300.

Sumer, B. M., Fredsøe, J., Jensen, B. L., & Christiansen, N. 1994. Forces on vibrating cylinder near wall in current and waves. *Journal of Waterway, Port, Coastal, and Ocean Engineering* 120.3: 233-250.

Sumner, D. 2010. Two circular cylinders in cross-flow: a review. *Journal of Fluids and Structures* 26.6: 849-899.

Sumner, D., Wong, S. S. T., Price, S. J., & Paidoussis, M. P. 1999. Fluid behaviour of side-by-side circular cylinders in steady cross-flow. *Journal of Fluids and Structures* 13.3: 309-338.

Valentine, D. T., &s Madhi, F. 2012. Potential Flow Theory and Numerical Analysis of Forces on Cylinders Induced by Oscillating Disturbances. *Journal of Offshore Mechanics and Arctic Engineering* 134.3: 031301.

Weaver, D.S., &s Fitzpatrick, J.A.1988. A review of cross-flow induced vibrations in heat exchanger tube arrays. *Journal of Fluids and Structures* 2.1: 73-93.

Williamson, C. H. K. 1985. Sinusoidal flow relative to circular cylinders. *Journal of Fluid Mechanics* 155: 141-174.

Yang, B., Gao, F. P., Wu, Y. X., & Li, D. H. 2006. "Experimental study on vortex-induced vibrations of submarine pipeline near seabed boundary in ocean currents." *China Ocean Engineering* 20.1: 113.

Yang, B., Gao, F., Jeng, D. S., & Wu, Y. 2009. "Experimental study of vortex-induced vibrations of a cylinder near a rigid plane boundary in steady flow." *Acta Mechanica Sinica* 25.1: 51-63.

Zdravkovich, M. M. 1977. Review of flow interference between two circular cylinders in various arrangements. *Journal of Fluids Engineering* 99.4: 618-633.

Zdravkovich, M. M. 1985. Forces on a circular cylinder near a plane wall. *Applied Ocean Research* 7.4: 197-201.

Appendix A: Wind Tunnel Characteristics

From earlier work in the same wind tunnel (Ralston, 1997), the velocity profiles along the vertical and horizontal center lines were known to be uniform, except near the top and bottom as well as near the front and back walls of the test section.

A hot-wire anemometer was positioned in the test section of the wind tunnel, mean velocity on the centerline as a function of percent speed and density was collected and explained on Chapter 3.

The mean velocity profiles were then measured with data being collected in the vertical centerline, the horizontal centerline and in the axial centerline.

A one dimensional RMS profile of the centerline measurements was calculated. And used to solve for the turbulence intensity and the mean velocity profile was traced for all centerlines.

Figure A1 depicts the velocity and turbulence intensity profile for (a) the vertical centerline, (b) the horizontal centerline, and (c) the axial (streamwise) centerline of the wind tunnel.
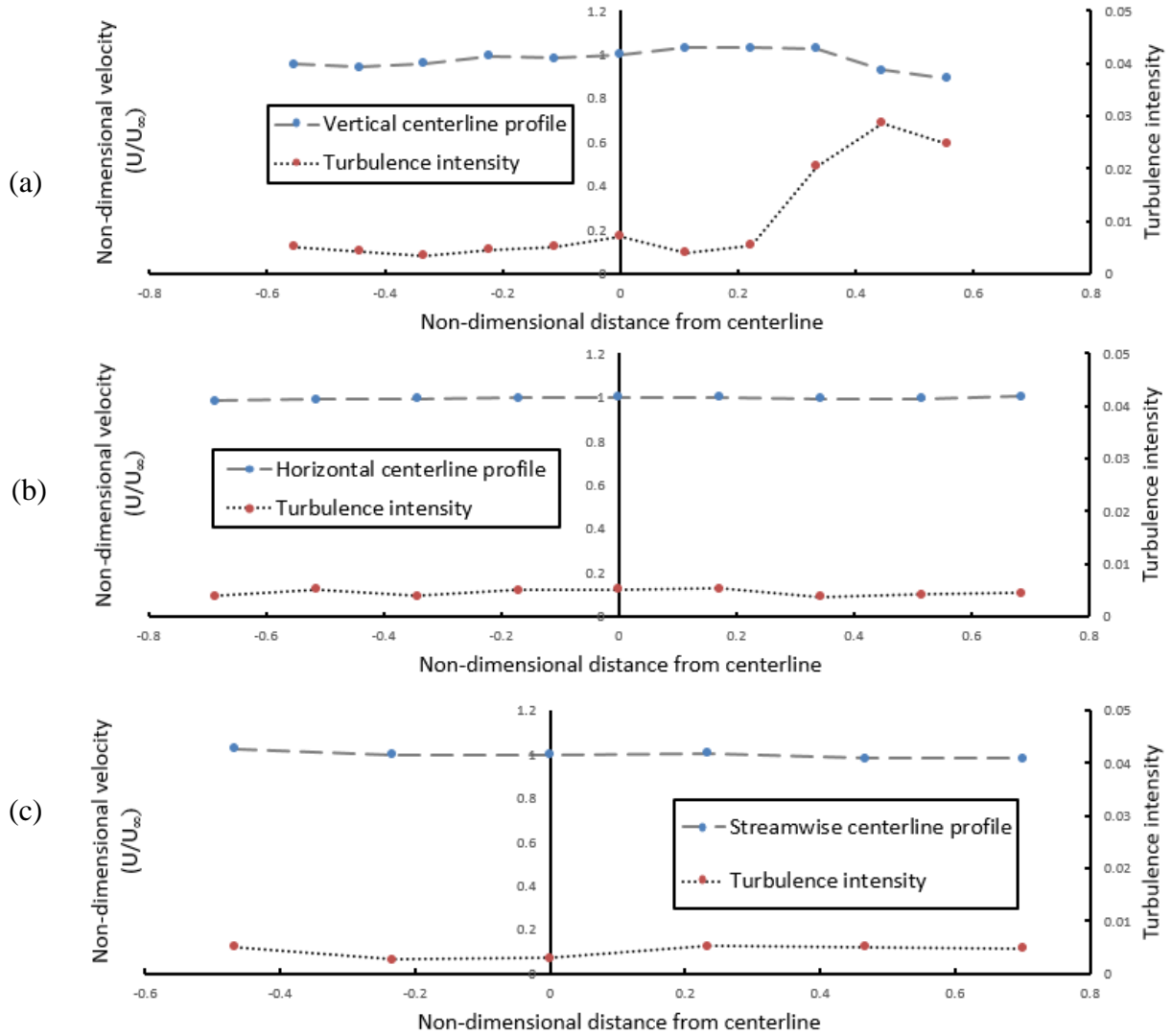
Figure A1 Wind tunnel profile along (a) the vertical centerline, (b) the horizontal (cross-stream) centerline, and (c) the axial (streamwise) centerline.

The characteristics of the Boundary Layer are presented in Table A-1.

Table A-1 Boundary layer characteristics

y	η	u/U∞
inches	[-]	[-]
0.16667	57.823	1
0.125	43.3672	0.99858
0.10417	36.1393	1.00125
0.08333	28.9115	0.99962
0.075	26.0203	0.99491
0.06667	23.1292	0.99998
0.05833	20.238	0.99547
0.05	17.3469	0.98688
0.04167	14.4557	0.9734
0.03333	11.5646	0.93203
0.025	8.67344	0.88575
0.01667	5.7823	0.82242
0.00833	2.89115	0.72613
0	0	0

Appendix B: Data

Appendix B contains all plots extracted from this study. Table B-1 presents a complete summary of the results of spectra analysis at the peak lift component frequency and twice the peak lift component frequency.

Table B-1 Spectral analysis of fluid force components at the main lift component frequency and twice the main lift component frequency

| | Frequency (Hz) | | Amplitude (m/s^2) | | | | Phase relative to Lift component | | | |
| | | | f_0 | | f_1 | | f_0 | | f_1 | |
G/D	f_0	f_1=2*f_0	Fluctuating lift	Fluctuating drag	Fluctuating lift	Fluctuating drag	Fluctuating drag	Velocity fluctuation	Fluctuating drag	Velocity fluctuation
1.64	16.4103	32.8206	0.7853	0.312	0.0043	0.0085	-87.04803113	35.82001281	4.860001738	143.6400514
1.5	16.1661	32.3322	0.5335	0.1902	0.0046	0.007	-104.0400372	-103.8600371	-37.44001339	-56.07002005
1	16.3614	32.7228	0.4001	0.1488	0.0057	0.0111	-88.83003176	-127.4400456	-19.44000695	20.16000721
0.75	16.0195	32.039	0.7038	0.1219	0.0055	0.0071	-141.1920505	-151.5600542	158.4000566	168.3000602
0.5	15.7753	31.5506	1.051	0.1028	0.006	0.0106	-121.5000434	127.0800454	144.7200517	-43.9200157
0.4	15.4823	30.9646	0.6467	0.2486	0.0108	0.0084	-147.5280528	-51.12001828	129.2400462	-110.8620396
0.3	14.5543	29.1086	0.1868	0.0471	0.0041	0.0044	94.50003379	-7.614002722	120.6000431	10.80000386
0.2	9.7192	19.4384	0.0705	0.0469	0.0225	0.0066	174.2400623	-78.300028	-69.48002484	111.6000399
0.1	10.696	21.392	0.0437	0.0064	0.0263	0.0064	69.30002478	-44.01001574	7.380002639	-5.400001931

Table B-2 shows the Figure name depending on G/D and type of figure.

Table B-2 Figure name relative to content

| | Amplitude (m/s^2) | | | Phase relative to Lift component | |
| | Velocity fluctuation | Fluctuating drag acceleration | Fluctuating drag acceleration | Velocity Fluctuation | Fluctuating drag acceleration |
G/D				Figure	
1.64	B1	B2	B3	B4	B5
1.5	B6	B7	B8	B9	B10
1	B11	B12	B13	B14	B15
0.75	B16	B17	B18	B19	B20
0.5	B21	B22	B23	B24	B25
0.4	B26	B27	B28	B29	B30
0.3	B31	B32	B33	B34	B35
0.2	B36	B37	B38	B39	B40
0.1	B41	B42	B43	B44	B45

Figures B1 through B45 show the spectral analysis results for different gap ratios. A table of contents is included on the following page for easier reference.

Spectral Analysis Results for Different Gap Ratios:

G/D = 1.64
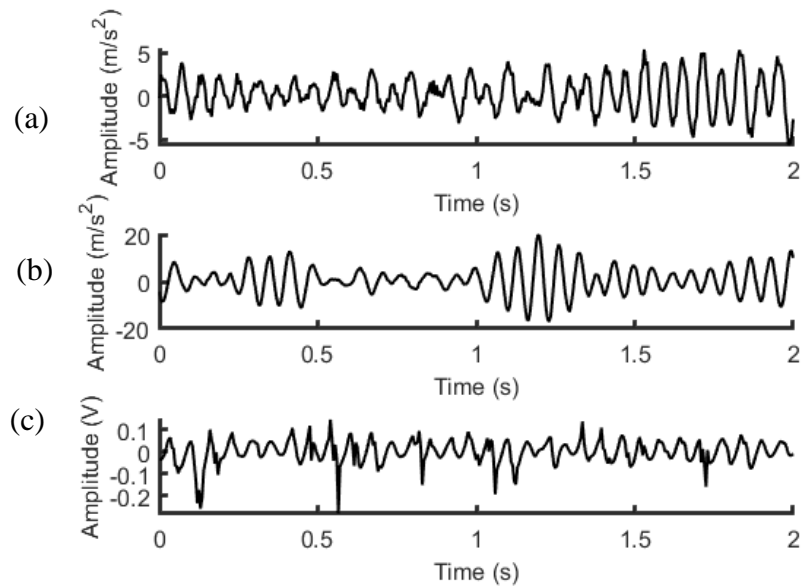
Figure B1 Time histories with *G/D* = 1.64 of (a) cylinder vibration in the streamwise direction, (b) cylinder vibration in the cross-stream direction, and (c) velocity fluctuations in the wake at $x_v/D = 2.5$, $y_v/D = 1.0$
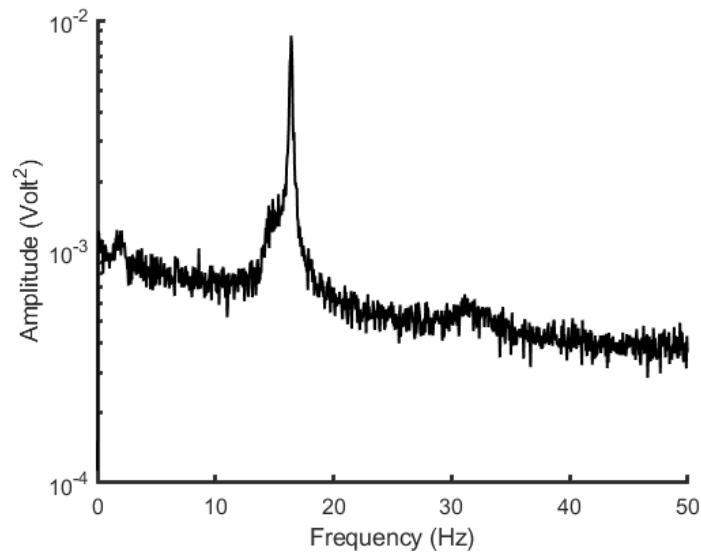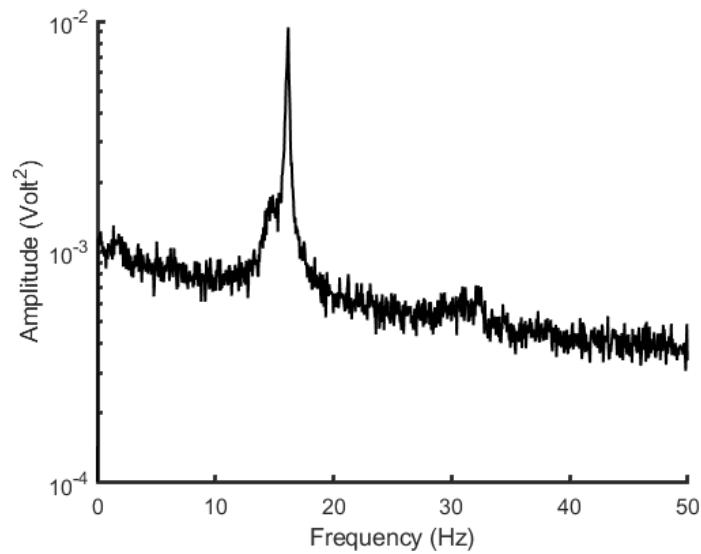
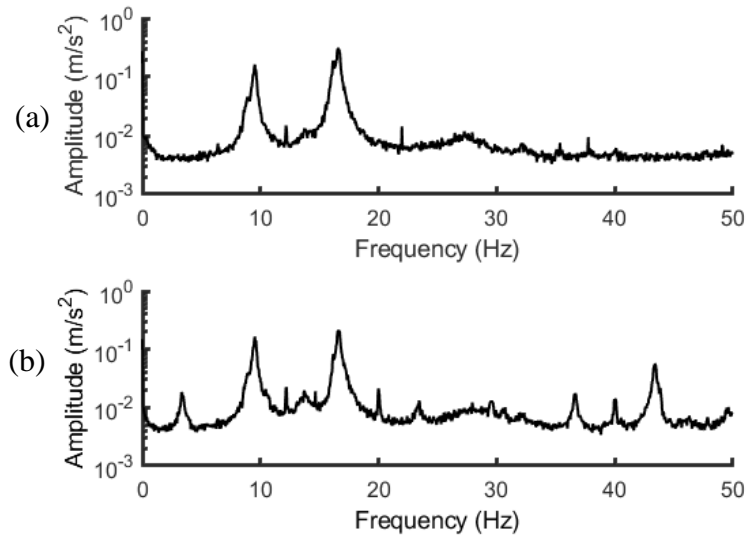Figure B2 Amplitude spectra of velocity fluctuations at *G/D* = 1.64
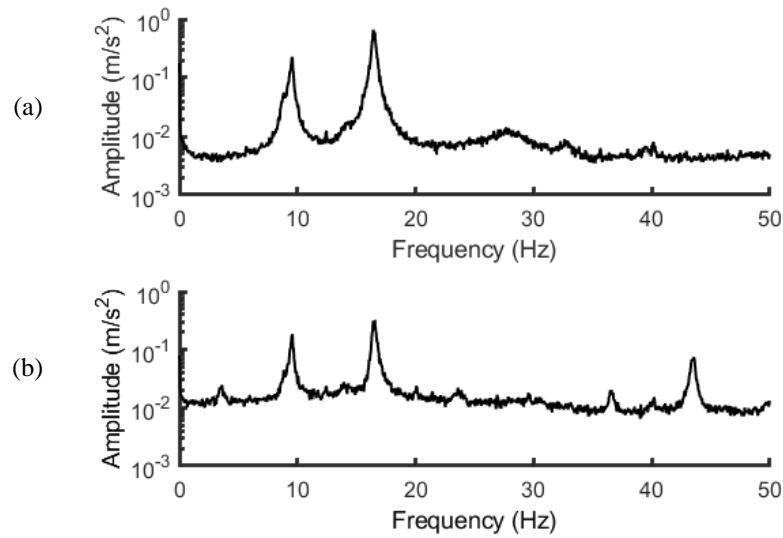
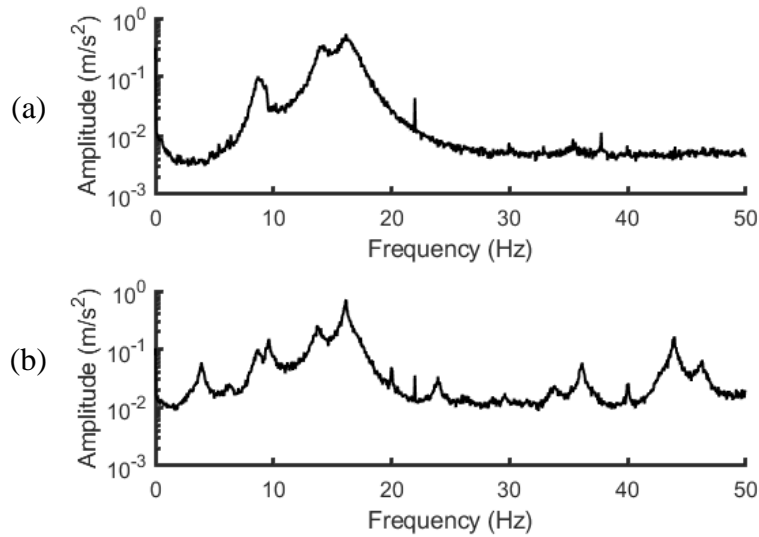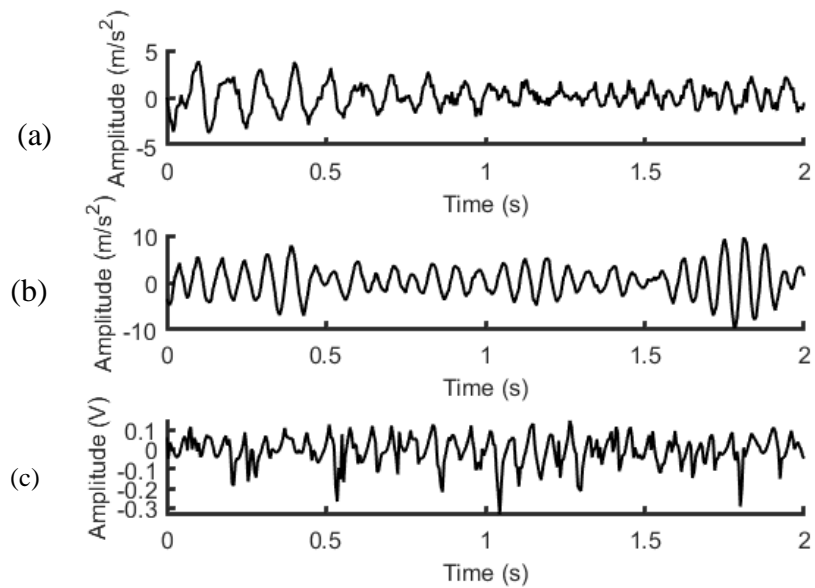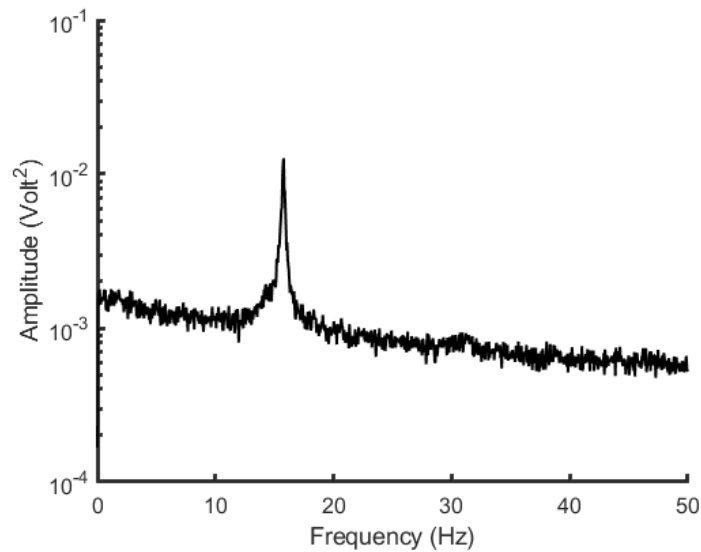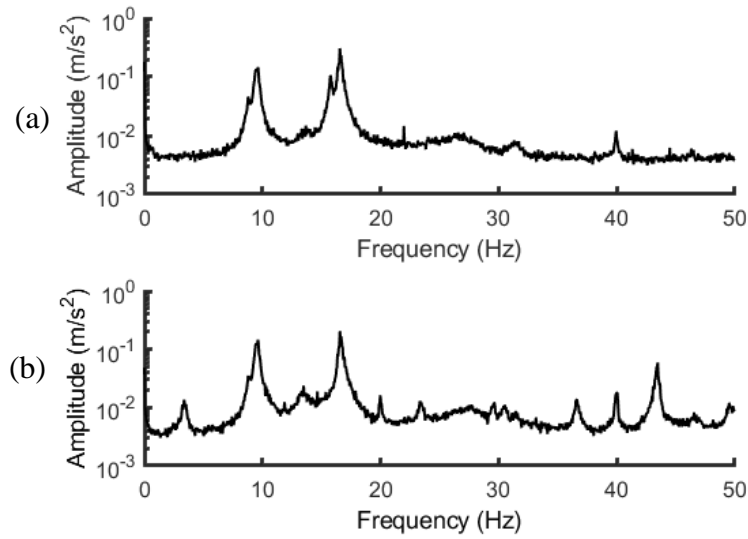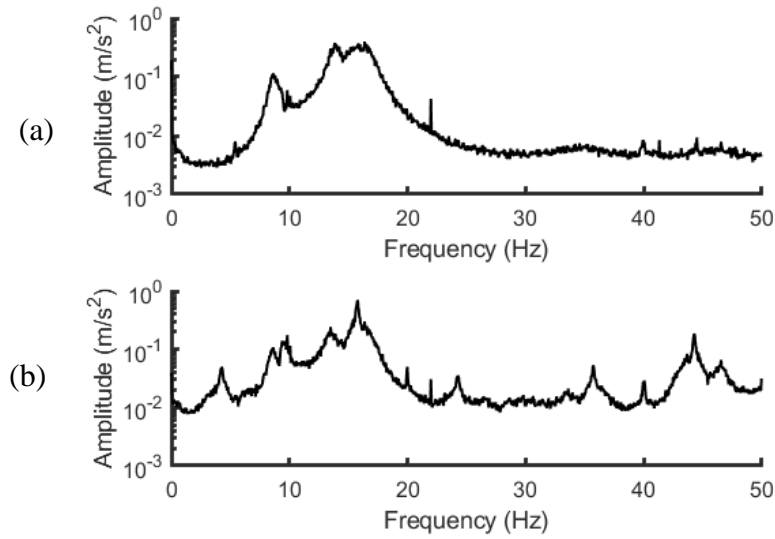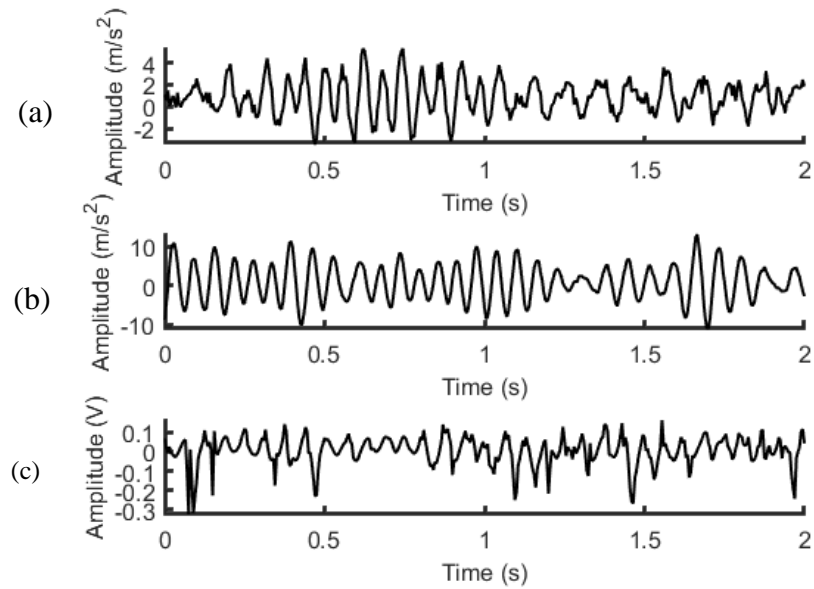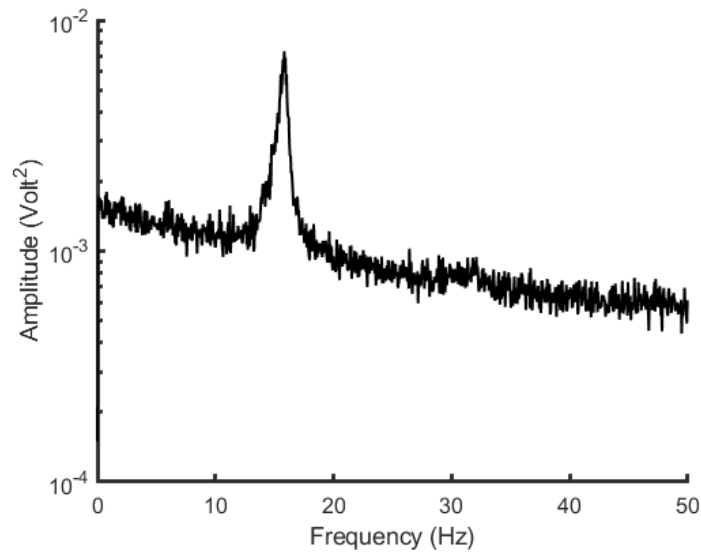Figure B3 Amplitude spectra of fluctuating drag acceleration at *G/D* = 1.64 (a) top accelerometer, (b) bottom accelerometer
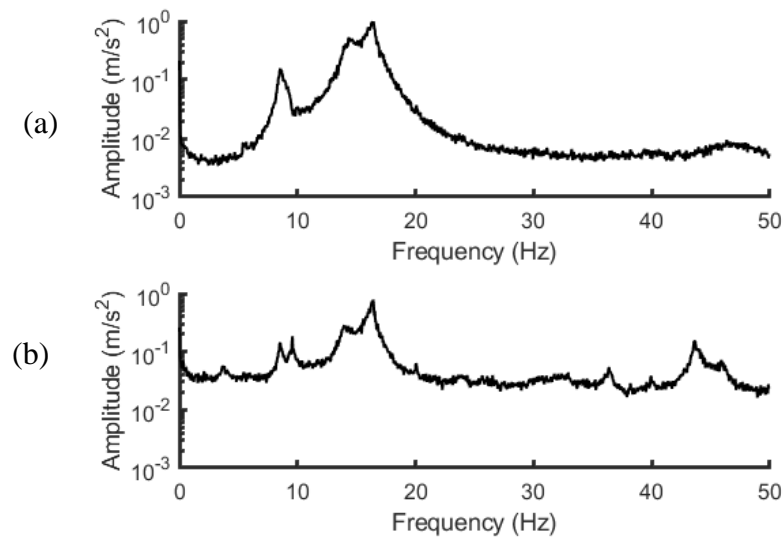
Figure B4 Amplitude spectra of fluctuating lift acceleration at *G/D* = 1.64 (a) top accelerometer, (b) bottom accelerometer
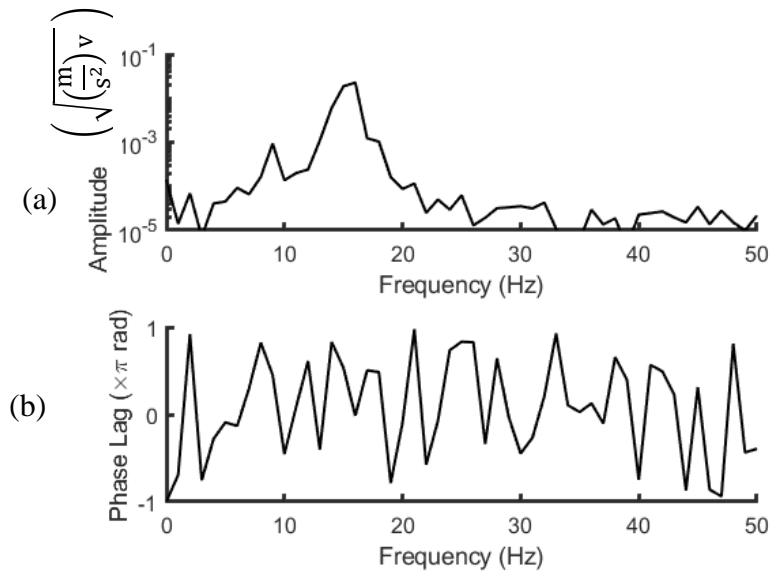
Figure B5 Cross-spectra (a) amplitude and (phase) of velocity fluctuation relative to the fluctuating lift acceleration at *G/D* = 1.64
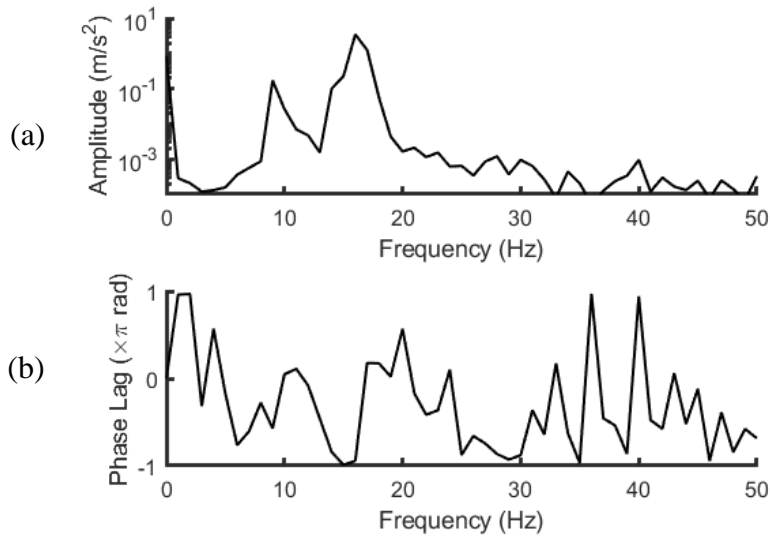
Figure B6 Cross-spectra (a) amplitude and (phase) of fluctuating drag acceleration relative to the fluctuating lift acceleration at *G/D* = 1.64

G/D = 1.5
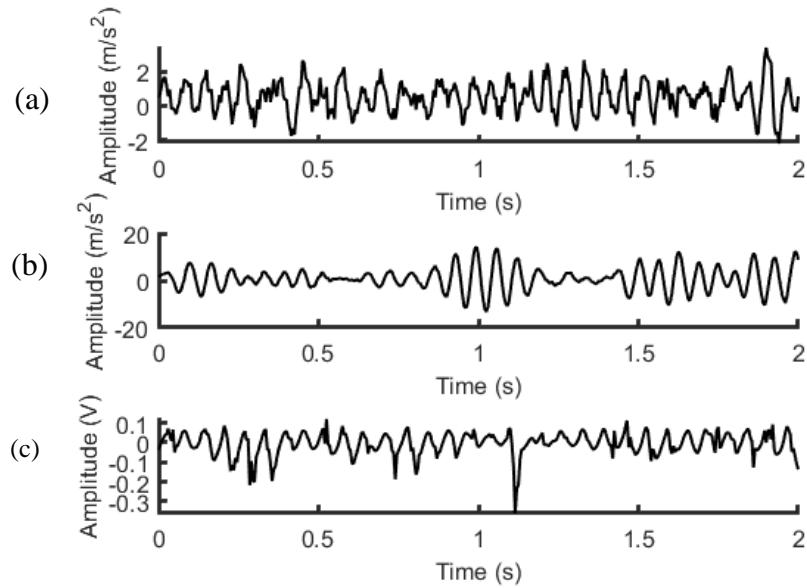
Figure B7 Time histories with *G/D* = 1.5 of (a) cylinder vibration in the streamwise direction, (b) cylinder vibration in the cross-stream direction, and (c) velocity fluctuations in the wake at $x_v/D = 2.5$, $y_v/D = 1.0$

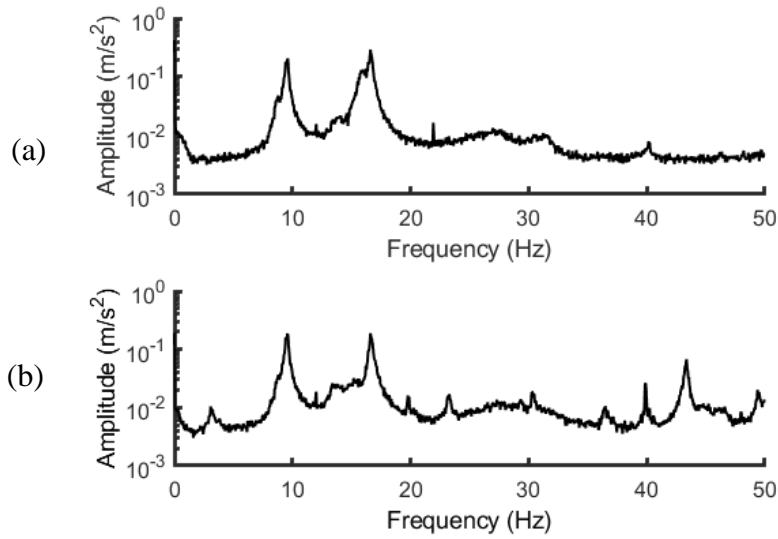Figure B8 Amplitude spectra of velocity fluctuations at *G/D* = 1.5

93

Figure B9 Amplitude spectra of fluctuating drag acceleration at *G/D* = 1.5 (a) top accelerometer, (b) bottom accelerometer
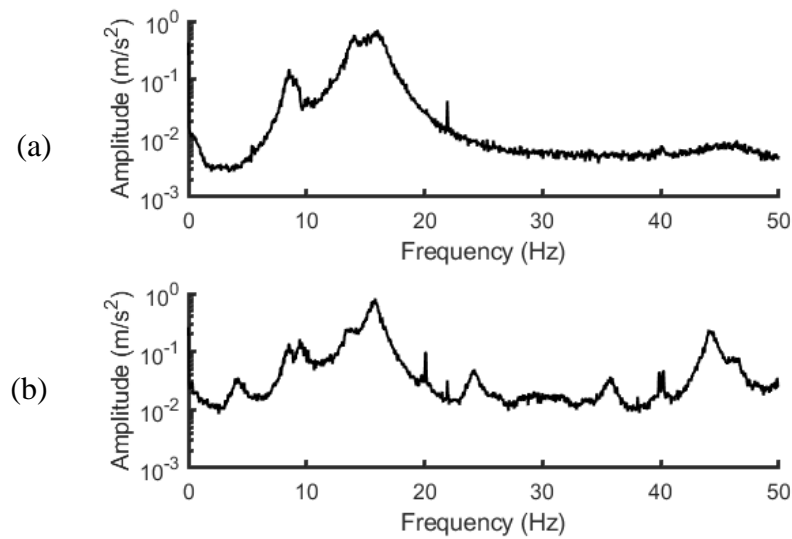

Figure B10 Amplitude spectra of fluctuating lift acceleration at *G/D* = 1.5 (a) top accelerometer, (b) bottom accelerometer
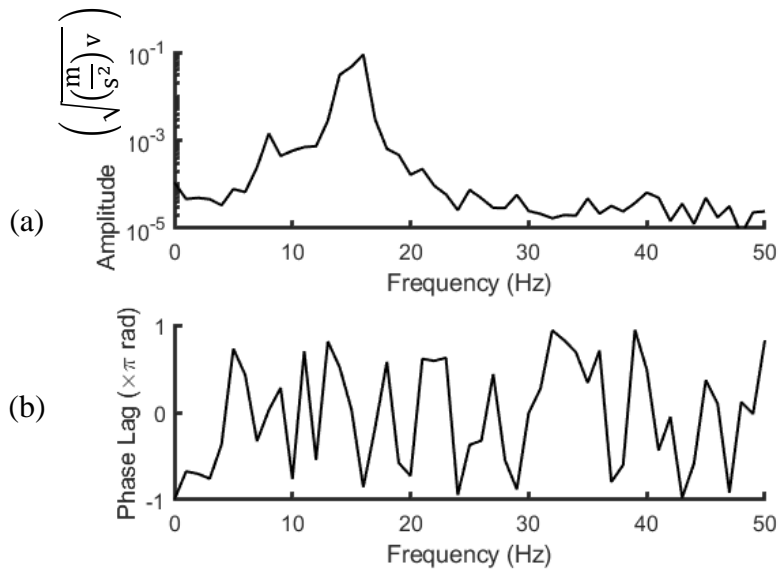
(a)

(b)
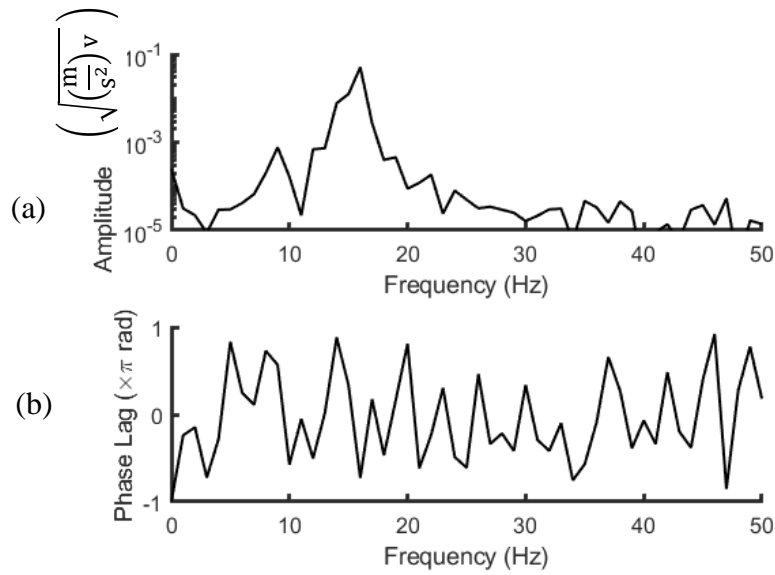
Figure B11 Cross-spectra (a) amplitude and (phase) of velocity fluctuation relative to the fluctuating lift acceleration at *G/D* = 1.5
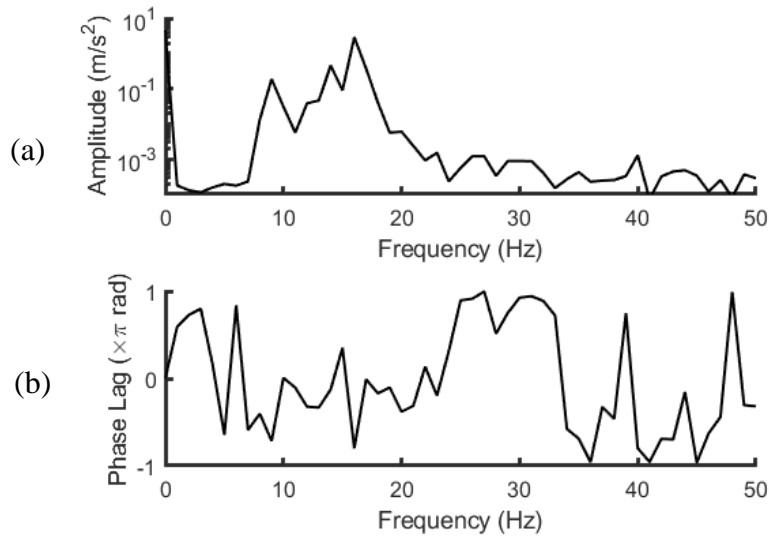
(a)

(b)
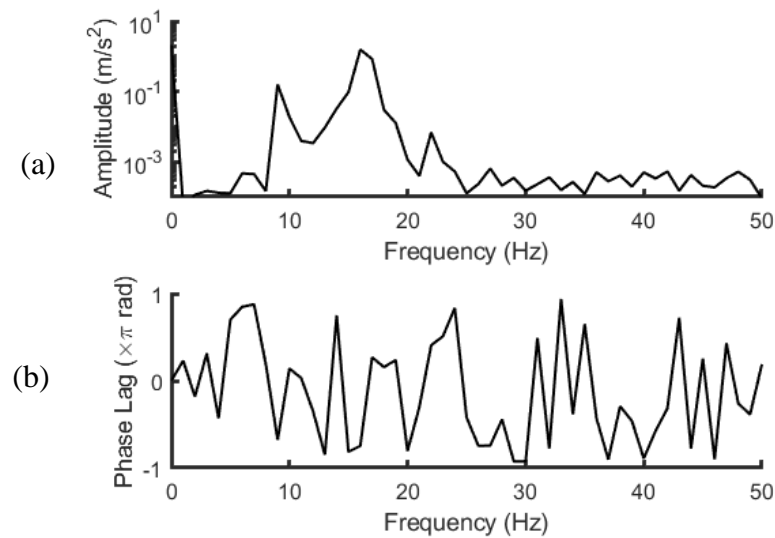
Figure B12 Cross-spectra (a) amplitude and (phase) of fluctuating drag acceleration relative to the fluctuating lift acceleration at *G/D* = 1.5
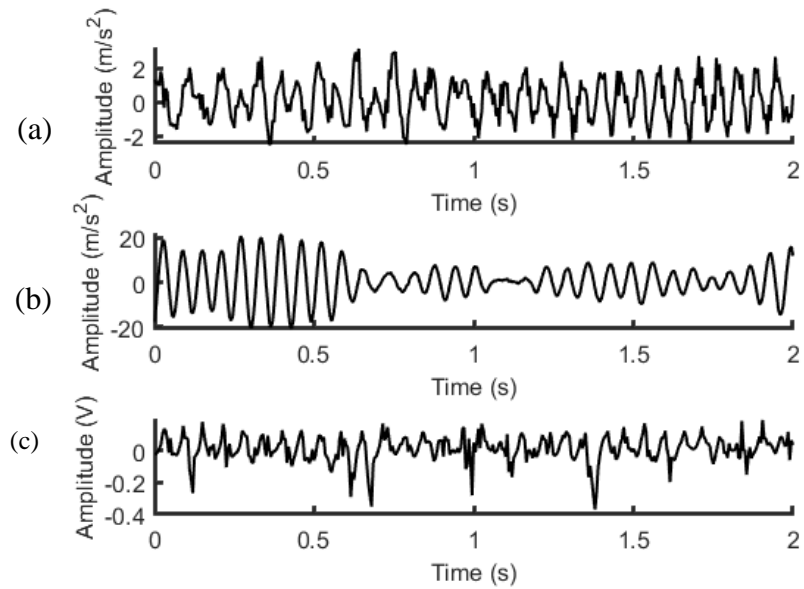
G/D = 1

Figure B11 Time histories with *G/D* = 1.0 of (a) cylinder vibration in the streamwise direction, (b) cylinder vibration in the cross-stream direction, and (c) velocity fluctuations in the wake at x_v/D = 2.5, y_v/D = 1.0
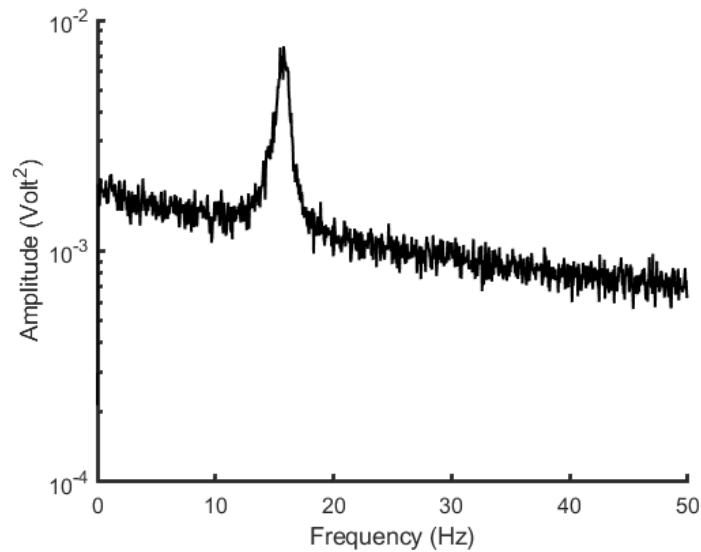

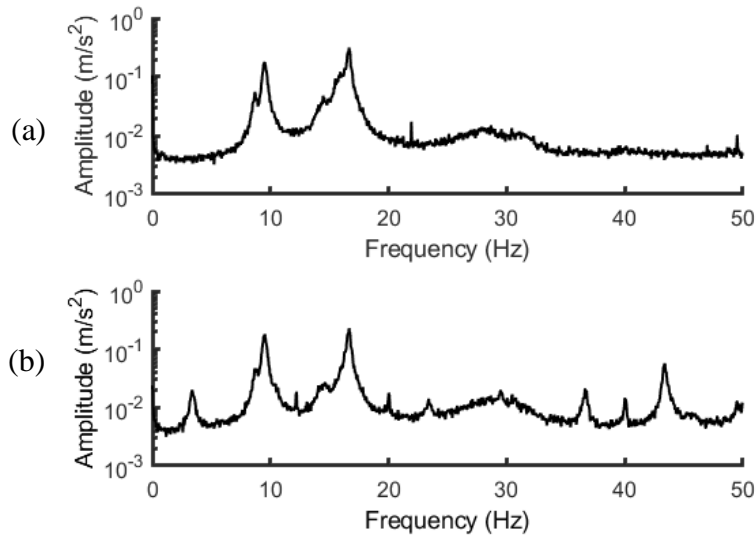Figure B14 Amplitude spectra of velocity fluctuations at *G/D* = 1

Figure B15 Amplitude spectra of fluctuating drag acceleration at *G/D* = 1 (a) top accelerometer, (b) bottom accelerometer
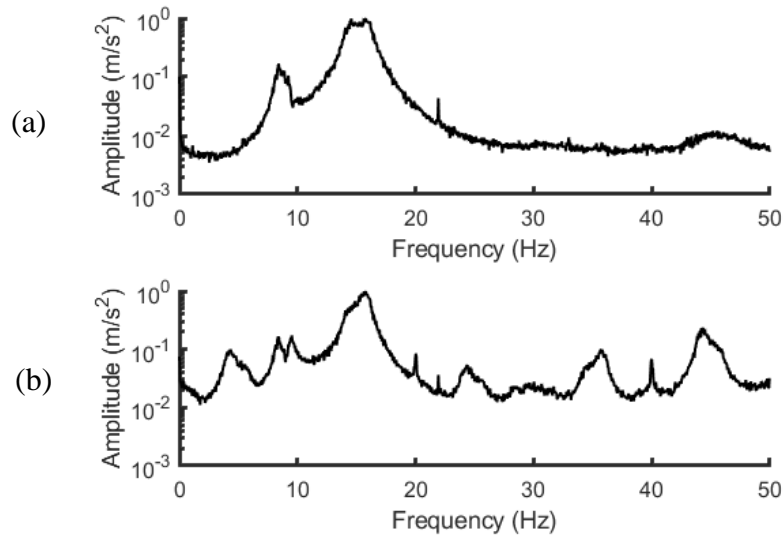

Figure B16 Amplitude spectra of fluctuating lift acceleration at *G/D* = 1 (a) top accelerometer, (b) bottom accelerometer
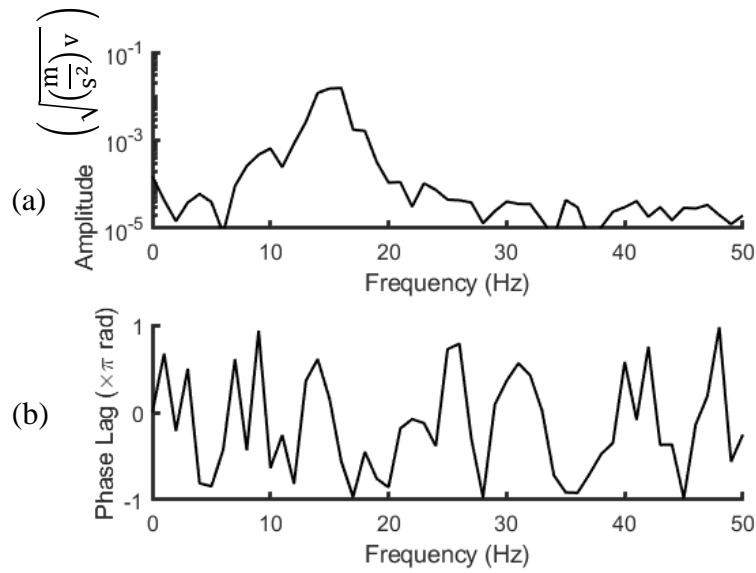
Figure B17 Cross-spectra (a) amplitude and (phase) of velocity fluctuation relative to the fluctuating lift acceleration at $G/D = 1$
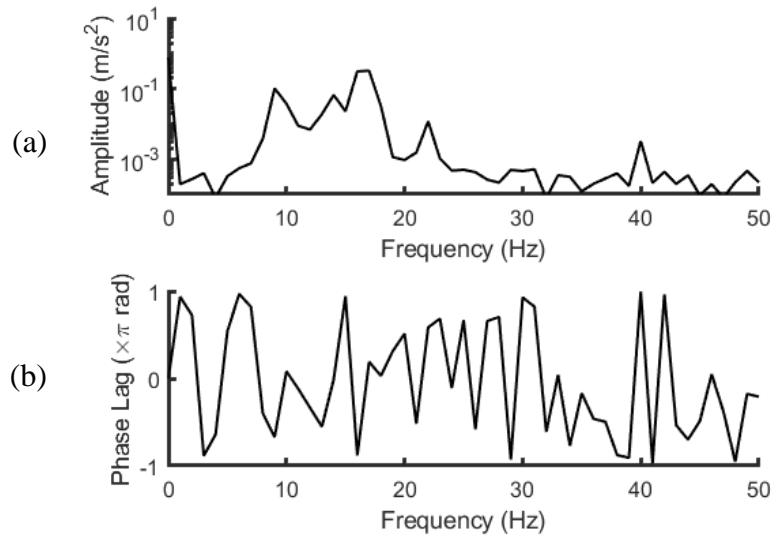
Figure B18 Cross-spectra (a) amplitude and (phase) of fluctuating drag acceleration relative to the fluctuating lift acceleration at $G/D = 1$

G/D = 0.75

Figure B19 Time histories with *G/D* = 0.75 of (a) cylinder vibration in the streamwise direction, (b) cylinder vibration in the cross-stream direction, and (c) velocity fluctuations in the wake at $x_v/D = 2.5$, $y_v/D = 1.0$

Figure B20 Amplitude spectra of velocity fluctuations at *G/D* = 0.75

Figure B21 Amplitude spectra of fluctuating drag acceleration at *G/D* = 0.75 (a) top accelerometer, (b) bottom accelerometer

Figure B22 Amplitude spectra of fluctuating lift acceleration at *G/D* = 0.75 (a) top accelerometer, (b) bottom accelerometer
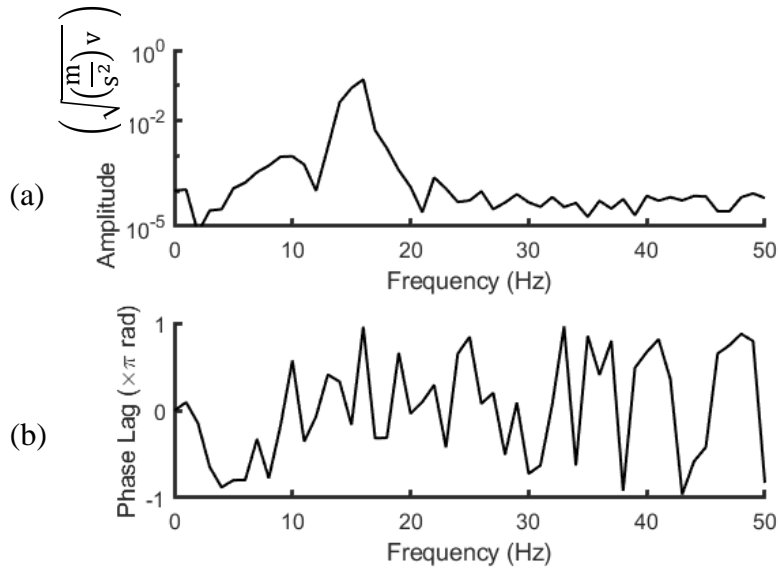
Figure B23 Cross-spectra (a) amplitude and (phase) of velocity fluctuation relative to the fluctuating lift acceleration at $G/D = 0.75$
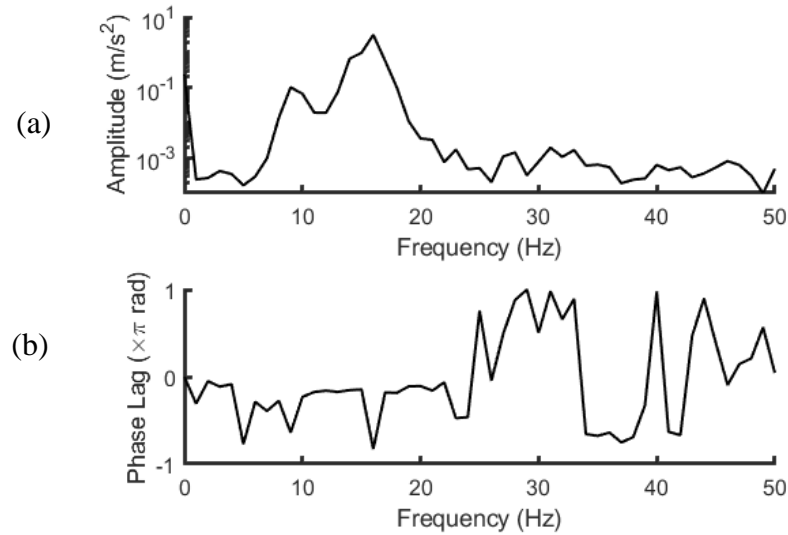

Figure B24 Cross-spectra (a) amplitude and (phase) of fluctuating drag acceleration relative to the fluctuating lift acceleration at $G/D = 0.75$
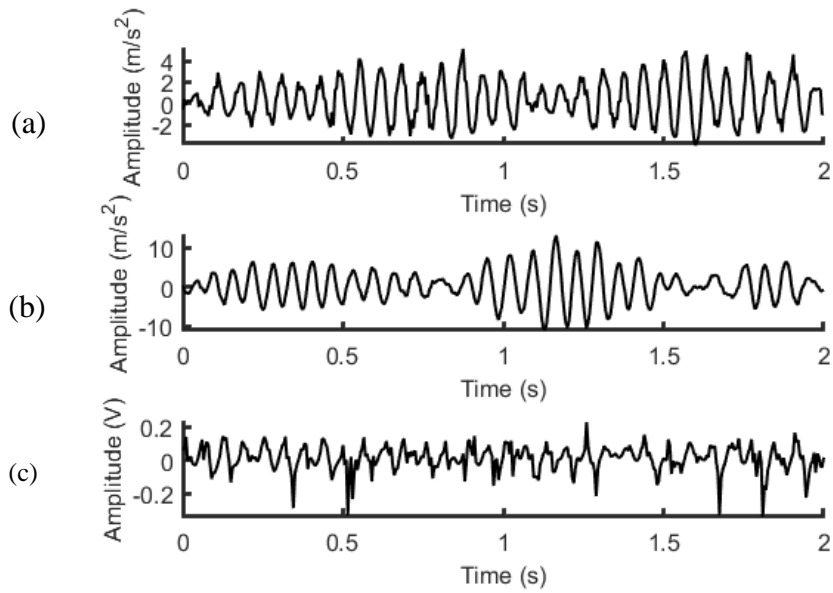
G/D = 0.5

Figure B25 Time histories with *G/D* = 0.5 of (a) cylinder vibration in the streamwise direction, (b) cylinder vibration in the cross-stream direction, and (c) velocity fluctuations in the wake at $x_v/D = 2.5$, $y_v/D = 1.0$
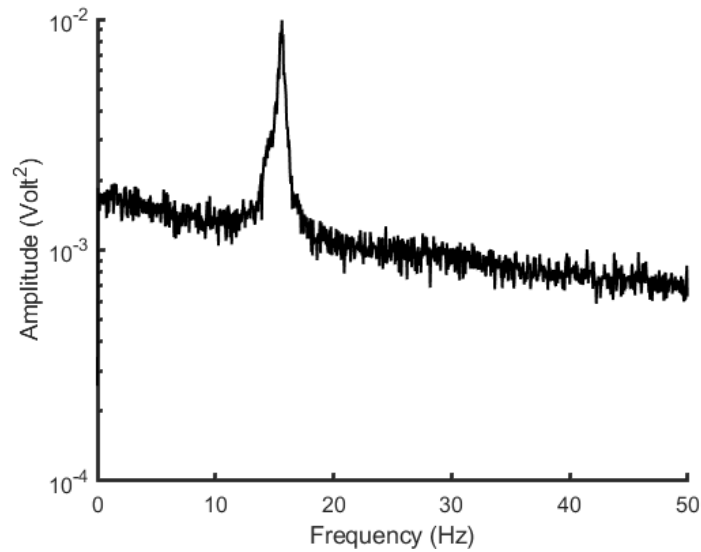

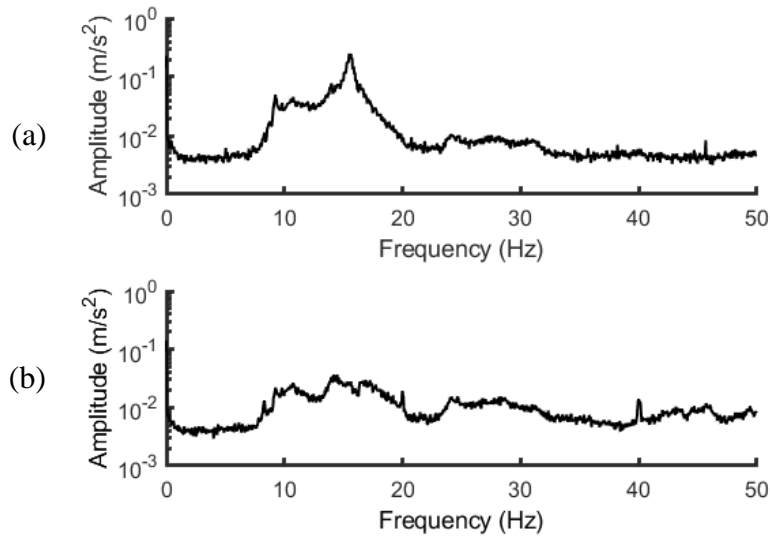Figure 27 Amplitude spectra of velocity fluctuations at *G/D* = 0.5

Figure B27 Amplitude spectra of fluctuating drag acceleration at *G/D* = 0.5 (a) top accelerometer, (b) bottom accelerometer
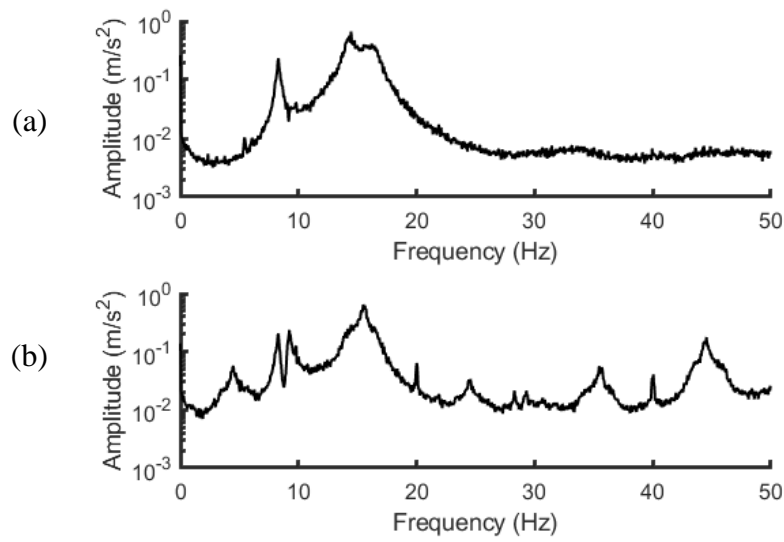

Figure B28 Amplitude spectra of fluctuating lift acceleration at *G/D* = 0.5 (a) top accelerometer, (b) bottom accelerometer
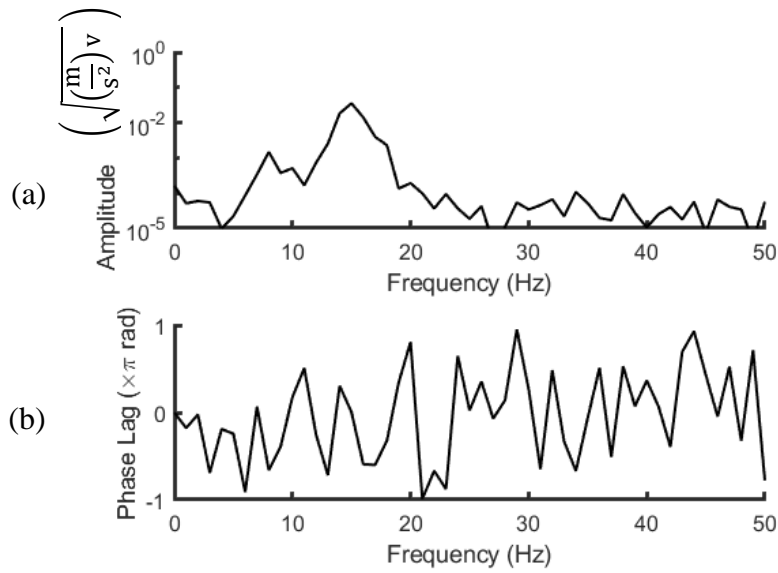
Figure B29 Cross-spectra (a) amplitude and (phase) of velocity fluctuation relative to the fluctuating lift acceleration at $G/D = 0.5$
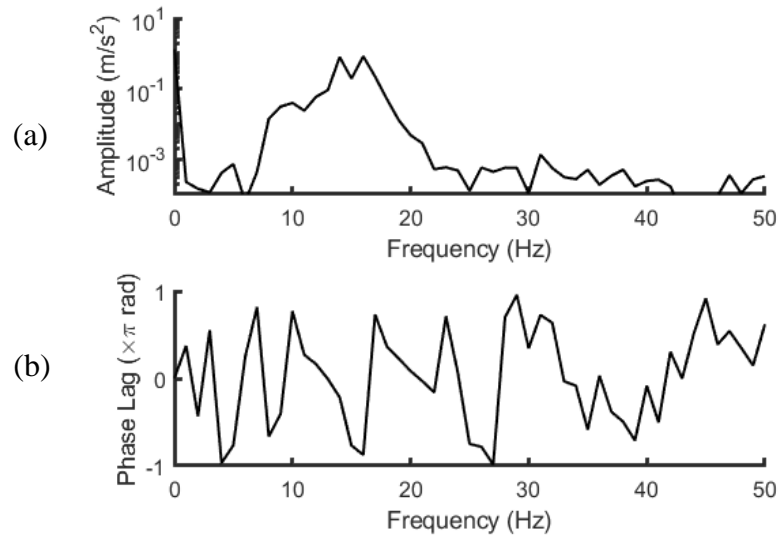

Figure B30 Cross-spectra (a) amplitude and (phase) of fluctuating drag acceleration relative to the fluctuating lift acceleration at $G/D = 0.5$

G/D = 0.4

Figure B31 Time histories with *G/D* = 0.4 of (a) cylinder vibration in the streamwise direction, (b) cylinder vibration in the cross-stream direction, and (c) velocity fluctuations in the wake at $x_v/D = 2.5$, $y_v/D = 1.0$

Figure B32 Amplitude spectra of velocity fluctuations at *G/D* = 0.4

Figure B33 Amplitude spectra of fluctuating drag acceleration at *G/D* = 0.4 (a) top accelerometer, (b) bottom accelerometer

Figure B34 Amplitude spectra of fluctuating lift acceleration at *G/D* = 0.4 (a) top accelerometer, (b) bottom accelerometer

Figure B35 Cross-spectra (a) amplitude and (phase) of velocity fluctuation relative to the fluctuating lift acceleration at $G/D = 0.4$

Figure B36 Cross-spectra (a) amplitude and (phase) of fluctuating drag acceleration relative to the fluctuating lift acceleration at $G/D = 0.4$
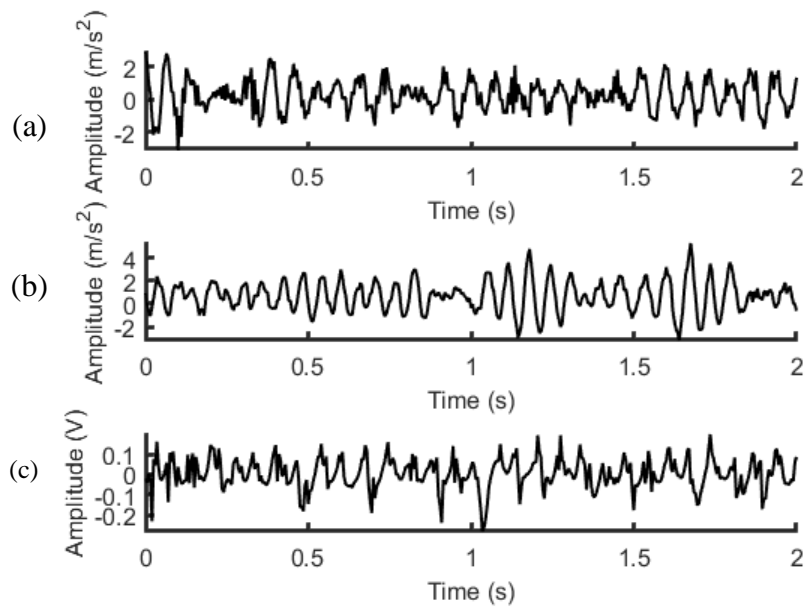
G/D = 0.3

Figure B37 Time histories with $G/D = 0.3$ of (a) cylinder vibration in the streamwise direction, (b) cylinder vibration in the cross-stream direction, and (c) velocity fluctuations in the wake at $x_v/D = 2.5$, $y_v/D = 1.0$
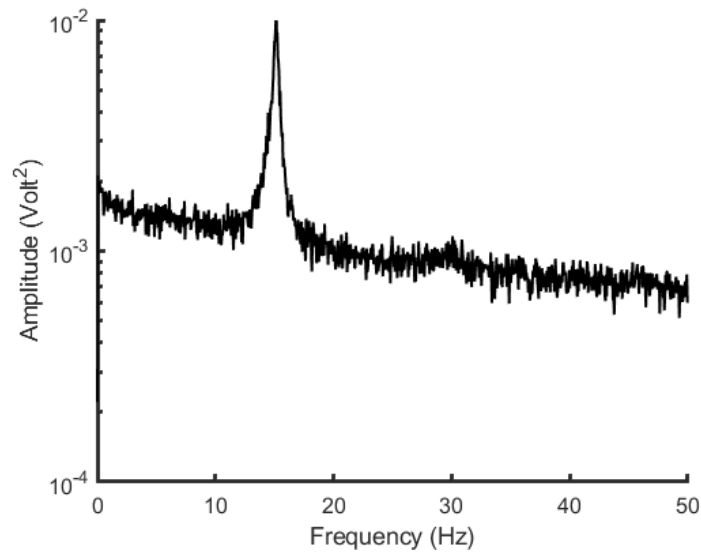

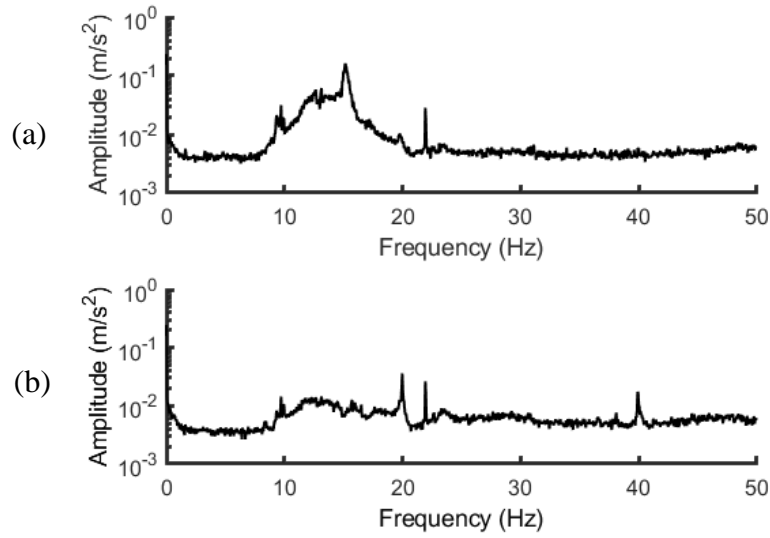Figure B38 Amplitude spectra of velocity fluctuations at $G/D = 0.3$

Figure B39 Amplitude spectra of fluctuating drag acceleration at *G/D* = 0.3 (a) top accelerometer, (b) bottom accelerometer
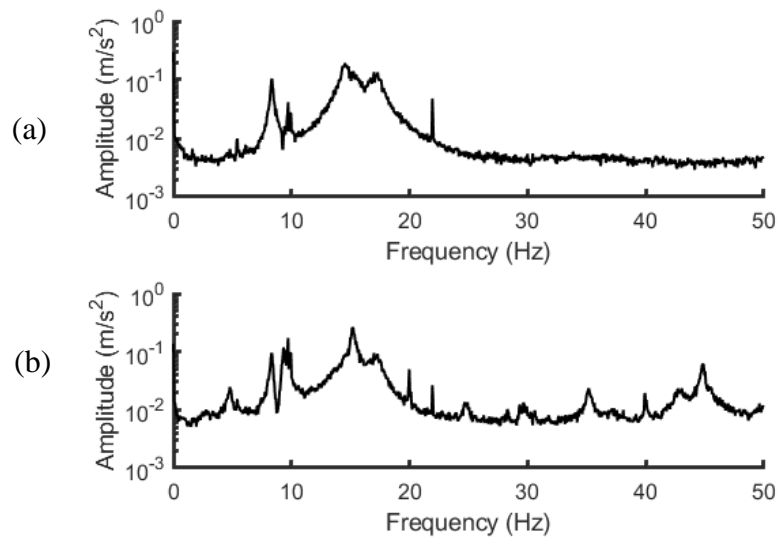

Figure B40 Amplitude spectra of fluctuating lift acceleration at *G/D* = 0.3 (a) top accelerometer, (b) bottom accelerometer
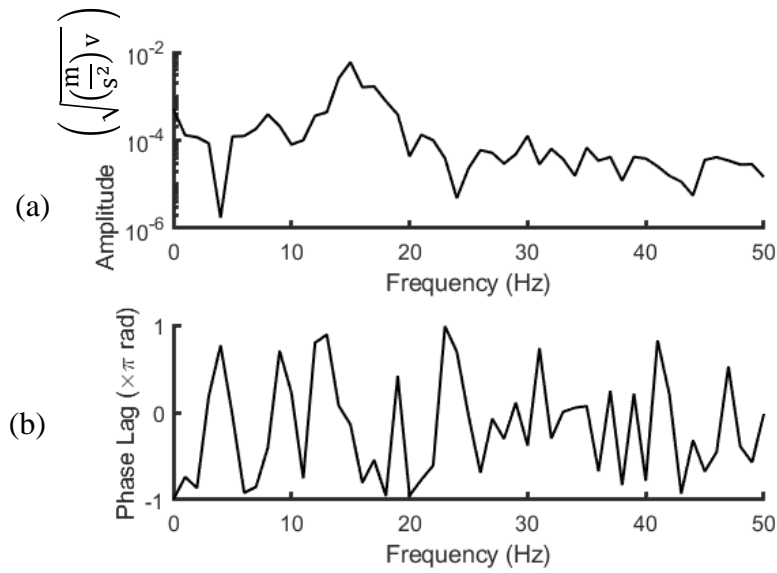
Figure B41 Cross-spectra (a) amplitude and (phase) of velocity fluctuation relative to the fluctuating lift acceleration at $G/D = 0.3$
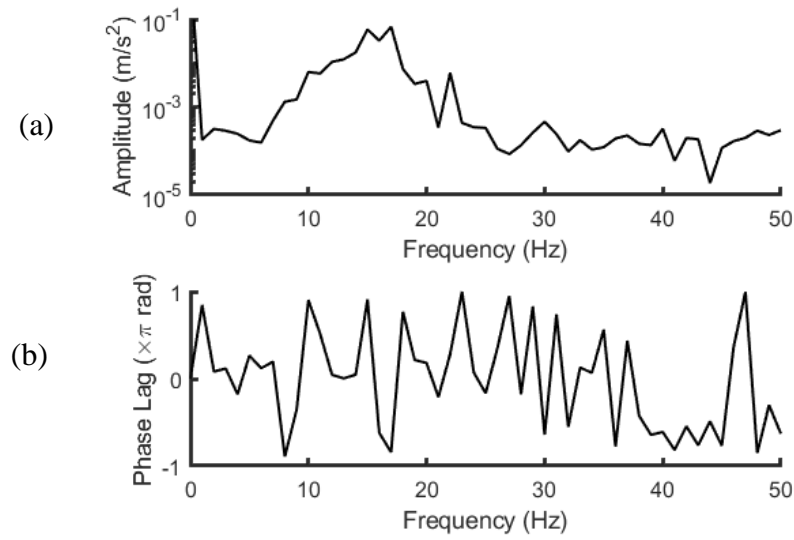

Figure B42 Cross-spectra (a) amplitude and (phase) of fluctuating drag acceleration relative to the fluctuating lift acceleration at $G/D = 0.3$
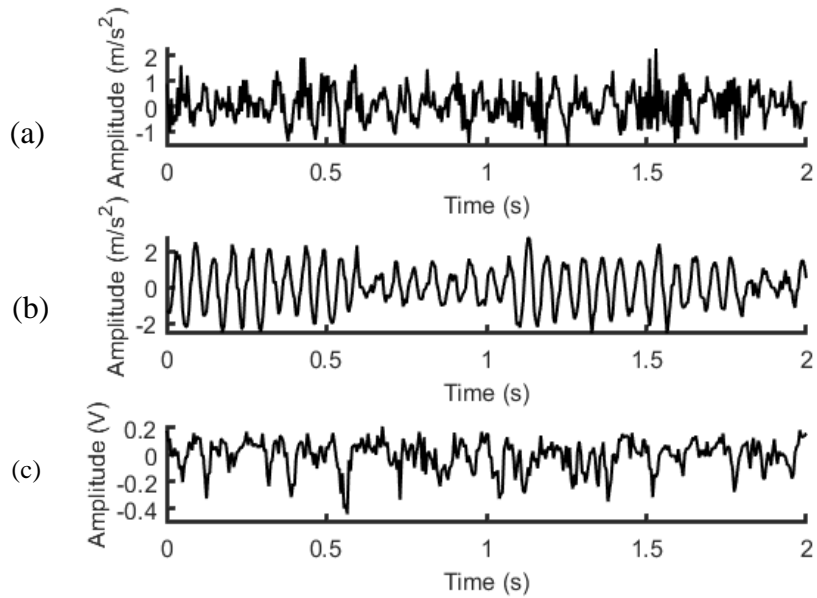
G/D = 0.2

(a)

(b)

(c)

Figure B43 Time histories with *G/D* = 0.2 of (a) cylinder vibration in the streamwise direction, (b) cylinder vibration in the cross-stream direction, and (c) velocity fluctuations in the wake at $x_v/D = 2.5$, $y_v/D = 1.0$
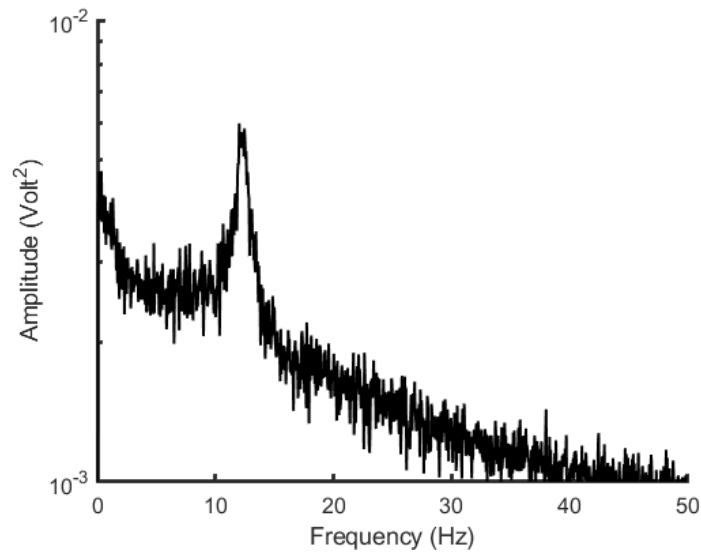

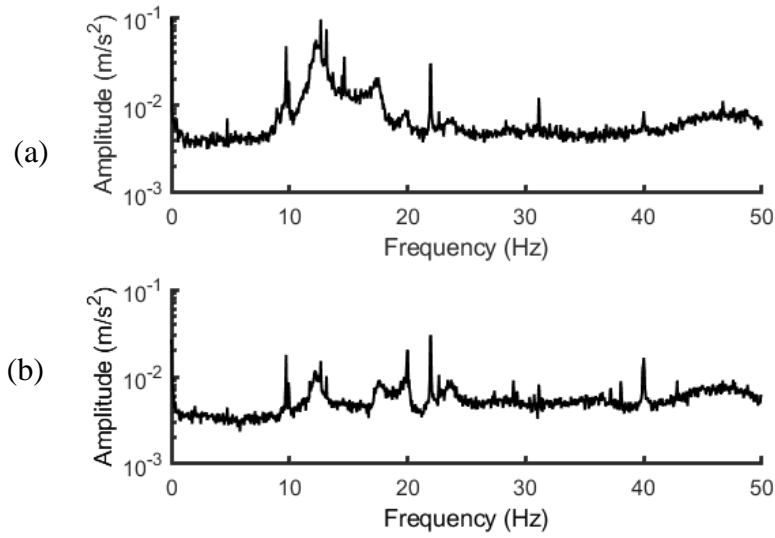Figure B44 Amplitude spectra of velocity fluctuations at *G/D* = 0.2

111

Figure B45 Amplitude spectra of fluctuating drag acceleration at *G/D* = 0.2 (a) top
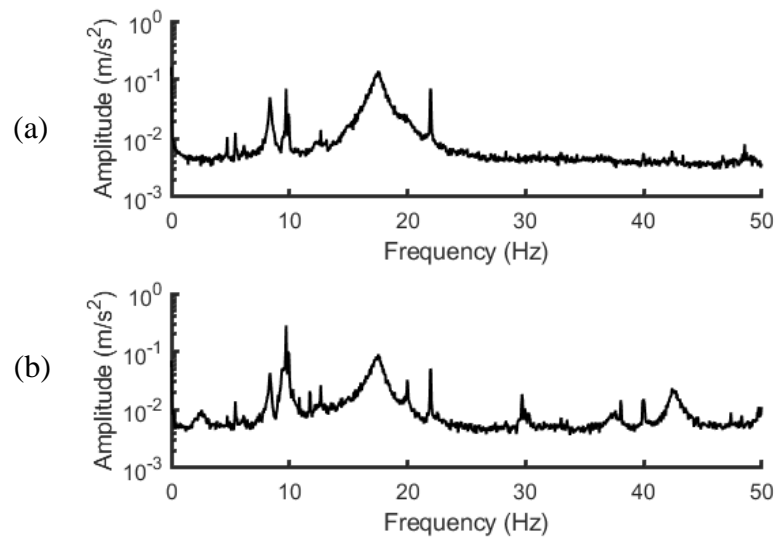accelerometer, (b) bottom accelerometer

Figure B46 Amplitude spectra of fluctuating lift acceleration at *G/D* = 0.2 (a) top
accelerometer, (b) bottom accelerometer

Figure B47 Cross-spectra (a) amplitude and (phase) of velocity fluctuation relative to the fluctuating lift acceleration at $G/D = 0.2$

Figure B48 Cross-spectra (a) amplitude and (phase) of fluctuating drag acceleration relative to the fluctuating lift acceleration at $G/D = 0.2$

G/D = 0.1
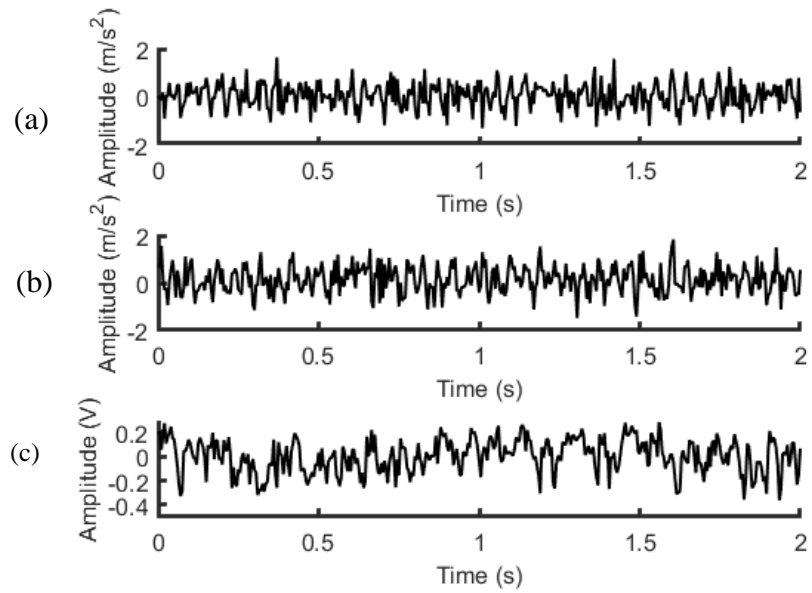
Figure B49 Time histories with *G/D* = 0.1 of (a) cylinder vibration in the streamwise direction, (b) cylinder vibration in the cross-stream direction, and (c) velocity fluctuations in the wake at $x_v/D = 2.5$, $y_v/D = 1.0$
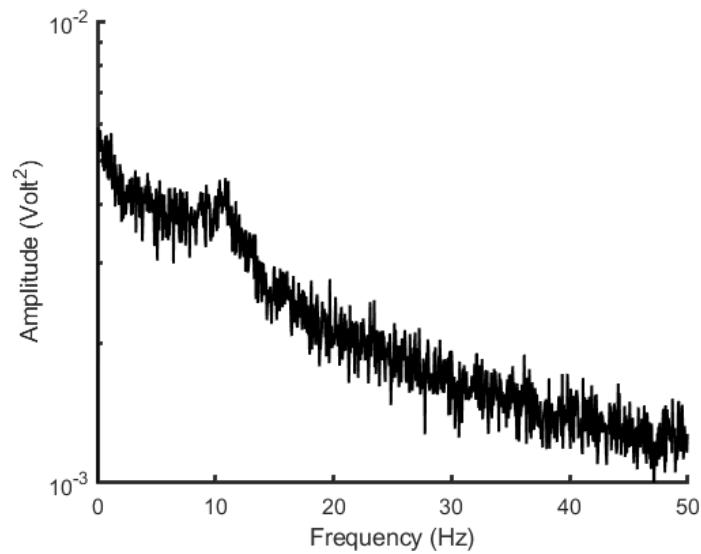
Figure B50 Amplitude spectra of velocity fluctuations at *G/D* = 0.1
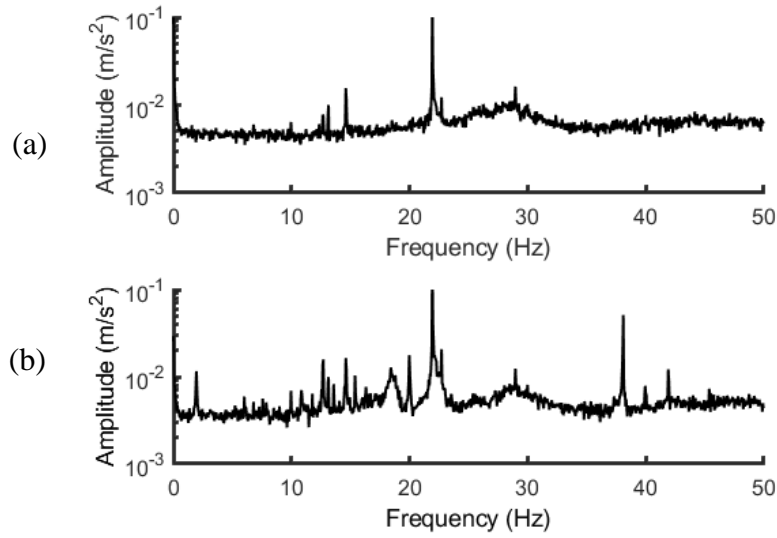
Figure B51 Amplitude spectra of fluctuating drag acceleration at *G/D* = 0.1 (a) top accelerometer, (b) bottom accelerometer

Figure B52 Amplitude spectra of fluctuating lift acceleration at *G/D* = 0.1 (a) top accelerometer, (b) bottom accelerometer
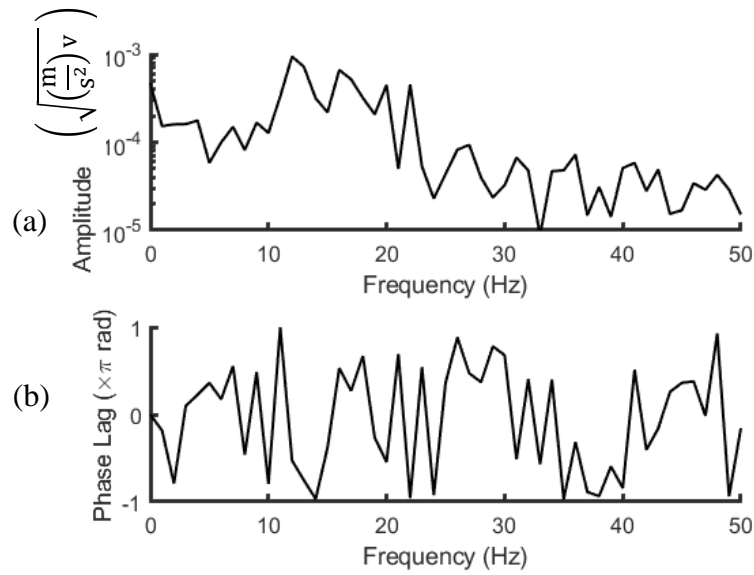
Figure B53 Cross-spectra (a) amplitude and (phase) of velocity fluctuation relative to the fluctuating lift acceleration at *G/D* = 0.1
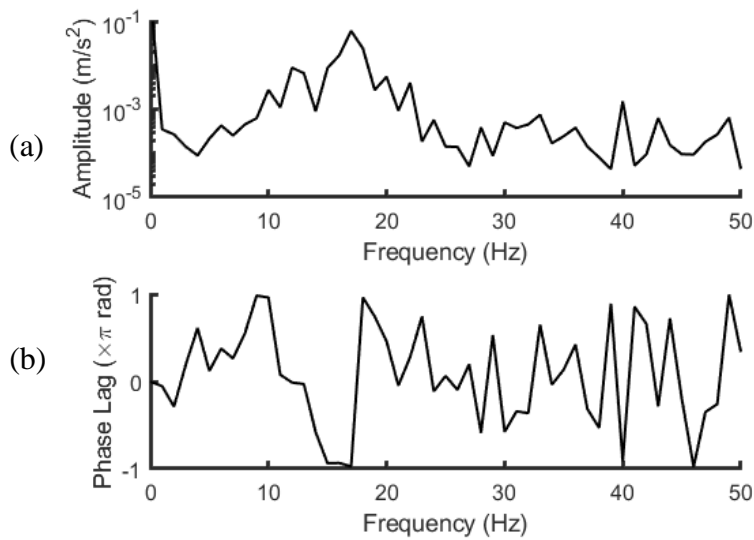

Figure B54 Cross-spectra (a) amplitude and (phase) of fluctuating drag acceleration relative to the fluctuating lift acceleration at *G/D* = 0.1

Appendix C: MATLAB Code for Data Reduction

Appendix C contains the MATLAB code used to analyze the data extracted from LabView, all the data was compiled into one file named "records", composed by 30 data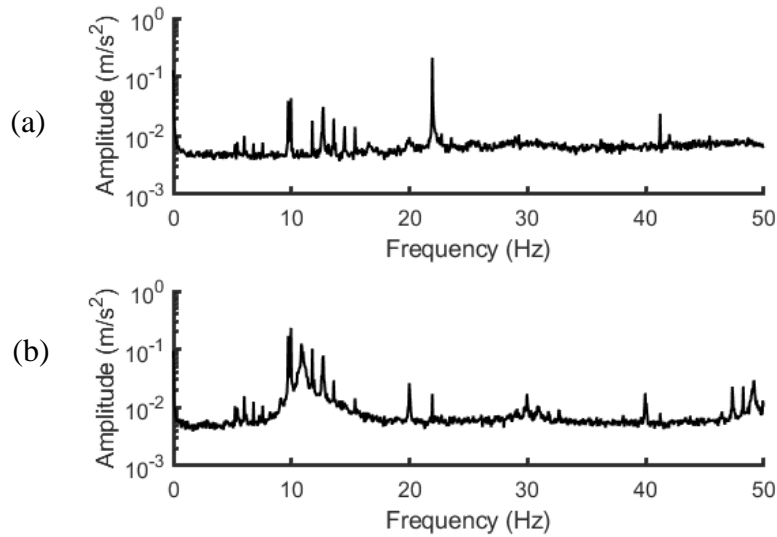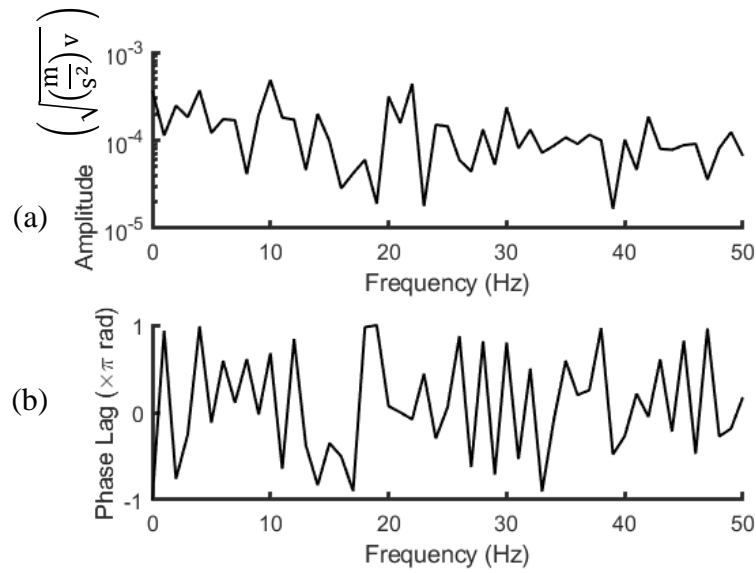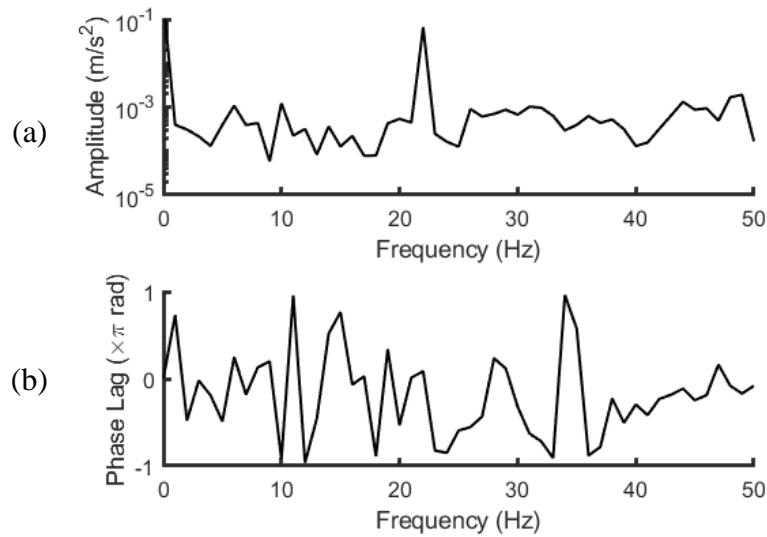 samples which with 4096 data points for time, velocity fluctuation (in Volts), and fluctuating drag and lift accelerations for the top and bottom accelerometers (in m/s^2). The code was written by the author as a MATLAB R2018a script.

```
close all
%Data analysis
%%
%Variables:
%time stamp
%4096 data points per record, 30 records per sensor at each location
t=records(:,1);
%frequency
fs=200/4095;
f=zeros(4096,1);
counter=0;
for i=2:4096
  f(i)=f(i-1)+fs;
end
for j=1:8:240
counter=counter+1;
%Extracting fluctuating lift acceleration from data
liftt(:,counter)=records(:,j-1+3);%lift top
liftb(:,counter)=records(:,j-1+6);%lift bot
%Extracting fluctuating drag acceleration from data
dragt(:,counter)=records(:,j-1+2);%drag top
dragb(:,counter)=records(:,j-1+5);%drag bot
%Extracting velocity fluctuation from data
vel(:,counter)=records(:,j-1+8);%vel
velavg(:,counter)=sum(vel(:,counter))/4096;
vel(:,counter)=vel(:,counter)-velavg(:,counter);
end
%%
%for each sensor: fft of each data record using a windowing function,
%then average 30 ffts and find amplitude spectrum of averaged fft
%FFT
%windowing
w=tukeywin(4096,0.05);%Tukey window
for k=1:30
%%lift top
```

```matlab
lifttw(:,k)=liftt(:,k).*w;%Tukey window applied
lifttfft(:,k)=fft(lifttw(:,k));%fft
abslifttfft(:,k)=sqrt(lifttfft(:,k).*
conj(lifttfft(:,k)))/4096;%(amplitude)
%%drag top
dragtw(:,k)=dragt(:,k).*w;%Tukey window applied
dragtfft(:,k)=fft(dragtw(:,k));%fft
absdragtfft(:,k)=sqrt(dragtfft(:,k).*
conj(dragtfft(:,k)))/4096;%(amplitude)
%%lift bot
liftbw(:,k)=liftb(:,k).*w;%Tukey window applied
liftbfft(:,k)=fft(liftbw(:,k));%fft
absliftbfft(:,k)=sqrt(liftbfft(:,k).*
conj(liftbfft(:,k)))/4096;%(amplitude)
%%drag bot
dragbw(:,k)=dragb(:,k).*w;%Tukey window applied
dragbfft(:,k)=fft(dragbw(:,k));%fft
absdragbfft(:,k)=sqrt(dragbfft(:,k).*
conj(dragbfft(:,k)))/4096;%(amplitude)
%%velocity
velw(:,k)=vel(:,k).*w;%Tukey window applied
velfft(:,k)=fft(velw(:,k));%fft
absvelfft(:,k)=sqrt(velfft(:,k).* conj(velfft(:,k)))/4096;%(amplitude)
end
%%
%average all 30 data records
toplift=mean(abslifttfft,2);
[rowtl, colu] = find(ismember(toplift, max(toplift(:))));
topdrag=mean(absdragtfft,2);
[rowtd, colu] = find(ismember(topdrag, max(topdrag(:))));
botlift=mean(absliftbfft,2);
[rowbl, colu] = find(ismember(botlift, max(botlift(:))));
botdrag=mean(absdragbfft,2);
[rowbd, colu] = find(ismember(botdrag, max(botdrag(:))));
velocity=mean(absvelfft,2);
[rowv, colu] = find(ismember(velocity, max(velocity(:))));
%peak frequency of lift fluctuations (f0)
flposition=rowbl(1);
fl=f(flposition);
%%
%find main frequency of vibration in the lift direction (Fl)
%from the averaged lift spectra top and bottom, check spectral phase
top and bottom
%Cross-spectrum
for m=1:30
[PhaseLDb(:,m),F] = cpsd(liftb(:,m),dragb(:,m),w,200,200,200);
[PhaseLDt(:,m),F] = cpsd(liftt(:,m),dragt(:,m),w,200,200,200);
[PhaseLVb(:,m),F] = cpsd(liftb(:,m),vel(:,m),w,200,200,200);
[PhaseLVt(:,m),F] = cpsd(liftt(:,m),vel(:,m),w,200,200,200);
[PhaseDVb(:,m),F] = cpsd(dragb(:,m),vel(:,m),w,200,200,200);
[PhaseDVt(:,m),F] = cpsd(dragt(:,m),vel(:,m),w,200,200,200);
end
%averaged cross-spectrum
PLDb=mean(PhaseLDb,2);
```

```matlab
PLDt=mean(PhaseLDt,2);
PLVb=mean(PhaseLVb,2);
PLVt=mean(PhaseLVt,2);
PDVb=mean(PhaseDVb,2);
PDVt=mean(PhaseDVt,2);
%%
%Plot cross-spectrum phase Lift and Drag top
figure
subplot(2,1,2)
plot(F(1:51),-angle(PLDt(1:51))/pi,'k','linewidth',1.5);
xlabel('Frequency (Hz)','fontsize',12)
ylabel('Phase Lag (\times\pi rad)','fontsize',12)
set(gca,'linewidth',2,'FontSize',12)
set(gcf,'color','white')
box off
subplot(2,1,1)
semilogy(F(1:51),abs(PLDt(1:51)),'k','linewidth',1.5);
xlabel('Frequency (Hz)','fontsize',12)
ylabel('Amplitude (m/s^2)','fontsize',12)
set(gca,'linewidth',2,'FontSize',12)
set(gcf,'color','white')
box off
axis([0 50 0.00001 0.1])
yticks([.00001 .001 0.1])
%Plot cross-spectrum phase Lift and Velocity Top
figure
subplot(2,1,2)
plot(F(1:51),-angle(PLVt(1:51))/pi,'k','linewidth',1.5);
xlabel('Frequency (Hz)','fontsize',12)
ylabel('Phase Lag (\times\pi rad)','fontsize',12)
set(gca,'linewidth',2,'FontSize',12)
set(gcf,'color','white')
box off
subplot(2,1,1)
semilogy(F(1:51),abs(PLVt(1:51)),'k','linewidth',1.5);
xlabel('Frequency (Hz)','fontsize',12)
ylabel('Amplitude (\surd((m/s^2)\times v)','fontsize',12)
set(gca,'linewidth',2,'FontSize',12)
set(gcf,'color','white')
box off
axis([0 50 0.00001 0.001])
yticks([0.00001 .0001 0.001])
%Power Spectrum amplitude
figure
subplot(2,1,1)
semilogy(f(1:1024),toplift(1:1024),'k','linewidth',1.5);
xlabel('Frequency (Hz)','fontsize',12)
ylabel('Amplitude (m/s^2)','fontsize',12)
set(gca,'linewidth',2,'FontSize',12)
box off
set(gcf,'color','white')
axis([0 50 0.001 1])
yticks([0.001 0.01 .1 1])
subplot(2,1,2)
```

```matlab
semilogy(f(1:1024),botlift(1:1024),'k','linewidth',1.5);
xlabel('Frequency (Hz)','fontsize',12)
ylabel('Amplitude (m/s^2)','fontsize',12)
set(gca,'linewidth',2,'FontSize',12)
box off
set(gcf,'color','white')
axis([0 50 0.001 1])
yticks([0.001 0.01 .1 1])
%
figure
subplot(2,1,1)
semilogy(f(1:1024),topdrag(1:1024),'k','linewidth',1.5);
xlabel('Frequency (Hz)','fontsize',12)
ylabel('Amplitude (m/s^2)','fontsize',12)
set(gca,'linewidth',2,'FontSize',12)
set(gcf,'color','white')
box off
axis([0 50 0.001 0.1])
yticks([0.001 0.01 .1])
subplot(2,1,2)
semilogy(f(1:1024),botdrag(1:1024),'k','linewidth',1.5);
xlabel('Frequency (Hz)','fontsize',12,'color','k')
ylabel('Amplitude (m/s^2)','fontsize',12,'color','k')
set(gca,'linewidth',2,'FontSize',12)
set(gcf,'color','white')
box off
axis([0 50 0.001 0.1])
yticks([0.001 0.01 .1])
%
figure
semilogy(f(1:1024),velocity(1:1024),'k','linewidth',1.5);
xlabel('Frequency (Hz)','fontsize',12)
ylabel('Amplitude (Volt^2)','fontsize',12)
set(gca,'linewidth',2,'FontSize',12)
set(gcf,'color','white')
box off
axis([0 50 0.001 0.01])
figure
subplot(2,1,2)
plot(F(1:51),-angle(PDVt(1:51))/pi,'k','linewidth',1.5);
xlabel('Frequency (Hz)','fontsize',12)
ylabel('Phase Lag (\times\pi rad)','fontsize',12)
set(gca,'linewidth',2,'FontSize',12)
set(gcf,'color','white')
box off
subplot(2,1,1)
semilogy(F(1:51),abs(PDVt(1:51)),'k','linewidth',1.5);
xlabel('Frequency (Hz)','fontsize',12)
ylabel('Amplitude (\surd((m/s^2)\timesv)','fontsize',12)
set(gca,'linewidth',2,'FontSize',12)
set(gcf,'color','white')
box off
axis([0 50 0.00001 0.001])
yticks([0.00001 0.0001 0.001])
```